ET4300
Master Thesis EE

Sensitivity Assessment of the Dynamic Performance of MTDC-Linked Offshore-Onshore Systems

O. van Hooff, 4786173

Sensitivity Assessment of the Dynamic Performance of MTDC-Linked Offshore-Onshore Systems

by

O. van Hooff

to obtain the degree of Master of Science in Electrical Power Engineering
at the Delft University of Technology,
to be defended on september 21, 2023 at 10:00 AM.

Student number:	4786173	
Project duration:	November 14, 2022 – September 21, 2023	
Thesis committee:	Dr. Ir. J.L. Rueda Torres	TU Delft - IEPG, Supervisor & Chair of the Jury
	Dr. A.I. Stefanov	TU Delft - IEPG
	Dr. Ir. A. Shekhar	TU Delft - DCE&S
	Dr. M. Sharma	TU Delft - IEPG, Supervisor
	MSc. J. Bos	TenneT - ESP, Company supervisor

TU Delft

Abstract

The electrical power system is a critical infrastructure that provides a reliable energy supply for daily businesses. Designing resilient and reliable power grids is of paramount importance to prevent blackouts and their adverse economic impact on society.

Resiliency is fundamentally defined as the ability of a system to respond to high-impact disturbances with a low-probability of occurrence. Evaluating resiliency in power systems is usually done in three stages. The first phase is the disturbance progress. During the first phase, the resilience level deviates from its pre-disturbance level. This can be observed by analyzing different metrics in the network. Secondly, in the case of effective primary control actions, a new steady state operating condition is reached, which differs from the pre-disturbance operating condition. Finally, the system reaches the restorative stage. The recovery starts and the system returns to normal operation.

The assessment of resiliency is a combination of assessing all three previously mentioned stages (during-disturbance, post-disturbance, and restorative). Depending on the focus of the study, different technical aspects of a system are assessed. This thesis focuses on the assessment of the during-disturbance phase because, in future grids with lesser reserves available and limited control capabilities, the initial response of the system following a disturbance becomes more critical.

This thesis presents a basic qualitative study of the dynamic performance due to an active power imbalance during a disturbance on the AC and DC sides of hybrid power systems with an emphasis on an MTDC interconnected offshore-onshore system. The widely used RoCoF (Rate of Change of Frequency) is adopted as a performance metric to assess the active power-frequency response from the perspective of the AC side. In addition, a modified quantification of the Rate of Change of Voltage (RoCoV), which is usually applied in the design of protection schemes, is suggested as an attempt to better capture the response of the DC voltage.

The suitability of these metrics to properly reflect the resulting dynamics is analyzed by considering different disturbances, such as generator outages, line outages, converter outages, and faults like line-to-line and line-to-ground short-circuits, at either the AC or the DC sides. The different disturbances are executed using real-time digital simulations on the EMT model of the CIGRE BM1 DC-AC test system in RSCAD® FX. The performance metrics are well able to capture the impact of different disturbances on the response of the system. However, the performance metrics are not able to capture oscillating responses.

A study on the parametric sensitivity of the control parameters in the outer control loop of the converters is executed to see the influence of these parameters on the dynamic response and whether the performance metrics are able to capture the influence. The parameters of the outer control loop determine the reference currents for the converter, and thus directly influence the output of the converters. The results show that, for a DC line-to-line short-circuit, the adjustment of the control parameters in the outer control loop has no influence on the response of the DC voltage. For each control setting, the DC voltage still immediately drops to 0. This is also reflected in the performance metrics.

Whereas, adjusting the control parameters in the outer control loop influences the DC voltage response when subjected to an AC 3-lines-to-ground short-circuit. The proportional gains of the controllers mainly influence the overshoot of the DC voltage and have a small influence on the settling time. This corresponds to the role of the proportional gain in PI control, to respond quickly to faults. On the other hand, the integral gain responds slower and integrates the error over time to eliminate the residual error. Therefore, the results show that the integral gain mainly has an impact on the settling time of the response, and almost none on the overshoot. This is not captured by the calculated performance metrics. The performance metrics capture the response after the initial overshoot and this results in an unfair comparison between performance metrics.

Preface

Here it is, the long-awaited finalization of my study period in Delft. After 5 years, I will obtain my master's degree in Electrical Power Engineering. The past 5 years have been a much-enjoyed journey. During my secondary school period, I would never dare to imagine obtaining my master's degree within 5 years. During the past 5 years, I have obtained 315 ECs, made 64 exams (including only 3 resists), and spent countless hours in the lecture rooms of EEMCS. All of this has led to this final document. I hope you will enjoy reading it.

The field of Electrical Power Engineering is an ever-evolving area of study that has a significant impact on our daily lives. As the world population grows, the demand for efficient and sustainable power generation, transmission, and distribution is more crucial than ever. I hope that my thesis has made a small contribution to the development of a sustainable-ready power grid.

During the past 10 months, while working on my thesis, I must have drunk many liters of tea, re-listened to my favorite artists on YouTube a million times, and cycled the hilly road to TenneT in Arnhem too many times. But it was all worth it! Every day in either the master's office in Delft or the Arnhem office of Tennet or working from my parents' house, gave me the motivation to keep going! It was a pleasure to work with all the other master students in our own space on the third floor. Besides our work, we could share all of our gossip and problems with each other.

Completing a thesis requires dedication, hard work, and the support of many people. I would like to take this opportunity to express my gratitude to those who have made this thesis possible.

Firstly, I would like to thank my parents for facilitating my study. For always being extremely supportive throughout my years in Delft. Thank you both so much for all, I can not say enough how much it is appreciated. My dad was always there to read my chapters and talk about my ideas. And my mom was always interested in what I was doing and was always proud.

Secondly, I want to thank my supervisors for their constant support during the development of the thesis. Thank you, José for your support, patience, and expert advice during each stage of the research. And Monika, for being available for any questions I had. But also my guidance team within TenneT, Jorrit, Robert, and Wilhelm, were always there to chat about the progress and give me advice. Thank you so much for making time to support me! I would also like to thank the rest of the Grid Analyses NL team! You were always so interested in what I was doing and made me feel part of the team. I am going to miss working with all of you! I also would like to thank Remko for his RSCAD support, and fun chats!

Finally, I would like to thank my friends at the TU Delft office for supporting each other throughout the thesis. Naturally, I would like to thank Randi for her support. You always tried to understand what I was doing and explain it to your friends. You supported me throughout the process and stopped me from worrying about anything.

Thank you all for your support and encouragement. This thesis would not have been possible without you. And now, after a hopefully successful defense, it is time for a new chapter in my life: a real-life job at TenneT!

O. van Hooff
Noord-Scharwoude, September 13, 2023

Contents

List of Figures

List of Tables

1

Introduction

This chapter provides an overview of the background, scope, overall approach, and contributions of this thesis. In addition, the existing research gaps are identified in the related literature study.

1.1. Background

The electrical power system is undoubtedly the largest energy system in our society. The electrical power system is considered one of the most complex and critical infrastructure systems. It forms the backbone of modern societies by providing essential services of reliable energy supply, which facilitates trade, productivity, and economic growth. Large disruptions or breakdowns of the energy supply may cause serious economic damage [1].

Traditionally, the performance of the power system has been analyzed by classical risk assessment methods. This approach allows the system to respond adequately to known hazards and threats [1]. This type of study focuses on the reliability of power systems. Reliability refers to the probability of satisfactory provision of power and energy to meet load demands and the ability to withstand disturbances [2]. Traditional reliability studies measure the ability of a system to supply all loads. However, the origin of events is not taken into account. In addition, so-called high-impact low-probability (HILP) events are not taken into account [3]. HILP events are events that have a high impact on the systems but have a low risk of occurring. These types of events can be caused by external factors such as natural disasters or cyber-attacks [4].

In order to capture the impact of HILP events on the power system, the concept of 'resiliency' can be used. The word resiliency comes from the Latin word 'resire' and means 'bounce back' [5]. Resiliency has been adapted by different disciplines. The meaning of resilience differs among these disciplines [6]. In power systems, resilience is a relatively new concept. The increase in the probability of natural disasters due to climate change and increased vulnerability to cyber-attacks due to digitization has increased the need to research the resiliency of power systems [7]. The resiliency of the power system can be defined as: "The ability of the power system to return to its original state from external shocks that feature great influence and low probability of occurrence" [8].

Evaluating resiliency in power systems is usually done in three stages. The first phase is the disturbance progress. During the first phase, the resilience level deviates from its pre-disturbance level. This can be observed by analyzing different metrics in the network. Secondly, in the case of effective primary control actions, a new steady state operating condition is reached, which differs from the pre-disturbance operating condition. Finally, the system reaches the restorative stage. The recovery starts and the system returns to normal operation. The assessment of resiliency is a combination of assessing all three previously mentioned stages (during-disturbance, post-disturbance, and restorative). Depending on the focus of the study, different technical aspects of a system are assessed.

Designing resilient power systems is of paramount importance to mitigate the societal impact of partial or total disruptions. The proliferation of power electronic converter interfaced devices challenges the overall dynamic performance due to their limited control and protection capabilities [4]. The focus of this thesis is on the dynamic performance of hybrid AC/DC power systems during the disturbance phase because, in future systems with fewer reserves available and limited control capabilities, the initial response following a disturbance can become more critical, for example resulting in a critical dynamic deviation of the operational limits **[8].**

In the future, our energy supply will largely depend on the availability of renewable energy sources. The connection of renewable energy sources in remote locations is currently chosen to be developed by using High-Voltage Direct Current (HVDC) links that minimize power losses over long distances [9]. In the future, HVDC links may evolve into Multi-Terminal DC (MTDC) systems, enabling the meshed interconnection of multiple power sources and power systems through the use of DC links [10]. This means that the energy supply will be largely dependent on the availability of the MTDC system. Therefore, understanding the physical mechanisms of the dynamic response of MTDC-interfaced power systems for different disturbances is essential to devise appropriate operational and control measures in the design of MTDC systems.

1.2. Literature Review

This section provides a short summary of the review of relevant recent literature.

1.2.1. Multi-terminal HVDC Systems Modelling

The ongoing energy transition will lead to MTDC systems becoming more common in future electricity systems [11]. The Modular Multilevel Converter (MMC) is a promising voltage-source converter technology for MTDC systems because of advantages in high power-handling capability, low switching frequencies, and reduced harmonic distortion [12]. There are hundreds of submodules in each MMC acting as its building blocks.

Electromagnetic Transient (EMT) simulation is a fundamental way of studying the operating characteristics of MMC-based MTDC systems. EMT simulations are able to capture detailed dynamics of both MMCs and MTDC systems [13]. The computational burden of EMT simulations rises with the increasing number of submodules. In order to improve the simulation efficiency, different kinds of simplified EMT models have been proposed for MMCs, such as Thevenin equivalent model [14] and average-value model [15].

To study the interaction between AC and DC power systems, not only the dynamics of the MTDC system but also of the dynamics of the AC system are of interest. Even with the implementation of a simplified MMC model, the computation burden of a large hybrid AC/DC power system can entail bottlenecks**.** [16]. To achieve a higher simulation efficiency, different EMT simulation methods have been proposed for hybrid AC/DC power systems. The analysis in [17] neglects the inductances of DC lines, such that both AC and DC power systems can be simultaneously simulated with the same time-step. Alternatively, [18] proposes a MTDC system modelling approach by considering the modulation indices of converters and the resistances of DC lines. However, in this approach, a simplified model was used where the inductance and capacitance of the DC lines were neglected, which has a significant impact on the dynamic response of the MTDC system.

The aforementioned studies were all carried out on monopolar MTDC systems. A simulation method for bipolar MTDC systems is proposed in [16], which describes a method where the inclusion of bipolar MMC-MTDC is established by using the companion circuit method. In addition, the inductances of DC lines are exhaustively modelled to ensure the simulation accuracy when a DC fault occurs. In order to overcome the difference in time constants between AC and DC systems, a multi-rate scheme is adopted to ensure simulation efficiency [16]. This method has been shown to be able to deal with large power systems with the inclusion of bipolar MTDC systems. The addition of modelling the inductances of DC lines has improved the simulation accuracy of DC faults. However, due to the simplification of the MMC, the proposed method is not suitable for studying the internal behaviour of a converter station. Another limitation is the system can not be used for harmonic studies on the AC sides [16].

In this thesis, an EMT model of MMC units is taken from the RSCAD library. This MMC model will be used to establish the dynamics of an MTDC-interconnected offshore-onshore system. In addition, the model will be used for studying the parametric sensitivity of the control parameters of the outer loop during a disturbance.

1.2.2. Evaluation of Disturbances

The power system is one of the critical infrastructures. Any failure or destruction affects the safety, security, economy, health, and well-being of a community. A fault in a power system can occur due to various reasons, such as an insulation failure, system overloading, or lightning strikes [19]. But also faults caused by external factors can occur in the power system. For example, faults caused by natural disasters or cyber-attacks [20].

In case of a fault in an MTDC system, two critical situations can occur — either a sharp drop in voltage or a rapid increase in voltage [21]. As HVDC systems have a low impedance due to the absence of a fundamental frequency minimizing its series inductance, the DC fault current has a large peak and steady values within a few milliseconds [10]. The worst case DC fault for a VSC[1]-based HVDC systems is a line-to-line short-circuit. This type of fault is usually caused by an insulation failure between the two DC conductors. When a line-to-line fault occurs, the stored energy in the system capacitances will be discharged rapidly. Simultaneously, the AC system will experience a three-phase short circuit through the fault point [22].

This thesis will evaluate the impact of different disturbances on hybrid AC/DC systems. Disturbances that will be examined are generator outages, converter outages, line outages, and short-circuit disturbances. The impact of disturbances can be evaluated in different ways.

In [23], the impact of a disturbance is evaluated by quantifying the ability to supply critical loads. Moreover, in [24], this impact is assessed based on the amount of generation capacity that is lost. However, neither of those studies addresses the stage during the disturbance itself from a dynamic viewpoint. This type of analysis is done in [11]. The impact of AC faults, DC faults, and converter outages on a system with different types of converters is analyzed by comparing the responses of the DC voltage and active and reactive power in each line. The results of this research indicate that the DC system has the weakest response after DC faults. This conclusion is based on the fact that the response shows no recovery in comparison to AC faults and converter outages. However, no quantification is given to the initial response of the system during the disturbance.

In this thesis, the impact of disturbances on the dynamic response of the system is evaluated by quantifying the dynamic response of the system. For each side (AC & DC) of the system a performance metric is adopted to qualitatively analyze different possible forms of the resulting dynamic performance of the system during a disturbance.

1.2.3. Control functionalities of MTDC

The control system of a MMC has two main functions, the control of DC voltage and AC side auxiliary control. Regulating the DC voltage is the main control challenge in MMC-based MTDC systems since it is used to stabilize the operations of the DC system. However, the DC voltage is directly associated with the balance of active power, similar to frequency parameters in AC system systems. But, unlike frequency which is often considered a universal parameter, the DC voltage varies throughout the system depending upon the power injection at each node [25].

In [26], the ENTSO-E recognizes that the use of advanced functionalities of HVDC control functions is essential for a secure and efficient operation of hybrid AC/DC power systems. To overcome the frequency-related issues caused by reduced primary control capabilities in power systems, in literature several alternative control structures are proposed, such as Virtual Inertia (VI) and Fast Frequency Regulation (FFR).

In this thesis, the parametric sensitivity of the control parameters in the outer loop of an average MMC control loop is analyzed for the worst-case AC side and DC side disturbance. The goal of these analyses is to analyze the influence of the control parameters on the adopted performance metrics.

1.3. Objectives and Research Questions

The overall goal of this thesis is to evaluate the impact of disturbances on the active power flow across an MTDC-linked offshore-onshore system. To this aim, two performance metrics are adopted. The first metric quantifies the dynamic response on the AC side while the second metric quantifies the dynamic response on the DC side.

The effectiveness of the adopted metrics is evaluated by performing single-value parametric sensitivity analysis and by considering different disturbances like generator outages, line outages, converter outages, and faults such as line-to-line and line-to-ground faults. This analysis is intended to investigate the extent of understanding of the influence of primary control parameters in the outer loop and the determination of

---

[1] VSC: Voltage source converter

the control system's effectiveness in responding to diverse events. The following research questions are addressed:

1. What insights on the impact of different disturbances on the dynamic response can be gained from the adopted performance metrics after a disturbance in an MTDC-linked offshore-onshore system?
2. How effective are the adopted performance metrics in capturing the sensitivity of the parameters in the outer control loop of an MMC converter on the dynamic response in an MTDC-linked offshore-onshore system?

1.4. Thesis Contributions and Approach

Based on the defined thesis objectives and research questions as outlined in the previous section, the main contribution of this thesis is the identification of the boundaries of the adopted performance metrics with and without the adjustment of the control parameters in the outer loop.

In order to achieve the overall objective, in this thesis the approach shown in Fig. 1.1 is used. This figure shows a high-level overview of the approach. Firstly, the performance metrics will have to be defined to describe the dynamic response on each side of the system. After defining these performance metrics, a calculation implementation is needed in a case-study environment to assess the effects and its limitations. The input of the Python model used for calculation will be in the form of CSV files containing the measured signals from the disturbance cases.

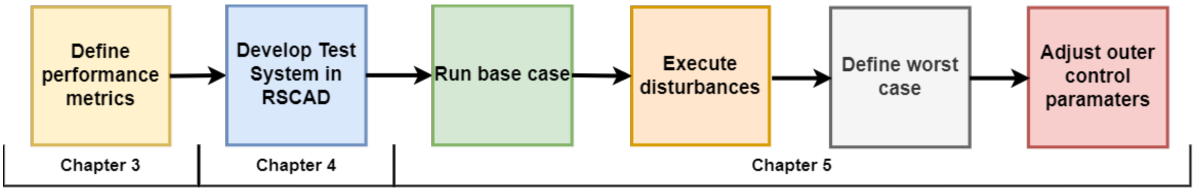

Figure 1.1: High-level overview of the approach used in this thesis

Secondly, the test system is developed in RSCAD. RSCAD is an EMT-based simulation program that enables real-time simulation. The test system will extended with different types of disturbances such as component outages and short-circuits. Within the RSCAD environment, a script will be written to enable the automatic operation of the test system.

Once the test system is developed, it will be run under normal operating conditions. This will serve as the base case for the analyses. After analyzing the performance of the test system under normal conditions, the system will be faced with different disturbances. Based on the calculated performance metrics, the worst-case AC side and DC side disturbance will be selected to use in the parametric sensitivity analyses. In the parametric analyses, the parameters of the outer control loop will be adjusted to see the influence on the adopted performance metrics.

1.5. Outline

The remainder of this thesis is organized as follows:

- Chapter 2 will go into the theoretical and modelling background of this thesis. In this chapter, the theory and modelling aspects of MMC units, transmission lines, and controllers will be discussed. In addition, an overview of the implemented EMT model in RSCAD is presented.
- Chapter 3 will explain the performance metrics that are used in this thesis. For each metric, the motivation, the theory, and the implementation will be discussed.
- Chapter 4 will describe the details of the implemented model and the implementation of the parametric sensitivity in RSCAD.
- Chapter 5 will go into the analysis of the different disturbances and the parametric sensitivity analysis of the outer control parameters.
- Chapter 6 will conclude this thesis by providing a summary of the main findings, as well as the answers to the research questions. Finally, suggestions for future research are also given in this chapter.

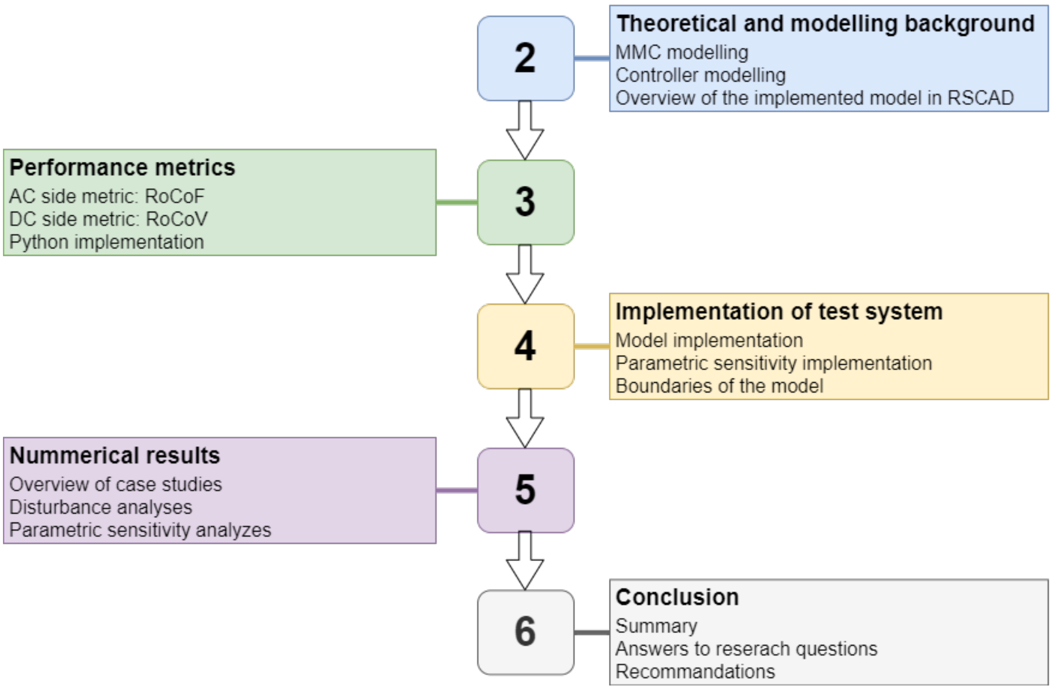

Figure 1.2: Outline of thesis document

2

Theoretical and Modelling Background

HVDC systems enable power transmission over long distances with reduced power losses compared to HVAC. Above that, HVDC allows the coupling of asynchronous AC systems [21]. At this point, the majority of HVDC connections are point-to-point. However, in point-to-point connections, the power flow is interrupted in case of a fault on the DC line. In order to overcome the full loss of power, multi-terminal HVDC systems are developed [10].

In this chapter, the theoretical background and modelling required for this thesis will be discussed. Each section will shortly go into the theory of that part and how to model this part. Firstly, the physical components of an MTDC system will be discussed in section 2.1. Secondly, section 2.2 will discuss the control system of an MTDC system.

2.1. MTDC System Components

A typical MTDC configuration consists of MMCs, commuting transformers, AC side and DC side capacitors, and DC transmission lines or cables [22]. The MMCs connect the AC systems to the MTDC system and convert the AC power to DC and vice versa. A commutation transformer separates the MMC output voltage from the AC system voltage. A DC side capacitor is used to reduce the voltage ripple on the DC side. Whereas, the AC filter reduces the harmonic currents produced by the converter [27].

In this section, the theoretical and modelling background of MMC converters will be discussed. Followed by the theoretical and modelling background of MTDC transmission lines and cables. The theory will support the models used in the test system as will be explained in chapter 4.

2.1.1. MMC Converters

In order to transmit power via an HVDC system, converters are needed to convert electrical power from AC to DC and vice versa. At the sending end, rectifiers are used to convert incoming AC power to DC. Inverters are used at the receiving end to convert the DC power back to AC. The 2 major types of power electronic converters are defined based on the main electrical variables: Current-Source Converter (CSC) and Voltage-Source Converter (VSC) [7]. Due to the fact that CSCs can not easily reverse the power flow, VSC is the preferred solution for MTDC systems. The main advantage of using VSCs is the ability to maintain a constant voltage when the power flow is reversed [28].

VSCs are classified depending on the number of voltage levels they can generate, this can be either two-level or multi-level. A two-level VSC can generate voltages of $-1/2\,V_{DC}$ and $1/2\,V_{DC}$. Newer multilevel voltage-source converters offer additional advantages compared to the traditional 2-level voltage-source converters. Multilevel voltage-source converters produce lower harmonics and suffer from fewer switching transients [29]. Besides that, multilevel converters create a lower dv/dt compared to 2-level converters. [30] This makes the modular multi-level converter the most prominent technology for high-power transmission as compared to 2-level VSC and other converter topologies [31].

Converter Models

Various computational models are available for simulating MMC converters. In [32], seven types of computational models are classified. The type of model suited for a study depends on the time frame of the analyzed phenomena on the DC system. The different types of computational models from [32] are summarized in table 2.1. The models of types 2 through 6 should in principle use the control system structure as the one used for type 1 based models. However, some of the low-level control functions might become irrelevant in the more simplified models.

Type of model	Relative computing time	Type of simulation tools	Type of studies
Type 1	NA	Circuit simulation tools	Not suitable for system studies
Type 2	1000	EMT	Detailed studies of faults in submodeles Used to validate simplified models
Type 3	900	EMT	Detailed studies of faults in submodules Used to validate simplified models
Type 4	30	EMT	Detailed studies of AC and DC fault close to converter
Type 5	2	EMT	Studies of AC and DC transients High level control system design-harmonic studies
Type 6	1.5 0.1	EMT Phasor domain	Studies of remote AC and DC transients
Type 7	0.01	Load-flow tools	Power flow

Table 2.1: Summary of converter model types [32]

For analyzing the impact of different disturbances, type 4 models are the most suited solution. The breakthrough of this model is that it realizes a drastic reduction in the number of electrical nodes for the simulation. The reduction is realized by making use of Thevenin equivalents. In addition, this model still reveals accurate impacts of different capacitor voltages in each sub-module. This makes it still possible to use this model in real-time simulations of MMC-based models of HVDC systems [33].

For EMT-type programs, the most commonly used method to solve differential equations is trapezoidal integration. By using this method, the solution of the voltage equation of a capacitor can be represented by a voltage source in series with an impedance. The resulting equation is [32]:

$$U_c(t) = R_c * I_c(t) + U_{c\_eq}(t - \Delta T) \tag{2.1}$$

Where $R_c = \Delta T/2C$, and $U_{c\_eq} = (\Delta T/2C) * I_c(t - \Delta T) + U_c(t - \Delta T)$. As a consequence of this, a submodule can be represented by the equivalent circuit shown in Fig. 2.1. Where the values of R1 and R2 depend on the gate signals and the direction of the current. In addition, the model takes into account the voltage across each diode in order to choose the values of R1 and R2 [32]. Finally, from the equivalent circuit in Fig. 2.1,

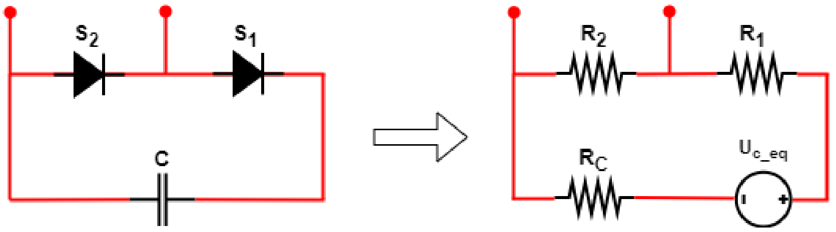

Figure 2.1: Equivalent model of submodule (Inspired by [32])

the Thevenin equivalent circuit can be built as shown in Fig. 2.2. The voltage across the submodule can be calculated from the equation:

$$U_{sm}(t) = R_{sm\_eq}(t) * I_{MV}(t) + U_{sm\_eq}(t - \Delta T) \tag{2.2}$$

With the equivalent resistor being equal to:

$$R_{sm\_eq} = \frac{R_2(t)(R_1(t) + R_c)}{R_2(t) + R_1(t) + R_c} \tag{2.3}$$

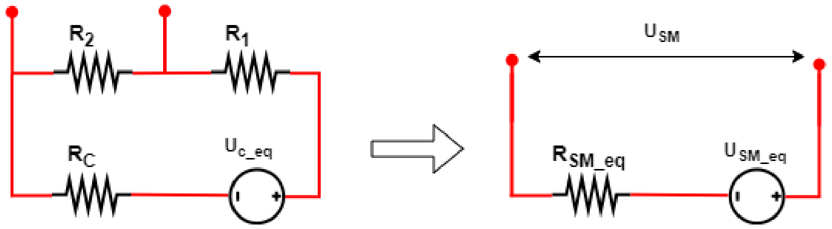

Figure 2.2: Thevenin equivalent model of submodule (Inspired by [32])

For the final model, all submodules are connected in series to create a multivalve. This can be replaced by an equivalent Thevenin circuit, with the equation:

$$U_{sm}(t) = (\sum R_{sm\_eq\_i}(t)) * I_{MV}(t) + \sum U_{sm\_eq\_i(t-\Delta T)} \tag{2.4}$$

2.1.2. MTDC Transmission Lines and Cables

There are 2 main topologies for HVDC transmission systems: monopolar and bipolar [22]. The choice for topology depends on the operational requirements, reliability, flexibility of demand and cost of the HVDC system [34]. The monopolar configuration has only one pole, which is mostly the negative polarity to reduce corona effects [35]. The return path is either the ground, sea, or metal [22]. The main disadvantage of all monopolar topologies is the lack of redundancy. If a fault exists in the link, the full capacity of the link is lost. In addition, in case of a DC fault, all terminals are affected by the high fault currents [22].

In bipolar topologies, power transmission is carried out using 2 conductors of opposite polarity. It is built up as a combination of 2 monopolar HVDC systems. This makes it a more costly alternative, compared to monopolar. However, bipolar can achieve twice the power rating of similar monopolar configurations. The main advantage of bipolar is redundancy. In the case that one of the poles is removed, the other pole will resume normal operation [22]. Even though grounding is not necessary, it is often provided for bipolar configurations. Without a return path, the entire HVDC transmission system will be made unavailable during faults [35].

Both overhead lines and cables are used for transmission via HVDC systems. However, as many HVDC projects involve offshore connections, most of the HVDC systems use DC cables. In addition, HVDC cables are also used for transmission on land for projects in city areas. HVDC overhead lines are mainly used for bulk transport over long distances, as the installation costs are lower compared to cables [32].

Frequency Dependent Modeling

When modelling cables or lines for EMT simulations, it is advised that frequency-dependent traveling wave models are used. Frequency-dependent travelling wave models take into account the frequency-dependent nature of the transformation matrix [36].

The electrical parameters of a line or cable are frequency-dependent due to the skin effect of conductors and the earth's return path. The modelling techniques of a frequency-dependent line or cable model are complicated, and not relevant to discuss in detail [32]. Instead, a short overview of the process will be given.

The first step is the computation of frequency-dependent parameters for a wide range of frequencies. Usually a range from 0 Hz to 1 MHz is used for this. Secondly, the frequency-dependent parameters are approximated by a continuous frequency-dependent function. In the final step, using a convolution technique, a time domain equivalent circuit is derived from the approximated functions. These time domain circuits can be implemented in EMT-type software packages [32].

There are two types of frequency-dependent models: phase domain models and modal domain models. Phase domain models refer to the mathematical treatment of defining frequency-dependent transmission line transfer functions without the use of a modal transformation. For a phase domain model, the transfer function equivalents are realized directly on a per conductor basis or phase domain basis.

Modal domain models consist of a set of equations that describe key features of phenomena based on the physical characteristics of transmission paths. For a three-phase overhead transmission line, there are only three modes and they are equivalent to the sequence component definitions. For underground or submarine cable systems, the modes are defined by the number of conducting elements including cores and sheaths or screens.

2.2. MTDC Control System Designs

The main function of the MTDC control is to control the power flow between the terminals. In addition, it has to maintain a stable output of active and reactive power. The control of an MTDC system is expected to tolerate severe transient AC waveform distortions and rapid changes in the magnitude and phase of AC voltages without leading to any problems [37].

A schematic representation of the hierarchy of an MTDC control system is shown in Fig. 2.3. The controllers of the converters receive their input from the master controller. The master controller is provided with the minimum set of functions necessary to coordinate the converters in the MTDC system. By controlling the DC voltage, the master controller regulates the overall performance of the MTDC system.

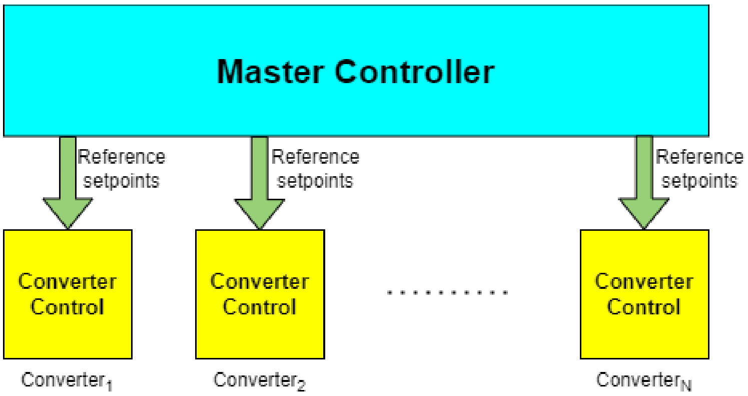

Figure 2.3: Schematic representation of MTDC system control hierarchy

2.2.1. Master Control

Any power unbalance reflects voltage variation in the MTDC system. In the case that there is more generation than demand, the DC voltage is increased as the capacitors are being charged with additional power. On the other hand, when there is more power drawn from the MTDC system compared to the amount of power injected in the system, the voltage will drop. In this case, the converters will ask for extra active power, which will be supplied by the capacitors [38].

The control of the DC voltage is more essential when compared to the AC system due to the small time constant of the capacitor [39]. This requires a fast reaction of the control system. The time constant for the primary control is in the order of tens of milliseconds [40]. The hierarchical control for MTDC systems can be divided into 3 control levels. Similar to AC system control, the higher-level control always acts slower than the lower control layer [41].

The voltage control can be achieved using different methods. The most commonly used methods are droop control, master-slave control, and voltage margin control [39]. For this thesis, the master-slave control strategy will be used. In this control scheme, one of the converters is configured for voltage control (master) and the remaining converters are configured for constant active power control (slaves). The power balance of the MTDC system is maintained by the voltage-controlled converter [42].

2.2.2. Converter Control

The control of the converter controls the converter by calculating PWM[1] pulses for the bridges of the converter. The controller consists of different levels: lower-level controls and upper-level controls. The combination of lower and upper-level controls forms the pole control. The master controller provides the reference inputs for the upper-level control of the converter [32].

The lowest level is specific to the topology of the valves inside the converter. The lower level control operates the fastest and is also known as firing control. The firing control takes the desired converter waveform as an input and determines by means of the valve firing logic the pulses that need to be generated [7]. The next level is the upper-level control, which addresses the dispatch of the overall converter. This is independent of the converter technology. The upper-level control controls the current through the phase reactor [42].

A general overview of the upper-level control can be seen in Fig. 2.4. After transforming the incoming signals into per-unit values, the three-phase quantities are transformed into the dq0-frame using the Clark transformation. By using the dq0-frame, the converter control can control the active and reactive power independently [43].

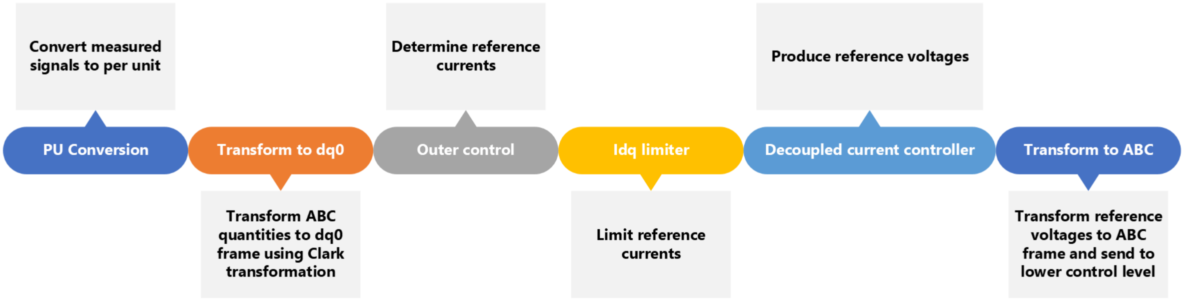

Figure 2.4: General overview of the upper-level control system for the converters

The calculated dq values are then sent to the outer control loop of the converter. The outer control loop is responsible for determining the reference currents. The general design of an outer control loop can be seen in Fig. 2.5. The active power loop (d-axis) can be configured to control either the DC voltage or active power, provided the AC system is sufficiently strong. The reactive power control loop (q-axis) can be selected to regulate either the AC voltage or the reactive power Q at the point of common coupling [44].

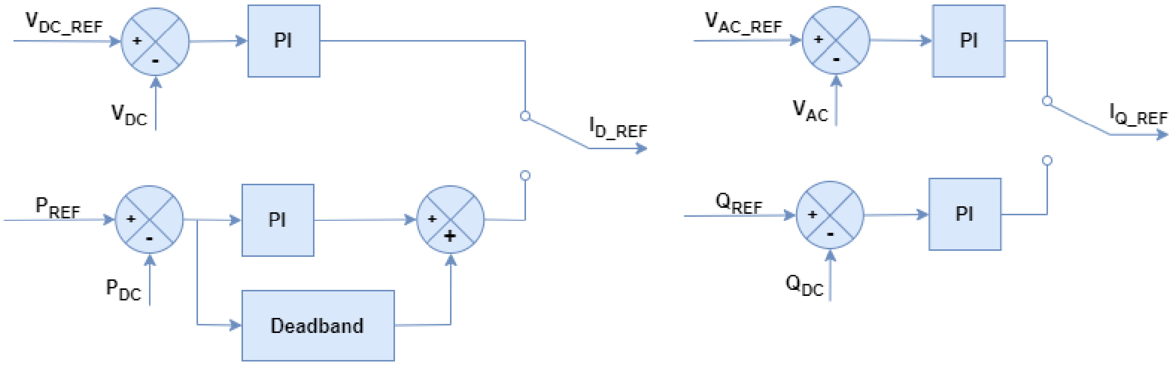

Figure 2.5: Outer level control system for the converters

The outer controller provides the current references i_{d_ref} and i_{q_ref} to a current limiter block. As a typical limiting scheme, the magnitude of the converter current is limited to I_{max}. In addition, this block offers the possibility to give priority to active or reactive power control. For example, in case of AC faults, priority can be given to restoring the system. This is done by maximizing the i_q reference and forcing i_d to 0 [32].

The outputs of the current limiter stage (i_d and i_q) are then given to the decoupled current regulator block. This stage produces the reference d and q voltages v_d and v_q which are transformed back into 3-phase com-

---

[1] PWM: Pulse Width Modulation

ponents and sent to the lower-level controls. Lower-level controls, including capacitor voltage balancing methods, are not discussed in this thesis. All details regarding lower-level controls can be found in the appendix of [32].

3

Performance Metrics

The assessment of the dynamic performance of hybrid AC/DC power systems for different disturbances is the process of evaluating the ability of an electrical system to maintain a stable state of operation. The assessment should provide a clear insight into the impact of a disturbance on the stability of the power system [6].

MTDC systems are becoming more popular for the connection of renewable energy sources in remote locations to the main system. However, MTDC systems are more complex and can be more vulnerable to disruptions and failures. At this point, there are no standardized metrics for assessing the dynamic response of hybrid AC/DC systems during a disturbance [10].

The metrics that will be used for the assessment should be able to capture the intensity of faults, the distance to the fault, and the strength of the system. In order to capture the response of a hybrid AC/DC system when subjected to a disturbance, 2 indicators will be used. Each metric should capture one important stability aspect of the system. The first indicator is used to determine the stability of the AC system. Another indicator will be defined for the assessment of the stability of the DC system.

The coming two sections will explain the chosen metric for each individual part of the system. Firstly, in section 3.1 the chosen AC indicator, rate of change of frequency (RoCoF), is described. Secondly, section 3.2 will explain the indicator of the DC side, which is the rate of change of voltage (RoCoV). Finally, the Python implementation of the metrics will be discussed in section 3.3.

3.1. AC indicator: RoCoF

Frequency is an important parameter in AC power systems, as it determines the synchronous operation of the system. When the frequency of the system is stable and within limits, connected generators will operate in synchronization with each other. However, if the frequency deviates too much from the nominal value, it can cause the generators to operate out of synchronization, which can result in power system instability, blackouts, or damaged equipment. Therefore, the frequency is a critical parameter that must be carefully controlled and maintained to ensure the safe and reliable operation of the power system [45].

Power system frequency stability refers to the ability of a power system to maintain a stable frequency following a disturbance. A typical response for the frequency following a disturbance can be seen in Fig. 3.1. The frequency response can be divided into four stages: inertia response, primary frequency control, secondary frequency control, and tertiary frequency control [46]. In the figure, it can be seen that during the first stage the frequency drops following a disturbance. During this phase, the inertial response determines the dynamics of the frequency by converting kinetic energy into electrical energy. The larger the inertia, the smaller the dip in frequency [47].

For this research, the first phase of the frequency response is of interest. The most commonly adapted parameter to describe the dynamic response is the rate of change of frequency (RoCoF) [48]. The RoCoF is defined as the derivative of the frequency, as shown in the equation below.

$$RoCoF = \frac{|f(t_0+T) - f(t_0)|}{T} \tag{3.1}$$

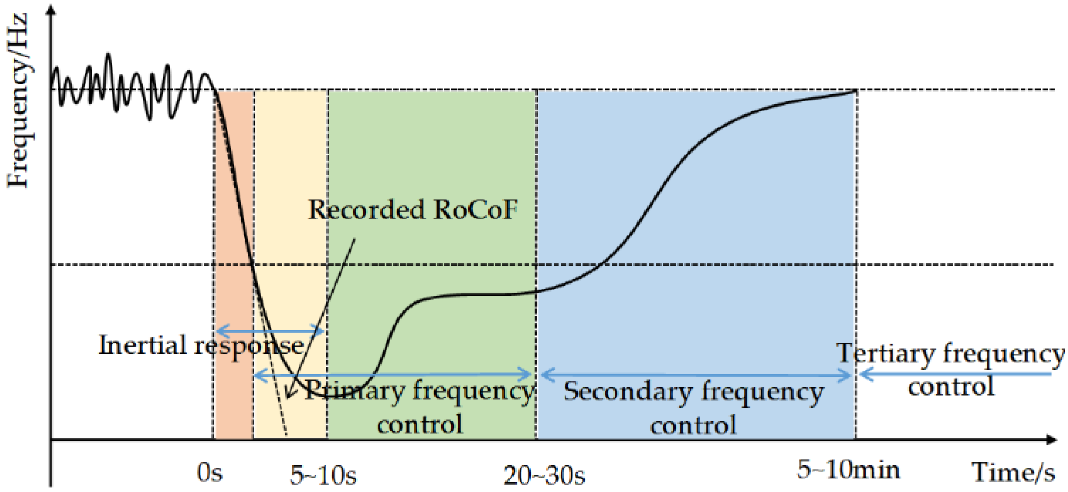

Figure 3.1: Typical frequency response of a power system following a disturbance [48]

The value of RoCoF is related to the initial response of the system. The relationship between the inertia and RoCoF can be described by the following equation [48]:

$$\frac{2H_{eq}}{f_0}\frac{df_I}{dt} = \Delta P_g(t) - \Delta P_L - D_{eq}\Delta f \tag{3.2}$$

where H_{eq} the equivalent inertia constant of the power system, f_0 is the normal frequency, $\frac{df_I}{dt}$ is the differential of the measured frequency, ΔP_g the change in output power from generators, ΔP_L the unbalanced active power caused by the contingency, D_{eq} the equivalent damping factor of the power system, and Δf is the frequency deviation from the normal frequency.

In the traditional power system, RoCoF was of less relevance, due to synchronous generators that limit and prevent high values of RoCoF. However, the increase in renewable energy sources and the disconnection of synchronous generators decrease the system inertia. As can be seen in Eq. 3.2, this will lead to higher values of RoCoF [49]. The appearance of high RoCoF values is usually interpreted as the need of action of protection devices, e.g. under-frequency load-shedding (UFLS) [49].

Grid Code	T	Security Threshold (Normal Frequency)
IEEE [50]	N.A.	0.4 Hz/s (60 Hz)
The Netherlands [51]	500 ms	2 Hz/s (50 Hz)
Germany [52]	500 ms	2 Hz/s (50 Hz)
Ireland [52]	200 ms	1 Hz/s (50 Hz)
UK [52]	500 ms	1 Hz/s (50 Hz)
Australia [49]	N.A.	No RoCoF standard (50 Hz)
USA [53]	N.A.	No RoCoF standard (60 Hz)
ENTSO-E [54] (for HVDC connected parties)	1 s	2.5 Hz/s (50 Hz)

Table 3.1: International grid codes on maximal values of RoCoF

Each individual system operator is left to define its own limits for RoCoF. Resulting in different values of RoCoF for different countries. Each country also uses its window period to calculate RoCoF [49]. In table 3.1, the RoCoF threshold values for several European and world power systems are shown. Not all countries have defined a security threshold for RoCoF yet. The security threshold for RoCoF has to be small enough to protect devices under extreme scenarios, while it must also be large enough to avoid triggering unexpected cascading failures [48].

System operators are facing the need to change the grid code specifications regarding RoCoF withstand capabilities, due to increasingly high penetration of power electronic devices [48]. In 2020, Ireland increased from 0.5 Hz/s to 1 Hz/s [49]. The UK has increased the RoCoF threshold from 0.125 Hz/s to 0.5 Hz/s for existing generators, and 1 Hz/s for new generators [49].

The ENTSO-E has written a guidance document for the national implementation of network codes on HVDC-system connections. Article 12 states that HVDC systems should be capable to withstand frequency changes at a rate between -2.5 and 2.5 Hz/s. The width of the measurement window is 1 second. For DC-connected power plants, connected via an HVDC converter, the system should be able to withstand frequency changes at a rate between -2 and 2 Hz/s [54].

3.2. DC indicator: RoCoV

In HVDC systems, the voltage magnitude is typically applied to control the power flow exchange between the converter stations. Voltage stability is defined by IEEE as the ability of a power system to keep the voltage within allowed limits [55]. Voltage instability occurs when the power system cannot keep the voltage between limits. The main causes of voltage instability are faults in power system components, such as generators, power transformers, and transmission lines.

Voltage stability indices can be used to describe the voltage stability of a power system. In literature, there are a lot of indices to define the power system voltage stability. The voltage stability indices can be categorized into 2 main groups: (i) system variable-based and (ii) Jacobian matrix-based [55]. In table 3.2, the differences are listed. For the purpose of assessing the dynamic response of the DC voltage, an index from the system variable-based category would be most suited. Jacobian matrix assessments require collecting the whole data of the power system components to define the voltage collapse point, which is not of interest to this research.

System variables-based	**Jacobian matrix-based**
Online purpose	Offline purpose
Used by operator	Used by designer
Based on bus and line elements	Based on Jacobian matrix modifications
Low computational requirements	High computational requirements
Compute the weakest area	Compute nearest voltages collapse point

Table 3.2: Differences between main categories of voltage stability indices

In [55] a list of 49 possible voltage stability indices is presented. The presented system variable-based indices are mainly conceived for the assessment of the steady-state performance of HVDC systems or solely based for usage in a three-phase system. Therefore, another way must be found to quantify the dynamics of the DC voltage excursion following a disturbance.

For detecting faults in MTDC systems, protection schemes in DC systems usually apply the rate of change of voltage (RoCoV) [56]. The use of RoCoV as an indicator in protection schemes motivates its usage as a performance indicator for the DC side. In MTDC systems it is not possible to rely on protection schemes that require communication from one end to another. It is necessary for each breaker to measure the fault transient and determine quickly whether the fault is on the segment of the line that it is protecting [57]. Although overcurrent would be a good indicator of a fault, waiting for the current to exceed a threshold before tripping adds a significant delay.

Another possibility is using the rate of change of current seen by the breaker as an indicator. Each breaker in the system has an inductor in series with it to limit the rate of rise of fault current. Therefore, the rate of change of current can be described by the following equation [57]:

$$\frac{di(t)}{dt} = \frac{v_{bus}(t) - v_{line}(t)}{L} \tag{3.3}$$

where L is the inductance of the limiting inductor and v_{bus} and v_{line} are the voltages on the bus and line side of the inductor.

As a result, the rate of change of current is approximately proportional to the voltage change on the line side, making the RoCoV at the line side a suitable indicator to detect and locate faults [57]. This feature of RoCoV, makes it also suited as a performance metric to quantify the dynamic response of the DC voltage after a disturbance.

During normal operation, the RoCoV values are around zero since the DC voltage is constant. However, during fault conditions, the DC voltage makes a sharp drop resulting in a quick increase in RoCoV [56]. Fig. 3.2 shows a typical voltage response after a disturbance. The recorded RoCoV is shown and is equal to the average slope over the chosen window period. The equation of RoCoV is formulated in a similar fashion like RoCoF:

$$RoCoV = \frac{|V_{DC}(t_0 + T) - V_{DC}(t_0)|}{T} \tag{3.4}$$

where, $V_{DC}(t)$ is the DC voltage magnitude and T is the time window of calculation. In protection schemes, the time window corresponds with the typical measurement sampling period (in the order of a few ms), to ensure a fast protective action. By contrast, a relatively longer time window is considered in this thesis, in line with the typical reaction time of primary DC voltage control. After conducting several EMT simulations, it turned out that T can be within 0.1-0.4 s, due to the steep DC voltage deviation caused by an abrupt power imbalance [57]. By using a longer window period, it is not possible to use the threshold values of RoCoV used in literature as a reference for what values of RoCoV are acceptable.

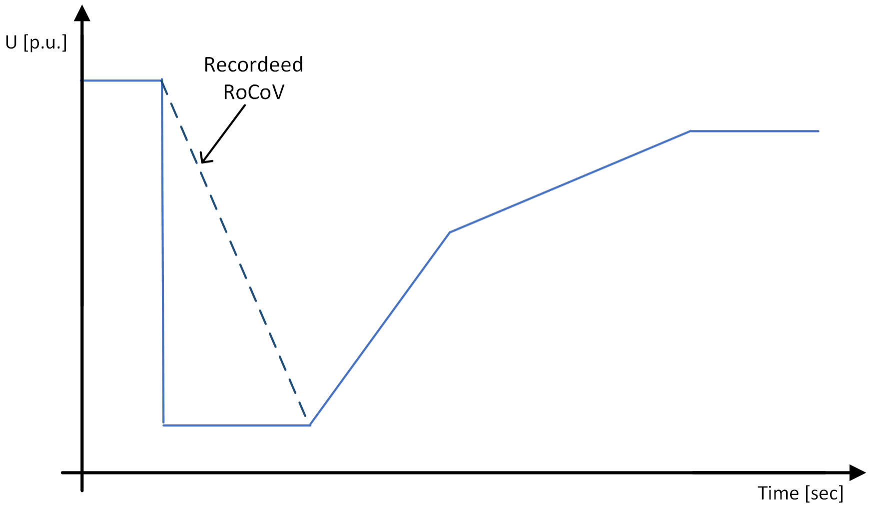

Figure 3.2: Fault-ride-through profile of an HVDC converter station (Inspired by [58])

3.3. Python Implementation

Now that the performance metrics are defined, their implementation must be developed. In Python, a general script is written to calculate the rate of change values. The measured data from the simulations is available in separate csv files for each scenario. The goal of the Python script is to generate a table including all calculated rate of change values for each simulation case. An overview of the methodology used in the Python script can be seen in Fig. 3.3.

The Python script consists of 2 functions. The first function calculates the rate of change value. The window length of this function is variable, such that different window lengths can be used. The second function generates the table with calculated values. For each scenario, the values of RoCoF and RoCoV are calculated at every converter in the system. This function obtains the data from the right csv file, and sends the data to the first function. Both functions can be found in App. A.

The rate of change function can be found in App. A.1. This function can be used to calculate the rate of change of any signal that is put in. As input, this function requires the array to calculate the rate of change with ($array$), the window length in seconds (t_w), the step size ($step$), and the start time of the first window in seconds (beg). The first step in this function is to define the location of the first and final samples of the window. The start location depends on the input of the start time of the first window. The first sample is calculated as a multiplication of the start time and the sampling frequency. The final sample of the window is

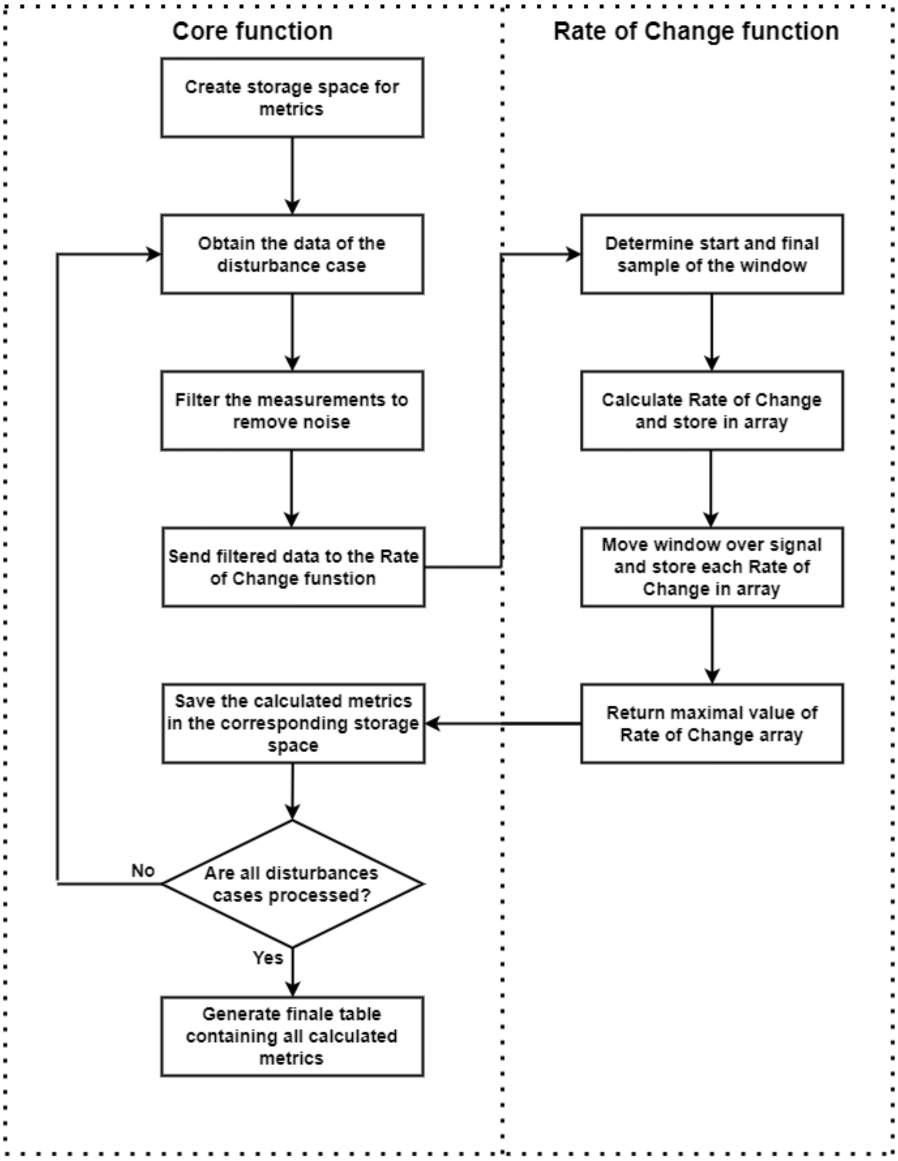

Figure 3.3: Overview of the methodology used in the Python script for calculating the performance metrics

calculated by adding the outcome of the window length multiplied with the sampling frequency to the start value. After defining the start and final location, the rate of change can be calculated as follows:

$$RoC = abs(\frac{End\_value - Start\_value}{\Delta t}) \tag{3.5}$$

where End_value and $Start\_value$ are the value of the array at the end and start sample and Δt is equal to t_w.

The window of the signal is moved over the full measured signal by adding the $step$ to the start and end sample until the end is reached. For every step, the rate of change will be calculated. If the end of the signal is reached, the highest rate of change value is returned to the core function.

The core function can be found in App. A.2. The purpose of this function is to generate a table containing all calculated performance metrics per converter for each scenario. For this function, 5 inputs are required. The first one is $Cases$, this is an array consisting of the unique identifier for each disturbance case. The second input variable is the $scen$, this is used find the address of the measured data. The $scen$ variable defines the settings of the system during the simulation, for example "base" or "Pref110". The third input ($name$) is related to the system settings. This input is a string stating how the settings are called. For example "Base case" or "Active power reference 110 %". Finally, the window lengths for the RoCoF (t_f) and RoCoV (t_v) are defined.

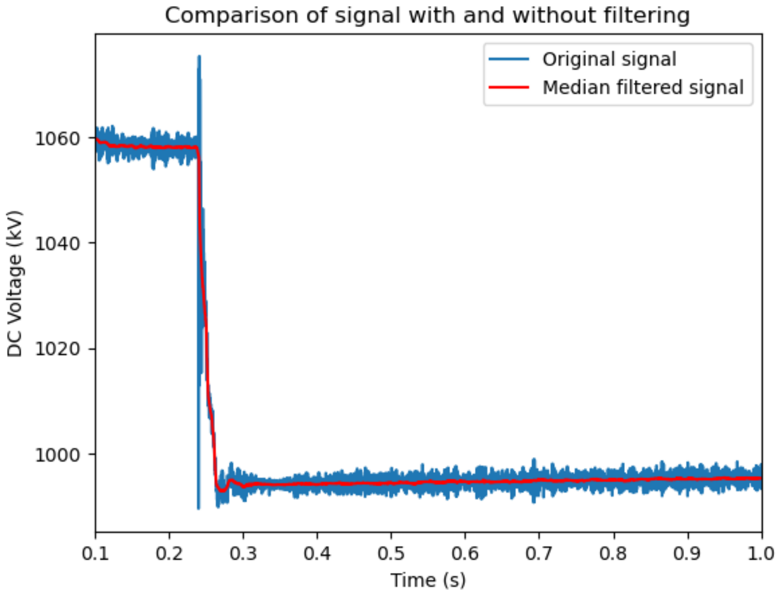

Figure 3.4: Comparison of signal with and without median filtering

In order to ensure that each metric is in the right row, Python dictionaries are used to store the calculated value for each case. The advantage of using dictionaries in Python is that each individual calculated value can be given a unique identifier, which is the disturbance case. After defining a dictionary for each metric, a for loop is used to calculate the metrics for each disturbance. Each dictionary identifier will be the *cas*. This ensures that when generating the table, the values of each disturbance will be placed in the same row.

The first step in the for loop is to obtain the data from the simulations. Each simulation case has a unique CSV file. The name of this file is a combination of the system settings (*scen*), the disturbance case (*cas*), and the location of the measurement. Secondly, the noise will be removed from the signals using a median filter. The main idea of the median filter is to run through the signal entry by entry, replacing each entry with the median of neighboring entries [59]. Fig. 3.4 shows an example of the effect of applying a median filter to an input signal.

Then the filtered signal is sent to the rate of change function. For calculating RoCoF, a window length of 0.5 *s* is used. The choice for 0.5 *s* is based on the guidance document of ENTSO-E for determining the value of RoCoF [60]. A window period of 0.5 *s* is the most commonly accepted and used for measuring RoCoF values in power systems.

In protection schemes, the time window of the RoCoV corresponds with the typical measurement sampling period (in the order of a few ms), to ensure a fast protective action. This time window is too short to provide a clear insight into the impact of the dynamic response of the DC voltage during a disturbance. Therefore, a relatively longer time window is considered in this thesis, in line with the typical reaction time of primary DC voltage control. After conducting several EMT simulations, it turned out that T can be within 0.1-0.4 s, due to the steep DC voltage deviation caused by an abrupt power imbalance [57]. For this thesis, a window period of 0.25 s will be chosen.

After finishing the for loop, all calculated values are combined in the final table. The final table is generated by creating a larger dictionary that combines all dictionaries. By converting the large dictionary to a Pandas dataframe, the final table can be returned as output.

4

Implementation of Test System

The test system plays a critical role in evaluating the dynamic response of a hybrid AC/DC system, and must therefore be carefully chosen. A detailed understanding of the test system is essential to evaluate the results obtained and draw meaningful conclusions. For this thesis, CIGRE's working group B4.72 BM1 model is chosen as the test system. The BM1 model is designed for the integration of large-scale onshore renewable generation [61].

In this chapter, the implementation of the test system will be discussed. But before introducing the test system in detail, the RSCAD® FX environment will be introduced in section 4.1. The remainder of the chapter will discuss the implementation of the test system. An overview of the taken steps is shown in Fig. 4.1. The first step on the implementation of the CIGRE BM1 model will be discussed in section 4.2. Secondly, the implementation of the disturbances will be discussed in section 4.3. Thirdly, section 4.4 will discuss the implementation of the sensitivity analyses. Finally, the developed RSCAD® FX script for automatic operation will be discussed in section 4.5. This chapter will be concluded with the boundaries and limitations of the model. This will be discussed in the section 4.6.

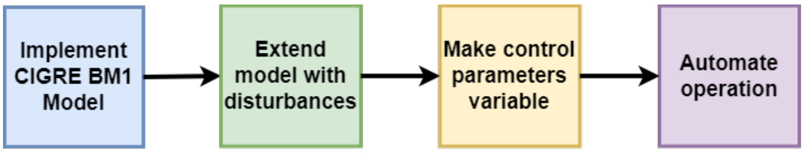

Figure 4.1: Overview of steps in the implementation of the test system in RSCAD® FX

4.1. RSCAD® FX environment

To simulate power systems, two types of models can mainly be used: RMS models and EMT models. Root mean square (RMS) simulations are performed to analyze electromechanical phenomena. RMS-based simulators assume that the system operates at the fundamental frequency and ignores other harmonics and DC components. Therefore, the RMS approach reduces the computational burden for fast transient simulation of power systems, but it is not sufficiently accurate to capture the stability issues of power electronic converters [62].

Therefore, an EMT-based solution will be used in this thesis. EMT simulations consider unbalanced operating conditions, non-linear phenomena, and precise dynamics of power electronics in the power system [62]. The range of dynamic phenomena and their applicability for either EMS or EMT type of models are shown in Fig. 4.2.

In order to perform EMT calculations, the RTDS tool from the TU Delft will be used. RTDS stands for Real Time Digital Simulator, which requires a dedicated server to perform the simulations. Within the faculty of EEMCS, the RTDS servers are available. A real-time simulator needs to achieve a computation time step, smaller than or equal to the time step itself [63]. The RTDS servers make use of high-speed digital signal processor chips and a reduced instruction set computer in order to achieve real-time computational speed. In addition, cutting-edge parallel processing techniques are used [64].

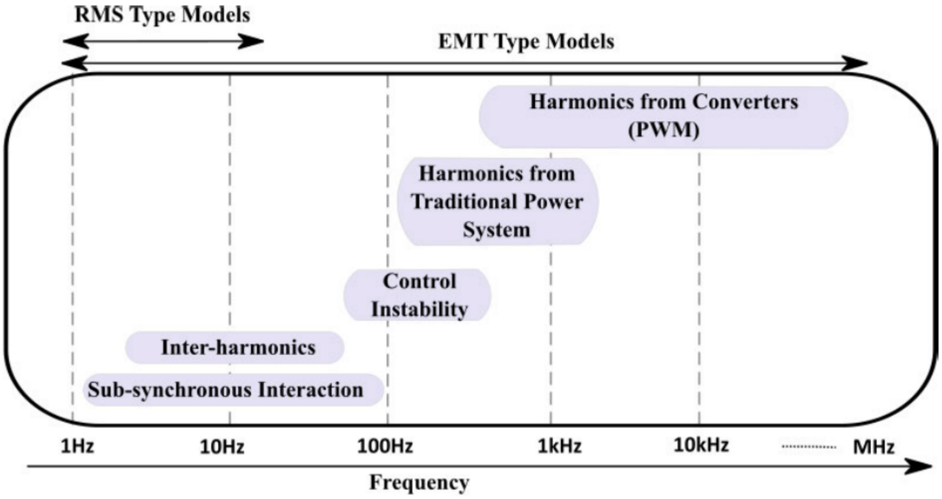

Figure 4.2: Dynamic phenomena and applicability of EMT and RMS tools [62]

At the faculty of EEMCS, 6 racks using PB5 cards are available and 4 racks using NovaCor chassis are available. The PB5 card consists of 2 Power PC RISC processors. Each processor is running at 1.7 GHz. The PB5 cards provide increased network solutions and component modeling capabilities. Each network solution can consist of a maximum of 72 nodes, which means a total of 144 nodes per PB5 card. Within a single rack, this can be increased to a total of 180 nodes [64].

A NovaCor chassis contains an IBM Power8 processor with 10 cores, operating at 3.5 GHz. The 10 cores are used to solve the overall network solution, and auxiliary components (i.e. machines, transformers, transmission lines, etc.), as well as the controls present in the simulation. On the NovaCor chassis, 2 network solutions are allowed. Each network solution can solve up to 300 nodes, making a total of 600 nodes per NovaCor chassis [64].

In order to perform simulations on the RTDS servers, RSCAD® FX is used. RSCAD® FX is the user interface for the RTDS servers. It includes several modules that are designed to enable the user to prepare, run and analyze simulation cases [33]. In RSCAD® FX, EMT calculations can be performed over a frequency range from 0 (DC network) to 3 kHz. Typically, EMT programs work with a time step between 25 and 50 μs. However, fast-switching power electronic devices present in current converters require more detailed computations. Therefore, the RSCAD® FX provides a library with small time-step models that work with a time-step between 1 and 4 μs [65]. For this thesis RSCAD® FX version 1.3.2 is used.

The RSCAD® FX software offers the option of tuning parameters during simulation, by using sliders, switches and dials on the dashboard. It is also possible to perform simulations from a script. The script can be written in a text file, using the RSCAD® FX scripting language. Another possibility is to write scripts on other platforms such as Python or Matlab [65].

4.2. CIGRE BM1 Model Implementation

This section will provide a detailed description of the test system that is used for the analysis. For this thesis, the CIGRE BM1 benchmark model is used as the test system. The design of the BM1 model can be seen in Fig. 4.3. The BM1 model is designed as a 5-terminal (4 AC/DC terminals and 1 DC/DC terminal) bipole MTDC system. As converters, the model uses MMC half-bridge converters. The DC grid lines are rated at ± 500 kV, the AC grid equivalent GE-A0 is rated for 750 kV and GE-A4 is rated for 220 kV [43].

The MTDC system consists of five DC buses. The three buses 1, 2, and 3 form one DC mesh. In addition, two DC radio branches (bus 1 to bus 5 and bus 3 to bus 4) are connected to complete the grid. The five DC buses are interconnected via five DC overhead lines. The lengths of each line are shown in the figure [43].

Two wind farms are connected to the model at A1 and A4 via AC/DC converters. Converters MMC-2 and

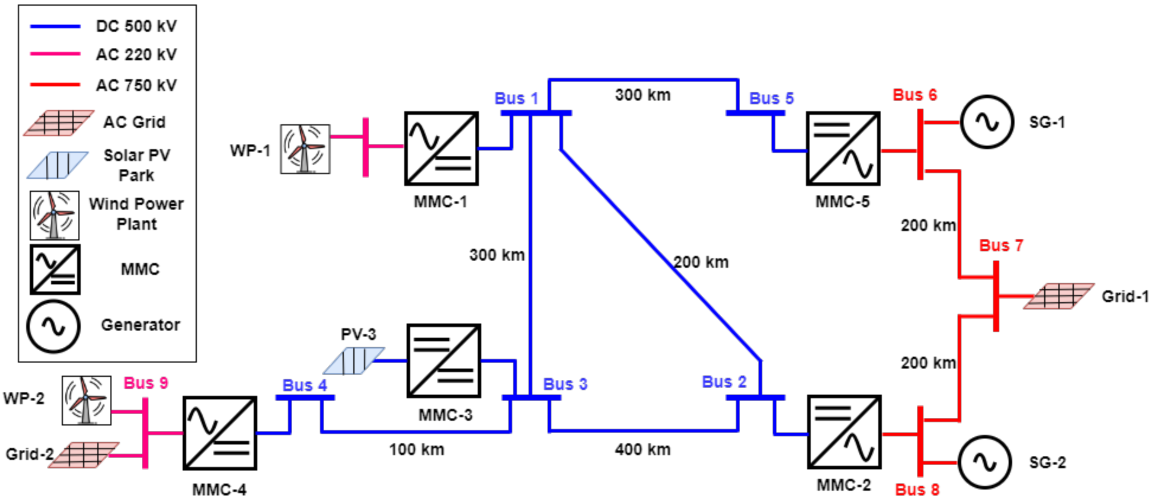

Figure 4.3: Multi-terminal HVDC test system B4.72 BM1

MMC-5 connect the equivalent grid grid-1 via 2 overhead AC line connections. In addition, at each converter, a conventional generator is connected. A solar photovoltaics (PV) park is connected to the system via a DC/DC converter MMC-3 [43]. The remainder of this section will discuss the implementation of each element in the test system.

4.2.1. Converter Model

The BM1 model consists of 5 converter stations that transform AC voltage to DC voltage and vice versa. All converter stations make use of MMC-based converters. In section 2.1.1, different types of MMC models are discussed. For the purpose of this thesis, a type 4 model is the most suiting type of MMC model. Within RSCAD$^{®}$ FX , four types of MMC models can be chosen for different applications. The different models are summarized in table 4.1. For the purpose of analyzing the dynamic response of hybrid AC/DC systems and analyzing the influence of the outer control loop parameters, the MMC5 is the most suitable option. The other 3 models are too detailed and would use too much computational efforts.

The U5 model	**The MMC5 model**
Detailed equivalent model	Simplified model
Requires individual SM firing	Assumes internal capacitor voltages are balanced
Supports up to 3 valves	Mainly for testing upper level controls
The GM model	**The CHANV5 model**
Detailed equivalent model	Detailed equivalent model
Quite similiar to U5 model	Modelled as a Norton's equivalent
Each SM IGBT switch can be controlled individually	Requires low level capacitor balancing control

Table 4.1: Overview of available MMC models in RSCAD$^{®}$ FX [33]

The MMC5 model is referred to as the simplified model in RSCAD$^{®}$ FX as it is less complex compared to the other 3 models. For this model, the assumption is made that the capacitor voltages in each sub-module is balanced internally [33]. The control input of the model is simplified to to an overall deblock integer signal and the number of sub-modules to be inserted. This model is designed specifically for testing high-level controls and system performance. The added benefit is that less hardware is required [66]. The MMC5 model is modelled on the small time step interface of RSCAD$^{®}$ FX .

For the implementation of the converters in the BM1 test system, each converter uses 12 sub-modules (6 per DC pole). The RSCAD$^{®}$ FX icon for 1 submodule is shown in Fig. 4.4. The CIGRE brochure [43] about the design of the BM1 model presents the ratings of each converter and the initial settings. These are shown in table 4.2.

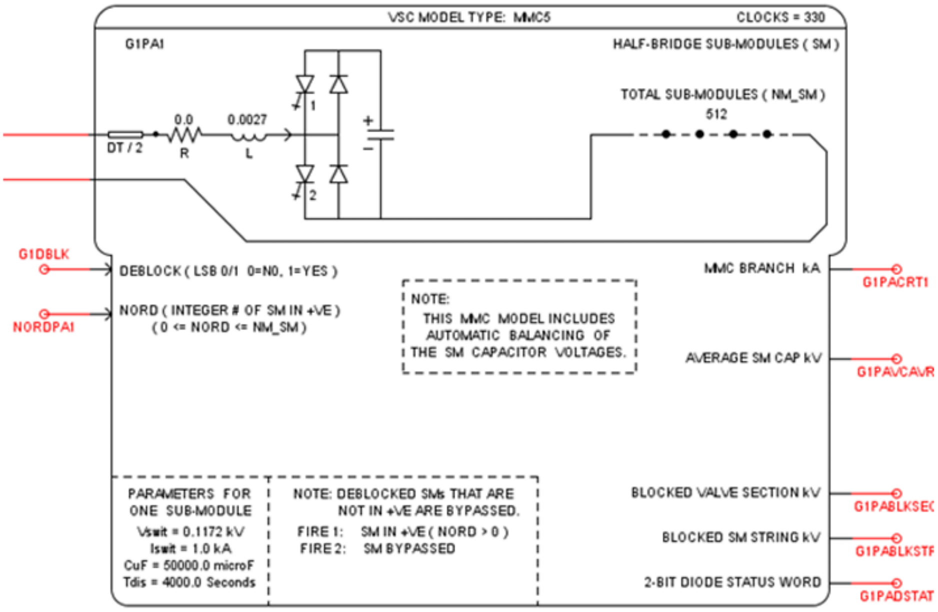

Figure 4.4: Icon of MMC5 sub-module in RSCAD® FX [65]

Converter	Type	Rating (MW)	Setting
MMC-1	MMC bipole	2500	P = 1800 MW, Q = 0
MMC-2	MMC bipole	5000	Vdc = 1 p.u., Q = 0
MMC-3	Back to back MMC bipole	2500	P = -1500 MW
MMC-4	MMC bipole	2500	P = -1500 MW, Q = 0
MMC-5	MMC bipole	2500	P = 2000 MW, Q = 0

Table 4.2: Converter setpoints and ratings for CIGRE BM1 model

4.2.2. Transmission lines modelling

In section 2.1.2 the modeling of DC transmission lines and cables is discussed. In order to represent the fast transients of HVDC cables and lines, the most detailed possible must be used in the model. In the CIGRE BM1 model, all transmission lines and cables are modeled as frequency-dependent traveling waves. Frequency-dependent lines and cables provide more accurate results when observing transient events. However, they carry a higher computational requirement [32].

In RSCAD® FX it is possible to create line models based on given parameters. Within RSCAD® FX there are two frequency-dependent models. The first one is the frequency-dependent mode model (FDMM) and the other is the frequency-dependent phase model (FDPM). The main difference is that FDPM represents the frequency-dependent nature of the internal transformation matrix. Therefore, FDPM is used to represent the transmission lines in the BM1 model [65]. For the BM1 model, the lengths and line parameters are taken from the CIGRE brochure [43] about the BM1 model. The parameters of the lines are shown in Table 4.3.

Line type	Rac (Ω/km)	Xac (Ω/km)	Bac (S/km)	Rdc (Ω/km)	Max Current (kA)
DC ± 500 kV				0.0062	5.0
AC 750 kV	0.013	0.261	4.12e-8		5.27
AC 220 kV	0.040	0.304	1.85e-6		1.76

Table 4.3: Transmission line data for CIGRE BM1 model

4.2.3. Generator and equivalent grid modeling

The BM1 model has 2 equivalent grids included and 2 generators. These are all modeled as synchronous generators. In the original model, the grids and generators were modeled as voltage sources. However, a realistic representation of the AC side should include an inertia constant for a realistic response. The voltage source model does not provide this option in RSCAD® FX . Therefore to prevent the model from showing unrealistic responses on the AC side the synchronous generators are used to replace the voltage source as equivalent grid.

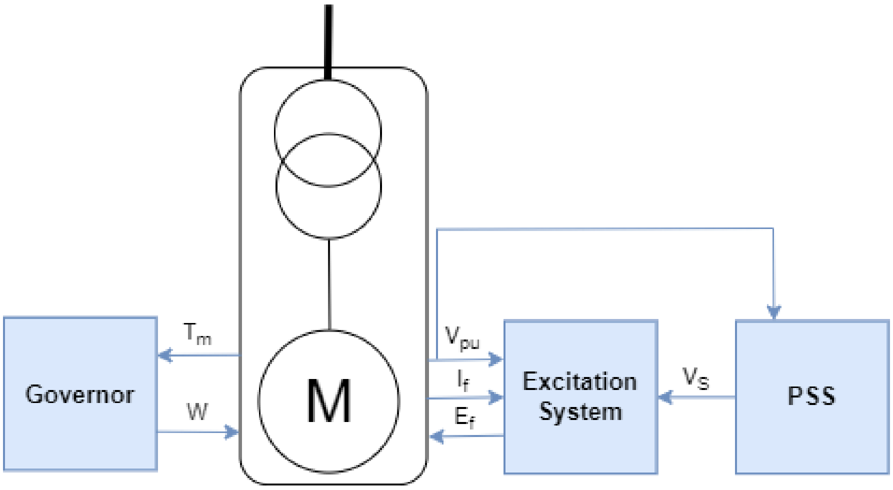

Figure 4.5: Schematic representation of the implementation of synchronous generator in RSCAD® FX

The synchronous generators are controlled by a power system stabilizer, excitation system, and governor. In Fig. 4.5, the connection of the control models to the synchronous generator can be seen. The governor is the IEEE type 1 model. In App. B.3, the block diagram of this controller can be found. For the excitation system, the IEEE type ST1 model is taken from the RSCAD® FX library. In App. B.2, the block diagram of the ST1 exciter can be found. The power system stabilizer taken from the RSCAD® FX library is the IEEE2ST model. The block diagram of the IEEE 2ST PSS model can be found in App. B.1. The parameters are kept to the standard of the IEEE models and can be found in Table 4.4. The only parameter that is adapted is the inertia constant for the generator. Based on the inertia values in [67], a value in the higher range is chosen to represent a strong AC grid. Therefore the inertia constant is set to 8.7 MWs/MVA.

Component	**Parameter**	**Value**
Generator	Rating	10000 MVA
Generator	Inertia constant	8.7 MWs/MVA
Generator	Stator leakage reactance	0.2327 p.u.
Governor	Gain	20
Governor	Lag time constant	0.001 sec
Governor	Lead time constant	0.001 sec
Governor	Valve positioner time constant	0.250 sec
PSS	Gain K1	10
PSS	Gain K2	0
PSS	Time contsnat T3	10.0 sec
Exciter	AVR lead time constant	1.00 sec
Exciter	AVR lag time constant	20.0 sec
Exciter	Voltage regulator gain	200

Table 4.4: Synchronous generator settings for the CIGRE BM1 model

4.2.4. Wind farm and PV modeling

Within the BM1 model, 2 wind farms and 1 solar PV park are included. The Wind farm models are simplified as an AC voltage source with a source impedance. The icon for the AC voltage source in RSCAD® FX is shown in Fig. 4.6. The AC source feeds into the MMC converter which controls the active and reactive power. The PV park is represented as a DC voltage source in series with a DC/AC inverter. Simplifying the modeling of renewable generation is sufficient since the emphasis is on the analysis of the dynamic response of the system, and not the renewables. This will reduce the computation requirement of the model and limit the amount of hardware required. For the voltage sources, the impedance has to be provided. For the wind farm WF-A1, this is set to 0.333 Ω and for the other wind farm WF-A4 and solar park PV-A3, the source impedance is 0.001 Ω. The source impedances are taken from the CIGRE brochure [32]. The settings and ratings of each generator in the system are taken from the CIGRE brochure [43] and can be found in table 4.5.

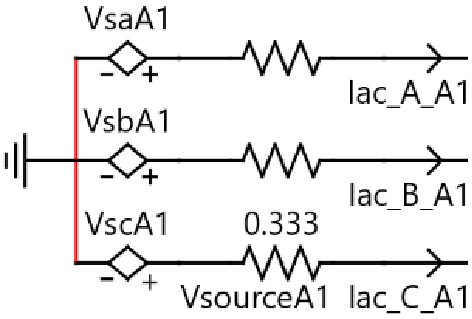

Figure 4.6: Icon for AC voltage source with a source impedance, used to represent the wind farms

Name	Generator type	Rating (MW)	Setting (MW)
SG-1	Synchronous generator	3000	3000
SG-2	Synchronous generator	3000	2000
WP-1	Wind-farm	2500	1800
WP-2	Wind-farm	2500	1600
PV-3	PV	2500	1500

Table 4.5: Generator setpoints and ratings for CIGRE BM1 model

4.2.5. Control system design

This section will describe the control system of the BM1 model. The main objective of the control system is to keep the system within operation boundaries. The control design of the system is split into 2 parts: converter control and MTDC system control.

Converter control

Firstly, the control of the converters will be discussed. Each converter makes use of the same control system. For the converters, a vector-oriented control strategy is used. The controller exists of a fast inner control loop and a slower outer control loop. A general overview of the upper-level control can be seen in Fig. 2.4.

The first step in the control of the converter is the conversion of the incoming signals to per-unit values. This is done by dividing the incoming measurement by the base. Secondly, the 3-phase quantities have to be transformed into the dq0-frame. Within RSCAD this can be modeled by using a Clark transformation block, as shown in Fig. 4.7.

The generated dq quantities are sent to the decoupled current controller, where they will be compared with i_{d_ref} and i_{q_ref}. The reference currents are calculated in the outer control loop. This design is based on Fig. 2.5. Each converter is equipped with active power, DC voltage, reactive power, and an AC voltage control loop. The PI controllers are designed as anti-windup PI controllers, as shown in Fig. 4.8. In a PI controller

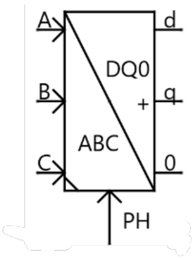

Figure 4.7: ABC-DQ0 transformation block in RSCAD

working under saturation, problems like windup or rollover arise. Hence anti-windup schemes are necessary to minimize performance degradation [68]. In this design, the PI controller uses a feedback loop to unwind the PI controller block when the controller hits specified saturation limits and enters nonlinear operation [69]. The values of K_p and K_i differ for each control loop. In Table 4.6 the parameter settings of the PI's per control loop can be found. The settings are chosen based on the provided control settings in [43].

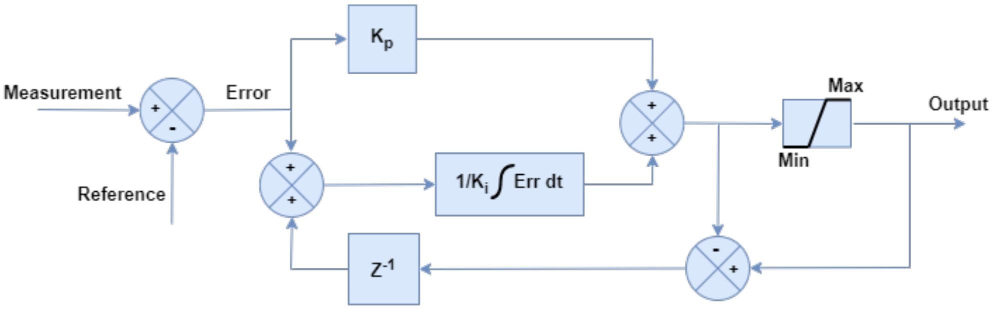

Figure 4.8: Design of the PI block

Control parameter	DC voltage control	Power control	Reactive power control	AC voltage control
Kp (p.u.)	14	0	1	1
Ki (s)	0.2	0.0303	0.0303	0.1
Deadband gain (p.u.)	-	14	-	-
Deadband width (%)	-	5	-	-

Table 4.6: Parameter settings of the converter controllers

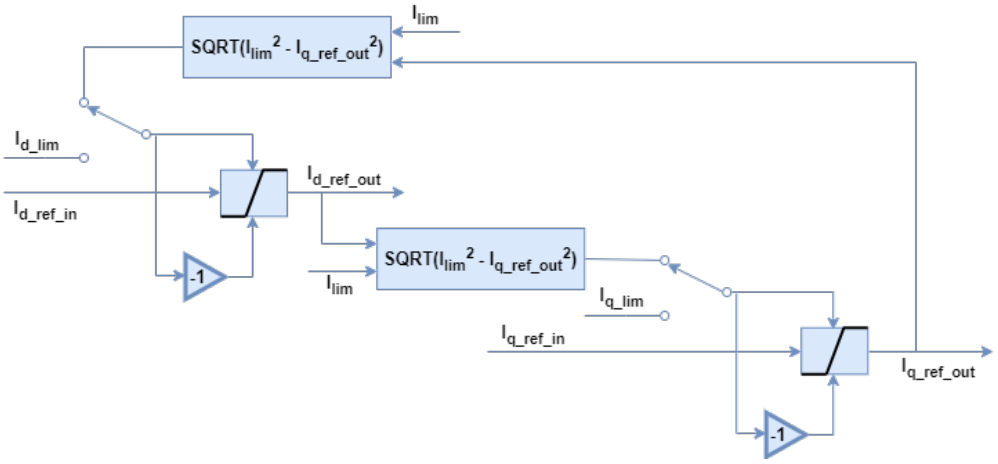

Figure 4.9: Design of the i_{dq} limiter block

The generated i_{d_ref} and i_{q_ref} reference currents are sent to the i_{dq} limiter block. In this block, it is ensured that the reference currents do not exceed the limitations of the converter. In addition, it offers the possibility to give priority to either reactive power or active power. This can be adjusted by changing the switch, as shown in Fig. 4.9. If the switch is changed, the reference current of either i_{d_ref} or i_{q_ref} is forced to 0 due while the other is maximized.

The out-coming $i_{d\_ref\_out}$ and $i_{q\_ref\_out}$ signals from the limiter block are sent to the decoupled current controller. The implemented design of this part is shown in Fig. 4.10. The output reference voltages are finally sent to the transformation block (same as in Fig. 4.7) and are transformed to ABC quantities. The ABC quantities are used as reference values for the lower level control of the converter. However, in this model, no lower level control is added, so the references are directly used in the model.

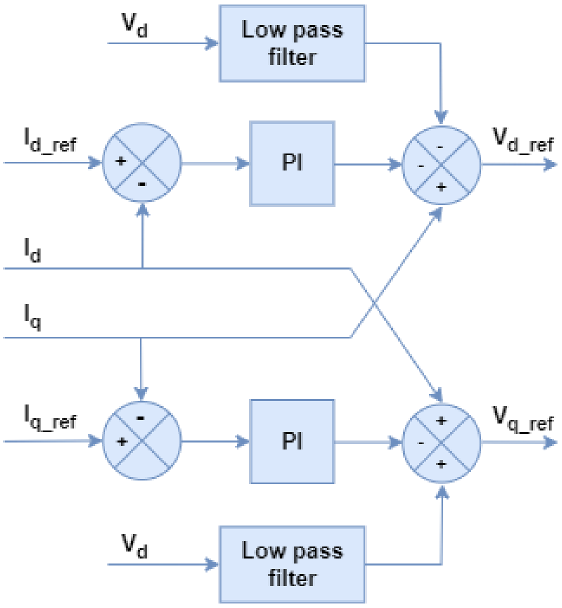

Figure 4.10: Design of the decoupled current controller block

MTDC system control

As a general control concept, the master-slave control method is used to control the DC network. The converter MMC-2 is set as DC voltage control in the positive and negative terminal, both are controlled independently of each other. All other converters are set with active power control on the d-axis. Converter MMC-2 was chosen because there are renewables generators connected at converters MMC-1, MMC-3, and MMC-4 that operate with constant power without extra room for adapting to the power changes in the system. Converters MMC-2 or MMC-5 can both be chosen to control the DC voltage, as there are conventional generators connected to their corresponding AC busbars. As there are more lines connected to the bus 2, this is the preferred location for DC voltage control. On the AC side, the converters are equipped with reactive power control and AC voltage control. For each converter independently, one of these control modes can be chosen. In the base scenario, all controls for the AC side are set to reactive power control [43].

4.2.6. Measurements of DC Voltage and Frequency

In order to calculate the performance metrics, the DC voltage and frequency must be measured in the model. Within RSCAD, it is easy to obtain the DC voltage at the output of the converter. By adding a blue measurement dot, the voltage of that point is measured by RSCAD. In order to obtain the difference between the positive and the negative terminal, a signal $EdcbA5$ is calculated as shown in Fig. 4.11. This signal is used as a measurement of the DC voltage at the output of every converter.

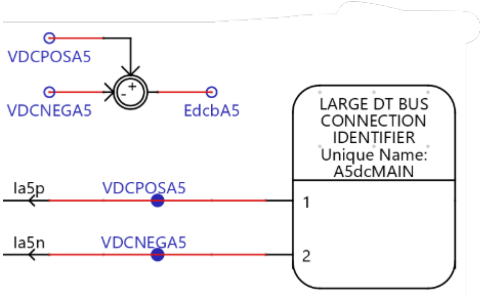

Figure 4.11: Implementation of voltage measurement

For the frequency, the same type of methodology is used as for measuring the DC voltage. Only this time the AC voltage measurement is connected to a frequency meter. This is shown in Fig. 4.12. The meter type is set to DFT (discrete Fourier transform). The output of the meter will be used to calculate the RoCoF.

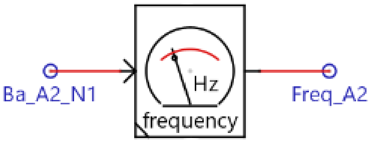

Figure 4.12: Implementation of frequency measurement

4.3. Disturbance Implementation

In this section, the implementation of the disturbances will be discussed. The impact of the different implemented disturbances will be analyzed using the performance metrics. For this thesis, 2 types of disturbances will be implemented: outages and short-circuit faults. In section 4.3.2, the short-circuit faults will be discussed in section 4.3.1. Secondly, the implementation of the outages will be discussed.

4.3.1. Short-Circuit Faults

The second type of disturbances that are implemented in the test system, are short-circuit faults. The short-circuit faults that will be implemented on both AC and DC sides are line-to-line and line-to-ground. On the AC side, a line-to-line fault is implemented as a line-to-line fault between phases A and B. The line-to-ground fault will be implemented as a 3 lines-to-ground fault. On the DC side, a line-to-line fault is between the positive and the negative line. The line-to-ground fault is implemented as a positive line-to-ground fault. For realistic implementation of the faults, circuit breakers will be placed to isolate the faulted section.

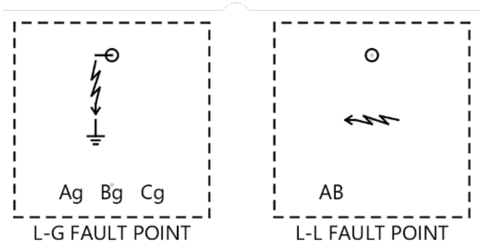

Figure 4.13: Icon of short-circuit faults in RSCAD

The RSCAD® FX short-circuit icons are shown in Fig. 4.13. The block will be connected to the location of the fault and will be surrounded by breakers. The breakers used for the implementation of outages are used for isolating the faults. In the settings of the fault, a control signal must be defined to activate the fault and the fault resistance must be defined. The fault resistances are taken from the guide for the development of HVDC models [32]. In this guide, low fault resistances are used. This will result in a larger fault current. The fault resistance of line-to-line faults is set to $0.1\,\Omega$. For line-to-ground faults, the resistance is set to $1\,\Omega$.

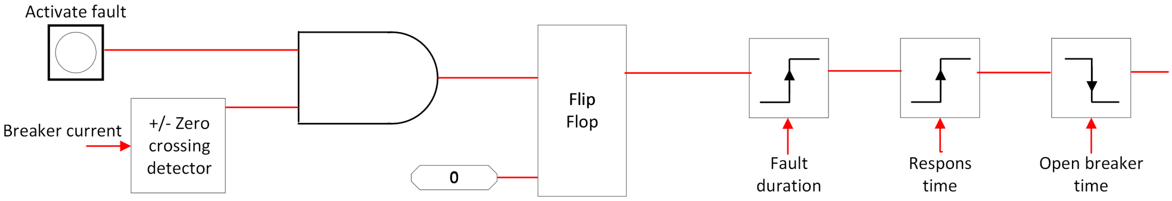

Figure 4.14: Design of control logic in RSCAD for activating breakers

For the operation of the breakers to isolate the fault, a control logic scheme is developed in RSCAD® FX . The control logic can be found in Fig. 4.14. The scheme can be used for both AC and DC side short circuits. If the push button to activate the fault is pressed, the output of the AND gate will become one once the zero-crossing output is also 1. For faults on the DC side, this is set to be a constant 1. The outcoming 1 will trigger the first step function, making the LGFLT signal 1. The period of the fault duration can be adjusted using the slider. The LGFLT signal will trigger the short-circuit block, and the fault will be executed. This will trigger the second step function for the breaker response. This step function will be activated with a specified delay. The delay is adjusted by the BRK_RESPONSE slider, which is used to define the response time of the breaker. Finally, the breaker will be closed again using the last step function. This one is also activated with a specified delay BRK_TIME.

For the AC side faults, the breaker response is set to a typical breaker response time of $40\,ms$. The fault on the AC side should be cleared after another $40\,ms$. Therefore the opening time of the breaker is set to $40\,ms$ as well [70]. On the DC side, faults are cleared after $10\,ms$. In the DC system, fault currents can obtain high values in a short period. In order to maintain safe operation the faulted section should be cleared within $10\,ms$ [71]. The $10\,ms$ is divided into a breaker response time of $5\,ms$ and an opening time of $5\,ms$.

4.3.2. Outages

The first type of disturbance that will be implemented is the outage of different components in the system. The implementation of any component outage is the same. The only key difference is whether the component is on the AC side or the DC side. Therefore, this section will only go into the implementation of the outage. In the next chapter, the different disturbances cases will be explained.

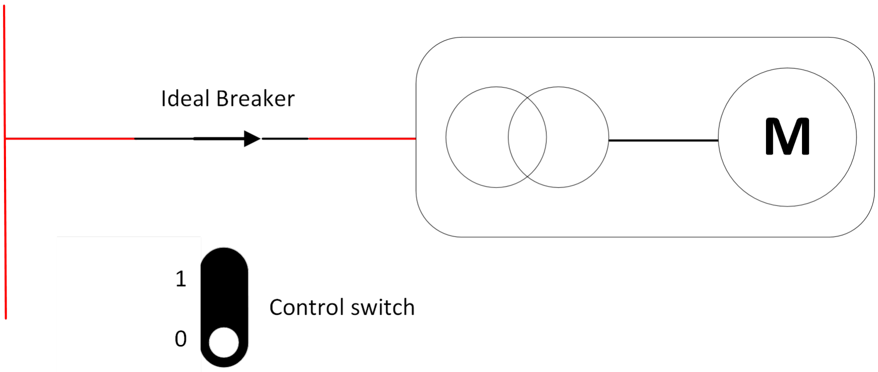

Figure 4.15: Implementation of outage on the AC side

AC Side Outage

For an outage on the AC side, ideal breakers will be used to disconnect any component from the system. It is chosen to use ideal breakers instead of a realistic circuit breaker, as it is only of interest to disconnect the component. The dynamics of a circuit breaker would influence the process of disconnection and is therefore not used for the implementation of an AC side outage.

On both sides of the component, the ideal breaker is placed. The control signal of both breakers will be the same, such that in the automatic operation process they can easily be activated. The breakers can be controlled by adding an integer switch in the simulation window of RSCAD® FX . The implementation of an AC side disturbance is shown in Fig. 4.15.

DC Side Outage

For an outage on the DC side, using an ideal breaker is not possible. The DC system in RSCAD® FX is modeled in the small time step environment, where the ideal breaker is not designed to work in the small time step environment. Therefore, an actual model of a DC breaker must be used. Within RSCAD® FX a hybrid DC breaker model is available to use in the small time step environment [72]. The RSCAD® FX icon for the hybrid DC breaker is shown in Fig. 4.16. A detailed description of the hybrid model can be found in App. C.

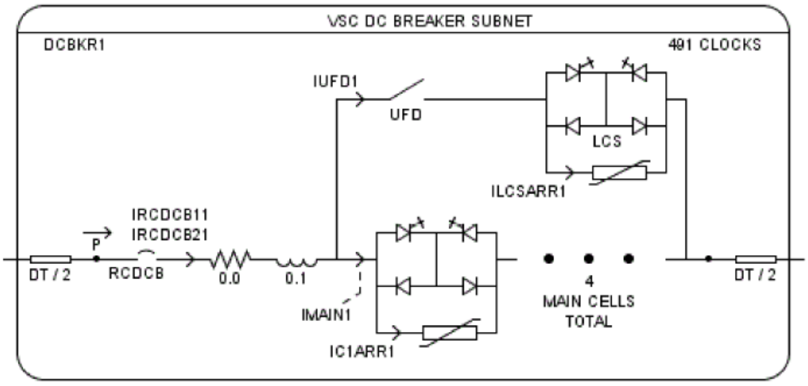

Figure 4.16: DC Circuit breaker model used for the implementation of an outage on the DC side

In order to limit the dynamic effects of the DC circuit breaker on the response of the system as much as possible, the parameters of the model have been adapted. The breaking capability of the breaker is set to $20\,kA$, to ensure that it will always break the current. In addition, the response time is set to $0\,s$. This way, the DC breaker will operate as ideal as possible. The rest of the implementation process is comparable to the AC side outage. Again, a breaker is placed on both sides of the component and is set to use the same control signal. The control signal will be connected to a switch such that it can be controlled during operation.

4.4. Implementation of Sensitivity Analyses

After applying the different disturbance cases to the system, the worst-case AC and DC side disturbance will be used for the parametric sensitivity analyses. For this purpose, the control parameters in the outer loop will have to be made variable. As the different control variables are the same in every converter, 1 slider per parameter must be created. The slider can be controlled in the automation script.

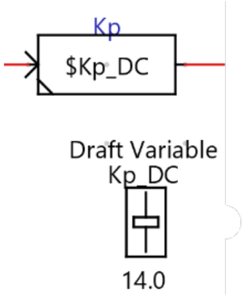

Figure 4.17: Implementation of $Kp_DC in RSCAD® FX

In order to make the control parameters a variable, in RSCAD® FX a dollar sign must be placed in front of the chosen signal name. So for example $Kp_DC. In order to control the variable, a slider must be created with the exact same signal name, but without the dollar sign. So in this case the slider would be named Kp_DC. This will be done for all parameters in the outer control loop. The range of the sliders will be set from 0 to 100, such that a broad scope of parameters can be tested. In Fig. 4.17, an example of the implementation of $Kp_DC in RSCAD® FX is shown.

4.5. Automatic Operation

The final step in the implementation of the test environment is to automate the operation. For this purpose, an automation script is developed in RSCAD® FX . Within RSCAD® FX it is possible to record your actions and repeat this when starting the script. The run menu of an RSCAD® FX script can be seen in Fig. 4.18. In the figure, the relevant buttons are explained.

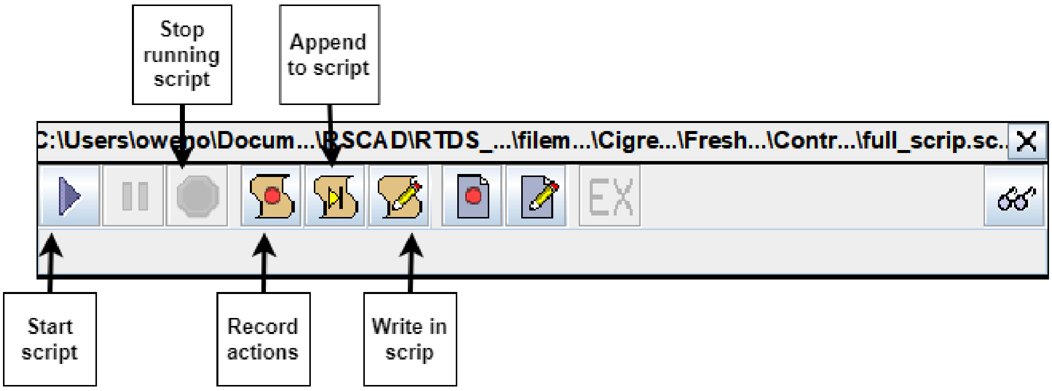

Figure 4.18: Run menu for scripts in RSCAD® FX

Figure 4.19: Overview of the methodology of the automation of disturbances

The overall process of the automation script can be seen in Fig. 4.19. The final script is built up by appending such a code block for each disturbance. The first step in a code block is setting all variable values. This is done by recording the setting of the values of each slider. This results in the following RSCAD® FX code:

```
SetSlider "DraftVariables : Kp_DC" = 14.0;
SetSlider "DraftVariables : Kp_PWR" = 0.0;
SetSlider "DraftVariables : K_dead" = 14.0;
SetSlider "DraftVariables : Ki_PWR" = 1.0;
SetSlider "DraftVariables : Ki_DC" = 0.2;
```

This code can be used as a basis, and parameters can be adapted for each scenario. The second step is starting the script y using the "*start*;" command. This will start the operation of the test system. In order to give the EMT model some time to start the operation of the system, 20 seconds is waited before activating any disturbance. The 20 seconds delay is achieved with the following command: "*SUSPEND* 20.0;".

Once the 20-second delay is over, the script will activate the studied disturbance. This is also done by recording the process of pushing the activate button and adding this to the script. This results in the following code:

```
PushButton "Subsystem #1 : CTLs : Inputs : LG_FLT_A2";
SUSPEND 0.185;
ReleaseButton "Subsystem #1 : CTLs : Inputs : LG_FLT_A2";
```

The release of the push button will activate the disturbance. By changing the LG_FLT_A2 signal name, a different push button can be selected to activate another disturbance. The measurements of the disturbance must now be written to a CSV file, such that it can be used in the Python script. Within RSCAD® FX , this is done by converting a plot into a CSV file. The RSCAD® FX code for this looks as follows:

```
SavePlotToCSV "A1 Data",          "Base_LL_A3_DCF_A1_Data";
SavePlotToCSV "A2 Data",          "Base_LL_A3_DCF_A2_Data";
SavePlotToCSV "A4 Data",          "Base_LL_A3_DCF_A4_Data";
SavePlotToCSV "A5 Data",          "Base_LL_A3_DCF_A5_Data";
SavePlotToCSV "Generators",       "Base_LL_A3_DCF_Gen_Data";
```

For each plot, a separate CSV file is created. The name of the CSV file is given a unique name formed according to this structure: "Scenaraio_FaultType_Location_SideOfSystem_MeasurementLocation". This way, it is easy to find the right file for each case. Finally, the run is ended by using the "$stop$;" command.

4.6. Model Boundaries and Limitations

Albert Einstein said: "A model must be as simple as it can be, but not simpler". In an ideal world, a model would be the perfect representation of reality. However, this is not possible. Any model will always make some kind of assumptions and/or simplifications.

The main boundary of this model is the control of the generators in the system. The reference inputs of the control of the converter will decide the amount of generation during normal operation. For example, the generation of the wind farm connected to converter A1 will generate 1800 MW as this is required by the reference of the active power for converter 1. However, in reality, the generation amount of a wind farm can not be controlled. In addition, in case of lost generation or demand, the modeled voltage sources will immediately adapt their generation/demand to restore the balance in the system. When operating a real power system, this is not realistic. Therefore, it will be hard to see the influence of a loss of generation or demand.

Another important note to make on the model is the response of the DC breaker. At this moment, no DC circuit breaker exists in operation that can respond to a fault within 5 ms. It is not even ensured, that a DC fault will be detected in time by the protection. In this model, no protection algorithm is present, and the operation of the DC breaker is always ensured.

The response of the AC side can only be analyzed at the connecting transmission lines between the converter and the equivalent grid. The propagation of fault through the AC system can not be analyzed. In addition, the modeled synchronous generation will adapt its demand to the available generation. In the real world, a customer usually does not take this into account and will consume power when needed. Therefore, the demand of the grid would be more constant. However, modeling this in RSCAD® FX was not possible when using a synchronous generator model.

5

Numerical Results

This chapter will discuss the numerical results of all case studies executed on the test system as described in chapter 4. A general overview of the steps taken in this chapter can be seen in Fig. 5.1. Firstly, section 5.1 will analyze the operation of the model in normal operating conditions, without any disturbances. This will be referred to as the base case. Secondly, all different case studies will be defined in section 5.2. In this section, the different disturbances and control settings will be defined. Following this, the dynamic responses of the system for each disturbance will be analyzed in section 5.3. Finally, in section 5.4, the sensitivity of the control parameters on these worst-case disturbances will be analyzed. This chapter will be concluded in section 5.5.

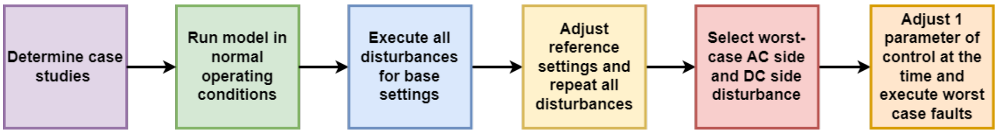

Figure 5.1: Overview of steps taken in this chapter

5.1. Base Case Analyses

The goal of this section is to discuss how the system operates under normal operating conditions. Analyzing the base case of the system is important to understand the response of the system to different types of faults. For the base case, all components are kept in their settings as discussed in section 4.2. The resulting operation state for the base settings of the system is shown in Fig. 5.2.

In the figure, for each generator and equivalent grid, the power generation or consumption is shown. A minus sign indicates power consumption and a positive number stands for power generation. The equivalent grid-1 is the main consumer in this test system, with a demand of almost 10 GW. The largest part of this demand is met by generators SG-1 and SG-2, producing in total 5 GW. The other 5 GW is generated by the renewable energy sources on the other side of the system. The power of the 2 wind farms and PV park is transported to grid-1 via the MTDC system.

The power consumption of grid-2 is much smaller when compared to the consumption of grid-1. Grid-2 consumes only 100 MW of the available power. This demand is fully covered by the wind power plant WP-2. The other 1.5 GW is used for supplying grid-1. The other wind power plant WP-1 supplies 1.8 GW, and the solar PV park PV-3 delivers 1.58 GW.

When analyzing the power flowing through the lines in the DC grid, the line between terminals A1-A5 transfers the largest amount of power. With a load of 80 % the line between terminals A1 and A5 is the closest to be congested. The line between terminals A1 and A2 has the lowest load, with only 40 % (1030 MW) this line has enough room to take some extra power.

The radio line connection between terminals MMC-3 and MMC-4 transfers the 1500 MW from the wind power plant WP-2. The power flow is continued through the line 2-3. From the power flow analyses, it can be seen that the lines 1-5 and 2-3 are transferring the most power, and are therefore the most critical lines. The diagonal line 1-2 can still supply to bus 2 if line 2-3 falls out of service. This is not the case when losing the line 1-5. In this scenario, no power can be supplied to bus 5, and all power will have to be transferred via 2.

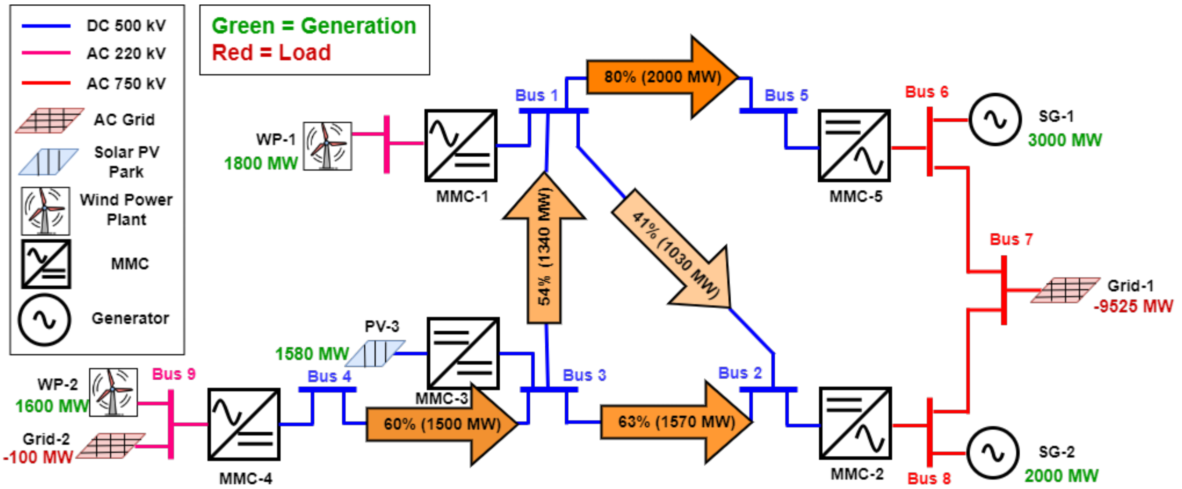

Figure 5.2: Multi-terminal HVDC test system B4.72 BM1 under normal operating conditions

5.2. Case studies

In this section, an overview of the set of scenarios will be presented. The scenarios are split into 2 parts. Firstly, the different faults and outages that will be assessed are explained in section 5.2.1. These scenarios will cover a range of possible disruptions, such as equipment failures and short-circuit faults. Secondly, the different control settings that will be examined are discussed in section 5.2.2.

5.2.1. Type of Disturbance

This section will discuss the faults and outages that will be examined. The type of fault scenarios can be split into 3 categories: conventional faults, converter outages, and line outages.

Firstly, the system will be faced with short-circuit faults. On both DC and AC sides, line-to-line and line-to-ground faults will be executed. Each fault will be executed at different stations at the AC or DC side of the converter. This way the the propagation of the through the DC system can be analyzed. MMC-2 and MMC-5 will be selected to compare the difference and see how it propagates through the AC side. MMC-1 is selected as this bus transfers the most power. Line-to-line faults are implemented as a fault between phases A and B on the AC side. The line-to-ground fault is executed as a 3-lines-to-ground fault. On the DC side, line-to-line faults are executed between the positive and the negative terminal. The line-to-ground fault is implemented as a positive line-to-ground fault.

Secondly, the system will be faced with different component outages. An outage means that during normal operation, a component is lost. In the CIGRE BM1 model, 3 types of components can be taken out of operation: converters, generators, and lines. There are 3 converters chosen to take out of operation. The chosen converters are MMC-1, MMC-2, and MMC-5. These converters are chosen as they have an essential function within the network. Converters MMC-2 and MMC-5 connect grid-1 to the DC network. In addition, converter MMC-2 is responsible for DC voltage control. As converter MMC-1 connects a large wind farm to the grid, this converter is also chosen to be taken out of operation.

For the generator outages, 5 scenarios are defined. The generators that are lost are the wind farm WF-A1, equivalent grids grid-1 and grid-2, and the generators SG-1 and SG-2. The wind power plant WP-1 is chosen as this is the main supplier of power to the DC system, and is therefore interesting to see its influence when taken out of operation. Equivalent grids grid-1 and grid-2 are the only loads in the system. Grid-1 is the largest load and shall have a large impact on the needed generation. On the other hand, grid-2 is largely fed by WP-2 and shall probably have less impact on the DC system. Finally, losing SG-1 and SG-5 is chosen to analyze. They provide strength to the connected converters and therefore have an essential function in the stability of the DC system. Especially, the function of SG-2 is important, as converter MMC-2 is set to DC voltage control.

Finally, the system is faced with line outages. The line outages are executed for 3 different lines, namely the lines between busses: 1-5, 1-2, and 2-3. These three lines are chosen as they play an important role in transferring power from the renewable sources on the left side of the system to the large load GE-A0. A summary of the disturbance case studies can be found in table 5.1.

Side	Type	Location	Goal
DC	Converter outage	MMC-1, MMC-2, and MMC-5	Compare role of DC voltage control/Active power control and effect of losing converter that provides power
DC	line outage	line 1-2, line 1-5, line 2-3	See influence of 3 most essential lines to compare influence of loading and distance
DC	short-circuit	LL and LG at MMC-1, MMC-2, and MMC-5	Analyse propagation through DC system
AC	generator outage	Grid-1, Grid-2, SG-1, SG-2, WP-1	Compare influence of amount of demand/generation and distance
AC	short-circuit	LL and 3LG at MMC-1, MMC-2, and MMC-5	Propagation of AC short circuit through DC system

Table 5.1: Summary of disturbance case studies

5.2.2. Controller Settings

Within the outer loop of the controllers of the converter, 4 types of parameters are adjusted for the sake of sensitivity assessment: proportional gain, integral gain, dead-band gain, and dead-band width.

Parameter	Values	Control loops	Goal
Proportional gain	0, 1, 5, 10, 25, 50, 75, 100	Active power, DC voltage	Check whether adopted metrics can capture influence of proportional gain on initial overshoot, compare proportional gain active power loop with dead-band
Integral gain	1 s, 0,2 s, 0,1 s, 0,04 s, 0,02 s, 0,0133 s, 0,01 s	Active power, DC voltage	Check whether adopted metrics can capture influence of integral gain on settling time
Dead-band gain	0, 1, 5, 10, 25, 50, 75, 100	Active power	Check whether adopted metrics can capture influence of dead-band gain, compare dead-band with active power proportional gain
Dead-band width	0%, 1%, 5%, 10%, 15%, 20%, 25%, 50%	Active power	Check whether adopted metrics can capture influence of dead-band width

Table 5.2: Summary of control parameter settings

From the analyses in the coming section, it will become clear that the frequency response shows to respond within limits in most of the cases. The DC voltage on the other hand shows more unstable responses. In order to improve the response of the DC voltage, the focus is on the control parameters that influence the performance of the DC side. The control of the converters is split into active (d-axis) and reactive power control (q-axis). Only the d-axis has an influence on the performance of the DC grid, as reactive power does not exist in DC systems. Therefore the parameters in the active power control loop will be altered. This means that the K_p and K_i of both DC voltage and active power control loops can be altered. In the active power control loop, the K_p is set to 0 and dead-band control is used. Therefore, 2 more parameters can be altered: the slope of the output and the width of the dead-band. This section will analyze the influence of each parameter.

It is chosen to vary the control parameters over a broad range to minutiously ascertain the influence of diverse controller settings. In table 5.2, a summary of the different considered parameter ranges is shown. If one variable is changed, all other parameters are in their base setting.

5.3. Disturbance Analyses

The analysis in this section will be based on the dynamic responses on the AC and DC side of the converters MMC-2 and MMC-5. Both converters form an essential role, as they connect the main demand (grid-1) to the DC system. This makes it an interesting location in the test system to analyze. The responses at MMC-1 and MMC-3 only have one renewable generator connected, making the response less interesting. In section 5.3.1 the dynamic responses to the outages are discussed and section 5.3.2 discusses the short circuit events. Finally, the values of the calculated performance metrics for different disturbances are compared in section 5.3.3.

5.3.1. Outages

Converter Outages

The response of the DC voltage at busses 2 and 5 can be seen in Fig. 5.3 and Fig. 5.4. The figures show that the outages of the converter furthest away from the bus are the least influential on the dynamic DC voltage performance. This is because the power transfer through the DC system can re-accommodate, so it is not significantly affected by these outages. By contrast, the largest voltage dip at both buses is caused by the outage of the closest converter. These outages cause significant power imbalances (in the order of 2 GW) which can not be re-accommodated by the DC network.

The converter MMC-5 (2 GW) is transferring less power than MMC-2 (2.6 GW), even though the impact of losing MMC-5 is significantly higher than the outage of MMC-2. The drop at bus 2 is around 50 kV for the loss of MMC-2, while the outage of MMC-5 results in a voltage dip of almost 200 kV at bus 5. This difference can be explained by the topology of the DC system. When MMC-5 is lost, no power will flow to bus 5 anymore. In contrast, when losing MMC-2, power can still flow through bus 2. Therefore, this has less influence on the response of the DC voltage.

Looking at the response of the DC voltage at buses 2 and 5 for the outage of MMC-1, both busses show a drop in voltage. At bus 5, a slightly larger dip is observed. This is because most of the power from WP-1 was flowing to bus 5 via line 1-5. In the case of losing MMC-1, this power is lost, thus resulting in a larger dip.

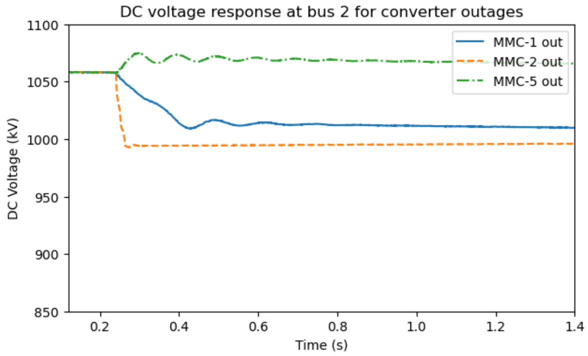

Figure 5.3: DC voltage response at bus 2 for converter outages

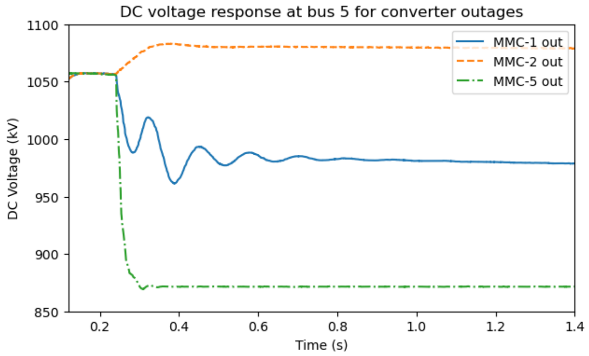

Figure 5.4: DC voltage response at bus 5 for converter outages

The frequency response of the AC system at buses 6 and 8 can be seen in Fig. 5.5 and Fig. 5.6. Just as with the DC voltage, the most influence on the response of frequency is caused by losing the converter closest to the measurement location. The deviation in frequency at bus 8 for losing MMC-2 is larger than the deviation in frequency at bus 6 for losing MMC-5. This is due to the difference in power delivered to the AC system by the converters. As shown in Fig. 5.2, MMC-2 delivers 2600 MW to the system, where MMC-5 delivers 2000 MW. In both cases, the frequency is able to restore quickly. The loss of MMC-1 causes some slow oscillations at bus 8. However, the frequency restores to the base after 0.4 ms. For all other cases, the frequency response remains stable around 50 Hz.

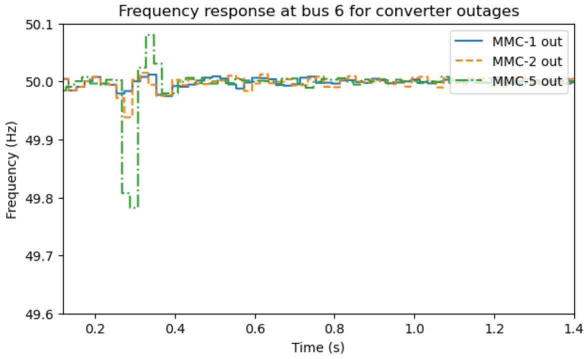

Figure 5.5: Frequency response at bus 6 for converter outages

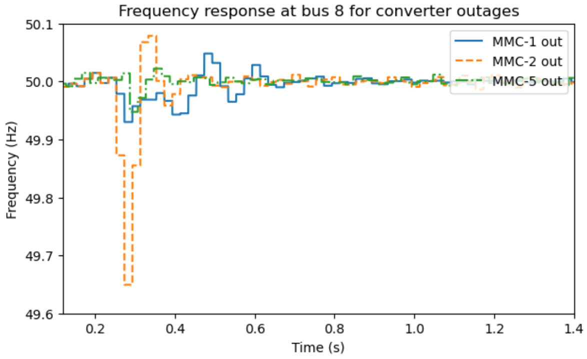

Figure 5.6: Frequency response at bus 8 for converter outages

In table 5.3 the calculated performance metrics are shown for the different converter outages. The values of RoCoV at both buses 2 and 5 match the analysis made on the dynamic responses of the DC voltage shown in Fig. 5.3 and Fig. 5.4. The highest value of RoCoV is observed at bus 5 for the outage of MMC-5, which is also the worst-case graph for the analyzed converter outages.

The calculated RoCoF values all stay below acceptable limits, as none of them even goes over 1 Hz/s. The outage of MMC-2 results in a RoCoF of 0.7080 Hz/s at bus 8, and the outage of MMC-5 results at a RoCoF of 0.4470 Hz/s at bus 6. This also matches with the difference in frequency dips shown in Fig. 5.5 and Fig. 5.6.

Disturbance	RoCoF bus 6 (Hz/s)	RoCoF bus 8 (Hz/s)	RoCoV bus 2 (kV/s)	RoCoV bus 5 (kV/s)
MMC-1 outage	0.01092	0.1700	187.5	321.2
MMC-2 outage	0.01136	0.7080	261.1	113.7
MMC-5 outage	0.4470	0.1354	53.16	755.8

Table 5.3: Overview of calculated performance metrics for converter outage

Generator Outages

The response of the DC voltage at bus 2 can be seen in Fig. 5.7, and at bus 5 in Fig. 5.8. The first thing that stands out is that the outage of SG-A2 causes significant and highly oscillatory DC voltage deviations at both buses. This is attributed to the electrical proximity of SG-2 to MMC-2, which affects significantly the power balancing at MMC-2, adversely lowering the effectiveness of the DC voltage control, which is dictated by MMC-2. Without the strength of SG-2, the controller of MMC-2 can not stabilize the DC voltage. By contrast, the outage of a similar generator SG-1 has almost no influence on the dynamic response of the DC voltage. The system oscillates shortly and settles to a stable value.

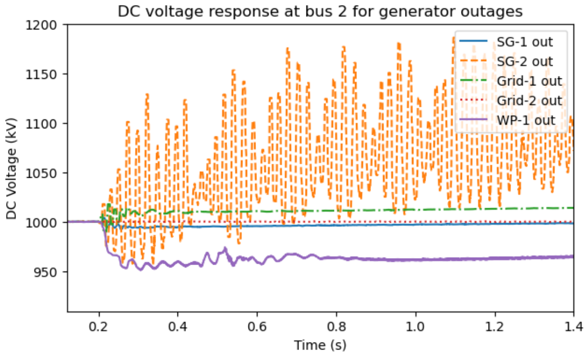

Figure 5.7: DC voltage response at bus 2 for generator outages

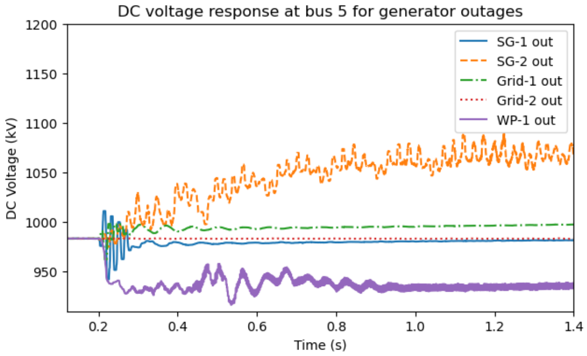

Figure 5.8: DC voltage response at bus 5 for generator outages

It is observed in the figure that losing grid-2 has no influence on the DC voltage. The small demand of grid-2 is fully covered by the wind power plant WP-2, which is connected to the same bus as grid-2. Therefore this outage does not influence the performance of the DC system. Even losing grid-1 has no large influence on the DC voltage. When the equivalent grid is disconnected from the system, the generators in the grid stop delivering power. This stabilizes the system in a short period of time. The outage of the wind power plant WP-1 results in a small dip in the DC voltage of $50\,kV$ at both measurement locations. In addition, the voltage starts oscillating slowly. After 0.8 s the voltage already stops oscillating and stabilizes.

In Fig. 5.11 the frequency responses for different generator outages are shown at bus 7. The largest deviation in frequency is caused by the loss of grid-1. In the figure, an increase in the frequency of $1.3\,Hz$ is observed when losing grid-1. This is an unacceptable response. As grid-1 is consuming $10\,GW$ of power, it can be understood why this results in the largest deviation. After the large peak, the system restores to 50 Hz again. This is also observed at buses 6 and 8. This is shown in Fig. 5.9 and Fig. 5.10.

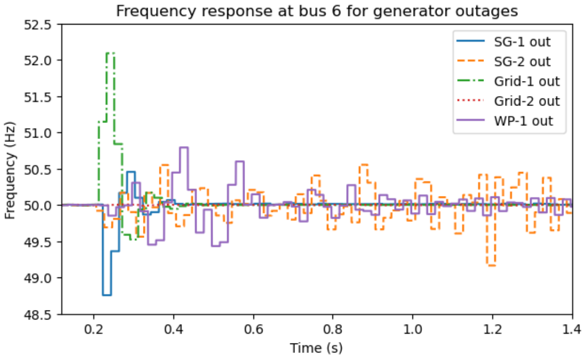

Figure 5.9: Frequency response at bus 6 for generator outages

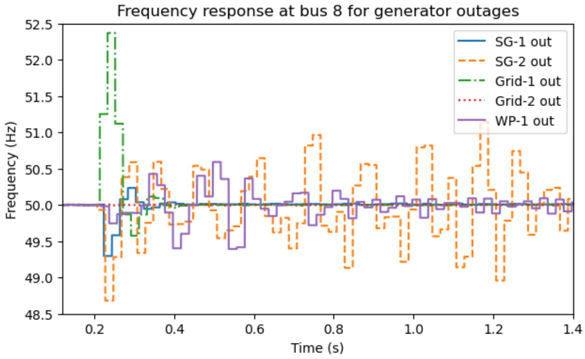

Figure 5.10: Frequency response at bus 8 for generator outages

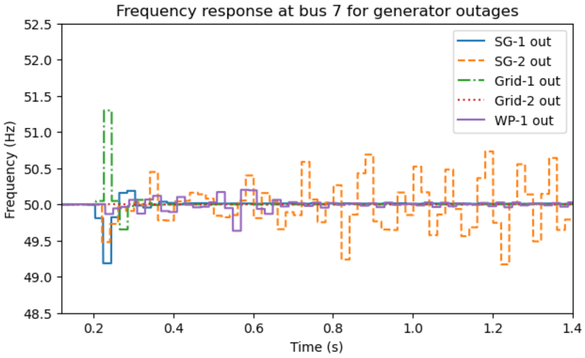

Figure 5.11: Frequency response at bus 7 for generator outages

The outage of SG-1 and SG-2 show to have different influences on the response of the frequency. Where the outage of SG-1 results in a dip of $0.8\,Hz$, a somewhat comparable response is expected in the case of losing SG-2. This is not the case. The frequency response shows oscillations with a maximal amplitude above 0.5 Hz. The oscillations can be explained by looking at the active power flows through the system.

The active power flow in the DC system can be seen in Fig. 5.12 for line 1-2 and for line 1-5 in Fig. 5.13. In the figure, it is observed that the outage of SG-2 causes heavy oscillations at line 1-2, which results in oscillations at line 1-5. While in both lines, the outage of SG-1 barely affects the power flow. The oscillations in lines 1-2 and 1-5, result in an unstable active power flow in the AC lines 6-7 and 7-8. This is shown in Fig. 5.14 and Fig. 5.15. This explains why for the outage of SG-2 oscillations in the frequency at all three buses are observed.

Losing WP-1 has caused similar oscillations as losing SG-2. With a maximal amplitude of 0.5 Hz, the frequency of the system operates unstable. This means that the oscillations in the DC voltage as shown in Fig. 5.7 and Fig. 5.7, make the frequency of the AC side unstable. The oscillations are also observed in the active power flow in the DC lines in Fig. 5.12 and Fig. 5.13. However, in this case, the DC voltage control is able to stabilize after 0.8 s. Even though, the oscillations result in an oscillatory response of the frequency at buses 6 and 8.

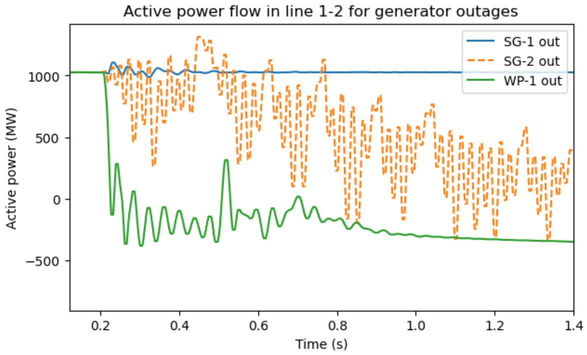

Figure 5.12: Active power flow in line 1-2 for generator outages

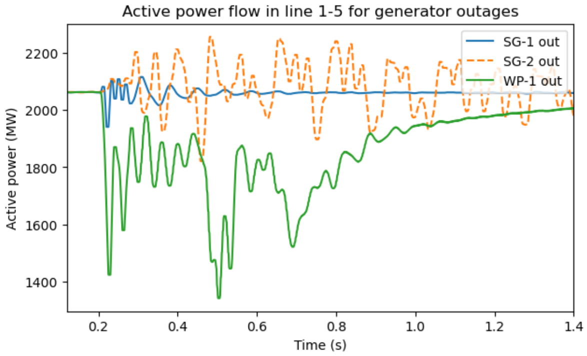

Figure 5.13: Active power flow in line 1-5 for generator outages

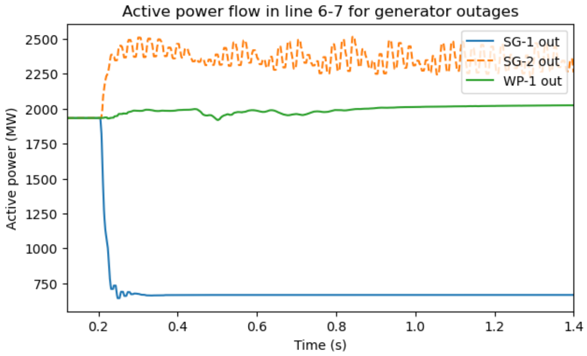

Figure 5.14: Active power flow in line 6-7 for generator outages

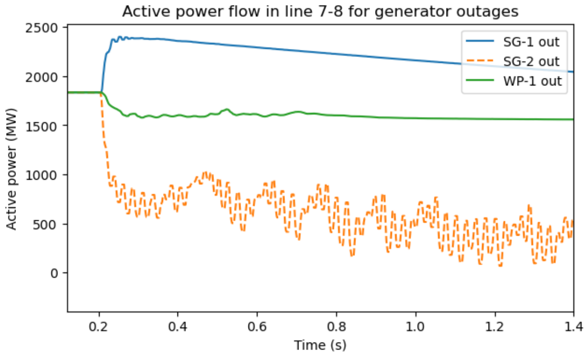

Figure 5.15: Active power flow in line 7-8 for generator outages

In table 5.4 the calculated performance metrics are shown for the different generator outages. When analyzing the calculated values of RoCoF, the calculated values show that only the value for the outage of grid-2 the RoCoF stays 1 Hz/s. The highest value of RoCoF is calculated for the outage of Grid-1, which is due to the high spike. Tthe value for the outage of SG-2 comes quite close to the value of losing grid-1. However no large peak in frequency is observed for the outage of SG-2, but heavy oscillations. In this case, the RoCoF shows the difference between a minimal and a maximal value, resulting in a large RoCoF. As the large oscillations are not acceptable, it is good that a high value is found. In practice, high values of RoCoF will cause parts of the system to disconnect. For the other, slightly lower oscillations. The values of RoCoF are also relatively high, which matches the observed responses.

Almost all calculated values of RoCoV are quite small, except for the outage of SG-2. With a RoCoV of 745.4 kV/s at bus 2 this is clearly the highest value in this table. Which matches with the analyses of Fig. 5.7. However, when comparing this value to the converter outage value of MMC-5 shown in table 5.3, these values are around the same. Comparing the instability caused by losing SG-2 to the dip in voltage caused by the outage of MMC-5, the instability is more alarming. A higher value of RoCoV would be more suited to this situation. The other calculated values of RoCoV are in line with the analyses of this section.

Disturbance	**RoCoF bus 6 (Hz/s)**	**RoCoF bus 8 (Hz/s)**	**RoCoV bus 2 (kV/s)**	**RoCoV bus 5 (kV/s)**
Grid-1 outage	4.179	4.738	87.08	127.8
Grid-2 outage	0.01816	0.02068	2.248	1.724
SG-1 outage	2.519	1.432	32.88	150.1
SG-2 outage	1.580	4.274	745.4	386.6
WP-1 outage	1.641	1.339	177.6	264.1

Table 5.4: Overview of calculated performance metrics for generator outages

Line Outages

The figures 5.16 and 5.17 show the responses of the DC voltage at buses 2 and 5 for different line outages. The influence of the line outages on the DC voltage performance at bus 2 is quite small. The two lines (lines 1-2 and 2-3) connected to bus 2 are not extensively loaded, so in the case of losing one, the other can take the extra amount of power. The outage of line 2-3 resulted in a larger dip than the outage of line 1-2 as this line was carrying more power before the outage. The power flowing through line 1-5 can easily be taken on by these two lines after the outage of line 1-5. Therefore, only small changes in the DC voltage are seen at bus 2.

As the impact of the outages of lines 1-2 and 2-3 are re-accommodated at bus 2, no influence is observed in the response of the DC voltage at bus 5. The most influential outage at bus 5 is the loss of line 1-5. This outage results in a drop of almost 200 kV. As this is the only line connecting the DC side of MMC-5 to the DC system, no power will flow through bus 5 anymore. Thus resulting in a drop in DC voltage.

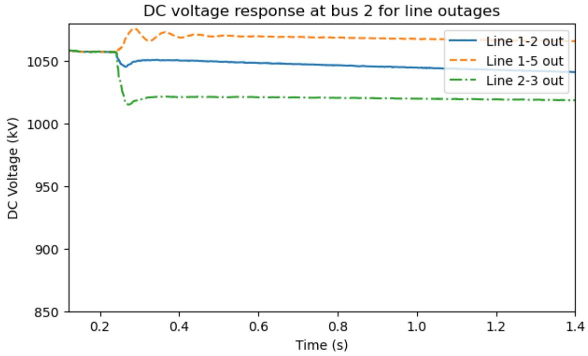

Figure 5.16: DC voltage response at bus 2 for line outages

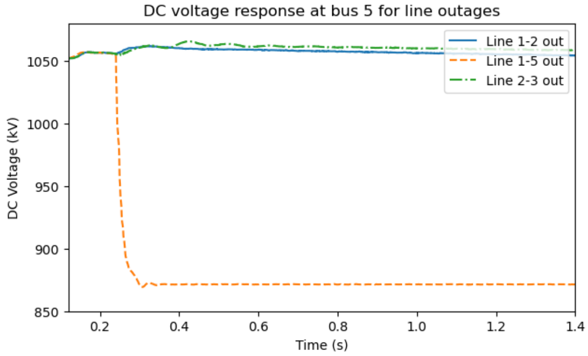

Figure 5.17: DC voltage response at bus 5 for line outages

In Fig. 5.18 and Fig. 5.19 the frequency responses at buses 6 and 8 for different line outages are shown. Both figures are quite similar. The frequency at bus 6 is most influenced by the outage of line 1-5. This outage results in a deviation of 0.25 Hz. The other responses show almost no influence of the line outage, just as is observed the DC voltage response at bus 5. At bus 8, the outage of line 2-3 is the most influential on the frequency response. Again a dip of 0.25 Hz is observed.

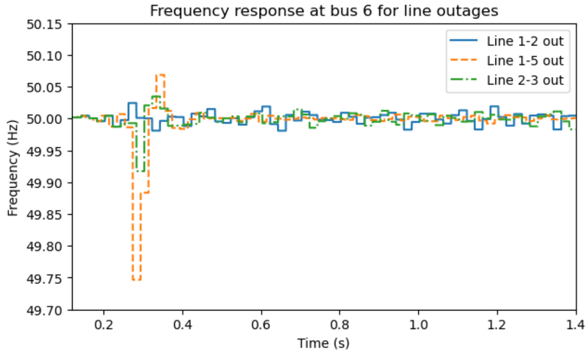

Figure 5.18: Frequency response at bus 6 for line outages

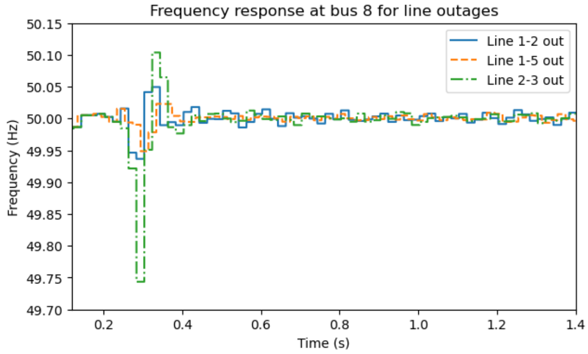

Figure 5.19: Frequency response at bus 8 for line outages

Table 5.5 shows the calculated performance metrics for the different line outages. The calculated RoCoV values show that only the value of losing line 1-55 results in a high value at bus 5. All other values are relatively low. This corresponds well with the responses seen in Fig. 5.16 and Fig. 5.17. Also, the calculated values of RoCoF are in line with the observed responses of Fig. 5.18 and Fig. 5.19. The highest values are calculated for line 2-3 at bus 8 and line 1-5 at bus 6. Both values are almost the same, which corresponds to the almost identical frequency responses for these cases. None of the RoCoF values come close to 1 Hz/s, which means that the frequency responds within limits for all three line outages.

Disturbance	RoCoF bus 6 (Hz/s)	RoCoF bus 8 (Hz/s)	RoCoV bus 2 (kV/s)	RoCoV bus 5 (kV/s)
Line 1-2 outage	0.01154	0.1785	42.06	27.66
Line 1-5 outage	0.5087	0.1467	61.80	767.6
Line 2-3 outage	0.1811	0.5138	151.6	41.40

Table 5.5: Overview of calculated performance metrics for line outages

5.3.2. Short Circuits

DC Side Short Circuit

In Fig. 5.20 and Fig. 5.21 the DC voltage responses for different short circuits in the DC system are shown. At both buses, the most influential disturbance is a line-to-line short circuit at the converter. A short circuit at the converter makes the voltage drop to zero within a few ms. Also line-to-line faults further away result in a steep descent to almost 0. In both figures, it is observed that the further away the short circuit, the less influence is observed. For a line-to-ground fault at the converter, the voltage of the damaged line will drop to zero, thus resulting in half the drop of a line-to-line short circuit. In this situation, half of the transport capacity can still be used via the other (non-damaged)polarity. Just as with the line-to-line short circuits, the further away the short circuit, the less influence is observed.

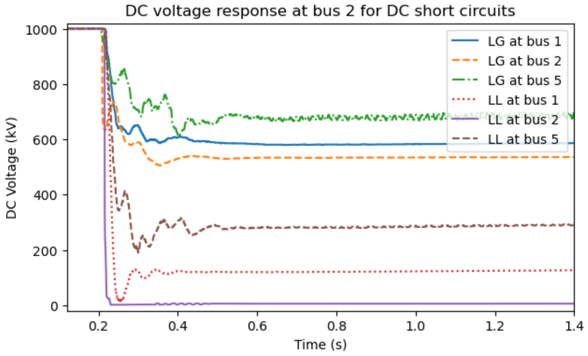

Figure 5.20: DC voltage response at bus 2 for DC side short circuits

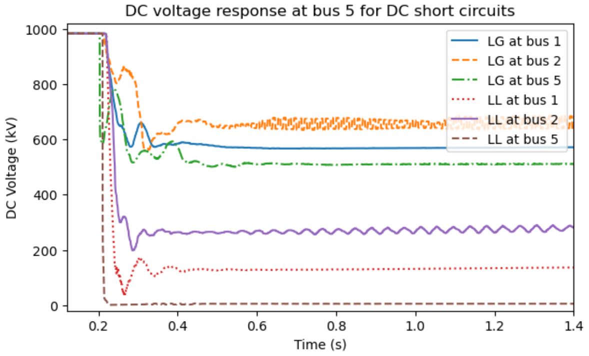

Figure 5.21: DC voltage response at bus 5 for DC side short circuits

The influence of DC side short circuits on the power flow in the DC system is shown in Fig. 5.22 and Fig. 5.23. The figures show that the DC side short circuits also cause steep slopes in the active power flow. The short circuit closest to the lines is shown to have the highest impact and the further away the less impact. This supports what is observed in the response of the DC voltage.

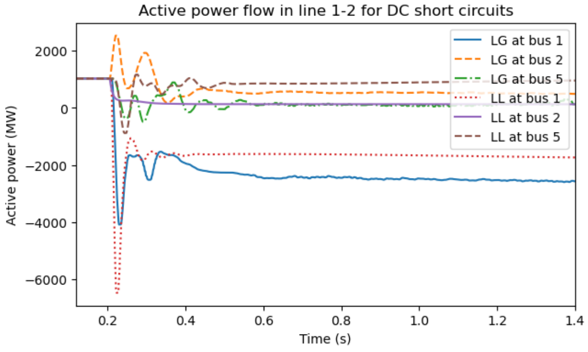

Figure 5.22: Active power flow in DC line 1-2 for DC side short circuits

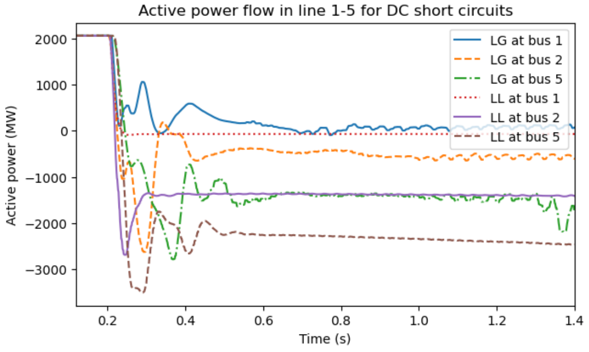

Figure 5.23: Active power flow in DC line 1-5 for DC side short circuits

From the analysis of the response of the DC voltage for DC side short circuit faults, it becomes clear that the DC system can not handle line-to-line or line-to-ground faults. For both cases, large dips in the voltage are observed. After the disturbance, the DC voltage shows no signs of recovery. This is because the DC system does not have enough capacity to restore the voltage from DC side faults. During the fault, IGBTs are blocked for self-protection, which creates a high over-current through the diodes. This can seriously damage the diodes [22].

Also, the AC side suffers from short circuit faults in the DC system. In Fig. 5.24 and Fig. 5.25, the frequency response for the different DC side short circuit events is shown. The graphs show that the line-to-line faults at bus 2 and bus 5 cause a frequency drop of $1.5\,Hz$. Also, a line-to-line fault further away, at bus 1, results in a deviation in frequency of $0.8\,Hz$. Also, a line-to-ground fault the DC side will result in relatively large frequency changes. All the line-to-ground faults result in a frequency deviation of around $0.5\,Hz$.

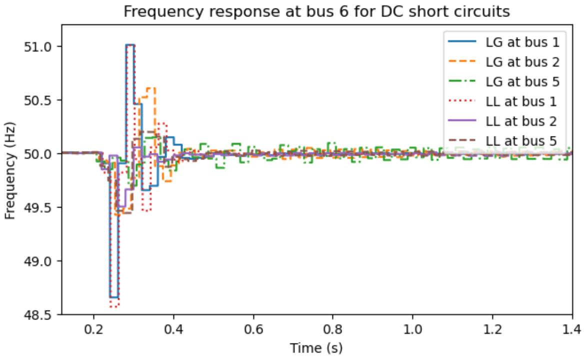

Figure 5.24: Frequency response at bus 6 for DC side short circuits

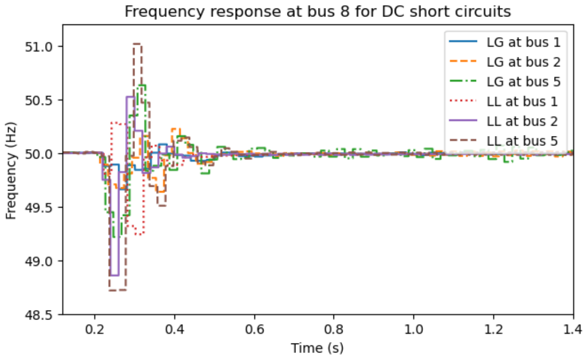

Figure 5.25: Frequency response at bus 8 for DC side short circuits

The calculated performance metrics for DC side short circuits are presented in table 5.6. In the table, high values of RoCoV are observed for every short circuit. This aligns with the drastic responses observed in Fig. 5.20 and Fig. 5.21. The resulting values show that the values for a line-to-ground fault stay below 2000 kV/s. This aligns with that only one line is affected in this case. For line-to-line short circuits, all calculated RoCoVs are above 2000 kV/s. When further looking at the calculated RoCoVs, the values also show that the further away the fault, the less impact.

Also the calculated values of RoCoF are relatively high. The calculated values are in line with the large oscillations seen in the frequency response during the disturbance. The calculated values show which short circuit results in the highest deviation in frequency and align with the analyses made.

Disturbance	**RoCoF bus 6 (Hz/s)**	**RoCoF bus 8 (Hz/s)**	**RoCoV bus 2 (kV/s)**	**RoCoV bus 5 (kV/s)**
LG at bus 1	2.682	0.6651	1681	1667
LG at bus 2	1.295	0.7126	1885	1393
LG at bus 5	0.7921	1.886	1067	1931
LL at bus 1	2.844	1.490	3522	3426
LL at bus 2	2.271	0.9949	3978	2902
LL at bus 5	1.151	2.441	3314	3912

Table 5.6: Overview of calculated performance metrics for DC side short circuits

AC Side Short Circuit

Fig. 5.26 and Fig. 5.27 show the DC voltage responses at bus 2 and bus 5 for different AC side short circuits. Both types of AC side faults (line-to-line and 3-line-to-ground) result in an increase in DC voltage. In addition, the responses for the different scenarios follow the same pattern. Only slight differences in the heights of the peaks are observed. The most influential short circuit is the 3-lines-to-ground short circuit at the other side of the converter. In both graphs, this results in the highest overshoot. The lowest overshoot is observed for a line-to-line fault further away. In contrast to the DC side short circuits, the DC voltage is slowly recovering to its pre-disturbance level after the disturbance. The fastest settling time is achieved with a line-to-line fault.

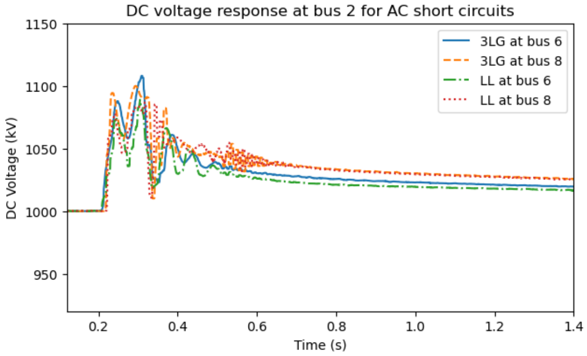

Figure 5.26: DC voltage response at bus 2 for AC side short circuits

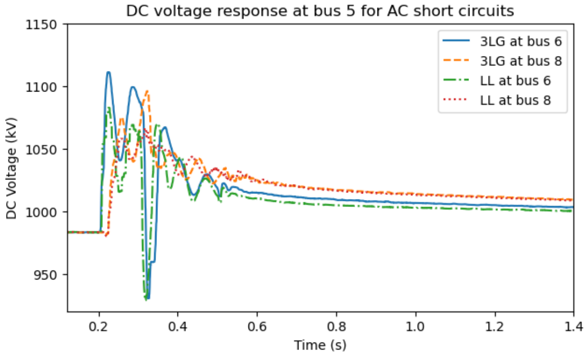

Figure 5.27: DC voltage response at bus 5 for AC side short circuits

In Fig. 5.28 and Fig. 5.29 the frequency responses are shown for different AC side short circuits. When comparing the figures, two similar graphs are observed. For both converters, the frequency responses to line-to-line and 3-line-to-ground faults at the converter show to follow the same pattern. In the case of a 3-line-to-ground short circuit at the converter, a dip of almost 5 Hz is seen. Also for a line-to-line fault, the frequency response shows a maximal deviation of 3 Hz. However, the frequency restores quickly as soon as the fault is isolated.

As the location of the fault is very close to the measurement location of the frequency, this has resulted in this large deviation from the base frequency. This analysis is supported by the fact that if the fault happens at the other converter, almost no disruption in the frequency is seen. When the fault is located at another station, only a small oscillation is observed in the frequency response during the disturbance. Therefore, for this part, also the frequency at bus 7 will be analyzed.

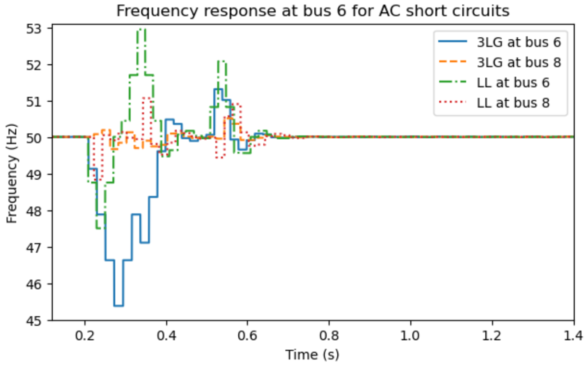

Figure 5.28: Frequency response at bus 6 for AC side short circuits

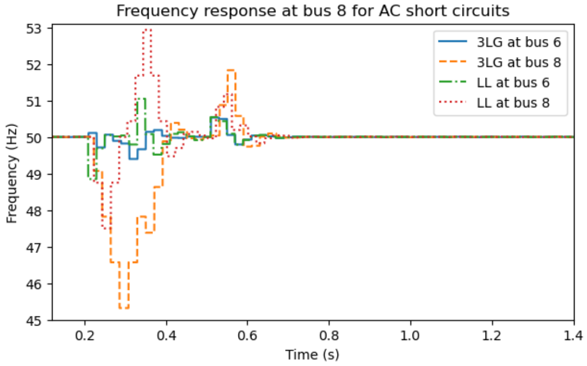

Figure 5.29: Frequency response at bus 8 for AC side short circuits

In Fig. 5.30 the frequency response at bus 7 is shown for different AC side short circuits. In this plot, no large disruptions as in Fig. 5.28 and Fig. 5.29 are seen. This shows that these were numerical errors of the frequency measurement unit. The most influential short circuit is a line-to-line at bus 6, followed by a line-to-line at bus 8. The impact of a line-to-line is higher at bus 6 as there is more power coming from there. Also for 3-lines-to-ground short circuits, the impact of a short circuit at bus 6 is slightly more than at bus 8.

The calculated performance metrics for AC side short circuits are presented in table 5.7. The calculated RoCoV values show that a 3-lines-to-ground short circuit close to the other side of the converter has the most impact on the DC voltage. If the disturbance is further away, the impact is somewhat lower, which is captured by the RoCoV. The values of RoCoF show some really high values at buses 6 and 8, but they clearly align with the frequency responses shown in Fig. 5.28 and Fig. 5.29. In a real power system, RoCoF values of 5 and 9 Hz/s are unrealistic. Therefore the frequency was analyzed at bus 7.

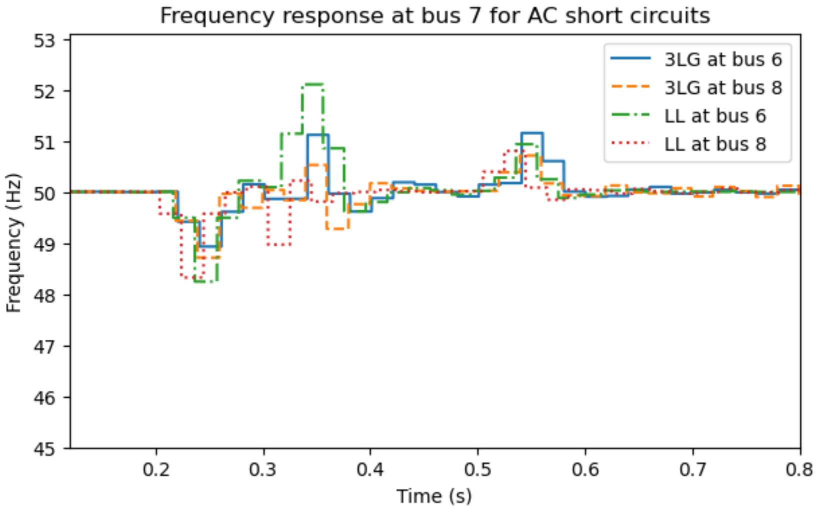

Figure 5.30: Frequency response at bus 7 for AC side short circuit faults

The calculated RoCoF values are all above 2 Hz/s, which means that they are alarming. The frequency response still shows too high deviations, which is unacceptable for the system. In contrast to the DC voltage, the most influential AC side short circuit is the line-to-line fault. For both buses, the disturbance is significantly higher compared to 3-lines-to-ground short circuits.

Disturbance	**RoCoF bus 6 (Hz/s)**	**RoCoF bus 7 (Hz/s)**	**RoCoF bus 8 (Hz/s)**	**RoCoV bus 2 (kV/s)**	**RoCoV bus 5 (Hz/s)**
3LG at bus 6	9.253	2.768	1.207	355.3	504.8
3LG at bus 8	1.022	2.300	9.353	462.5	491.1
LL at bus 6	5.883	4.201	2.311	288.8	432.5
LL at bus 8	2.354	3.480	5.865	412.8	411.9

Table 5.7: Overview of calculated performance metrics for AC side short circuits

5.3.3. Comparison of Performance Metrics

This section has discussed the dynamic response of the test system when faced with different disturbances. For almost all types of outages, both AC and DC sides show adequate responses. However, when faced with generator outages the system can become unstable. For the stability of the DC voltage, losing SG-2 has the highest impact compared to all other outages. When losing this generator, MMC-2 is no longer capable of keeping the DC voltage stable. However, by switching DC voltage control to MMC-5, this problem could easily be solved.

The test system has more problems with responding to short circuit faults. The line-to-line faults on the DC side have a huge impact on the response of the system. When the fault occurs close to the converter, the DC voltage drops to 0 within a few ms. For line-to-ground faults on the DC side, the voltage of the damaged line drops to 0. In this case, it is still possible to transport power via the other pole. Even short circuit faults on the AC side, result in the highest voltage deviation on the DC side.

The analyses of this section show that these conclusions can also be seen in the calculated metrics. Only in the case of losing SG-2, a too-low RoCoV value is calculated. In this case, the value is around some of the other acceptable outage responses such as the outage of line 1-5. When comparing the response of the outage of SG-2 with the outage of line 1-5, these are not close to each other. The instability caused by the outage of Gen-A2 is more alarming and should result in a significantly higher value.

In Fig. 5.31. Fig. 5.32 the confusion matrices have been plotted for RoCoV and RoCoF. The threshold for an unacceptable RoCoV is taken to 600 kV/s, this means that if the deviation of the DC voltage is larger than

150 kV the system is unacceptable. This value is taken as a reference as no regulation on the DC system voltage currently exists. For RoCoF the threshold is set to 1 Hz/s, equal to the strictest grid codes. The time series of the voltage responses and frequency responses are classified as acceptable or unacceptable responses as well.

The values of RoCoV are in line with what is observed in the time series responses for most of the cases. Only in a few cases, a too-low value was calculated. This is the case when an oscillating response is observed. The value of RoCoV can be used to distinguish between 3 categories: line-to-line DC faults (RoCoV > 2000 kV/s), line-to-ground DC faults (2000 kV/s > RoCoV > 1000 kV/s), and other faults (RoCoV < 1000 kV/s). In addition, the RocoV values show the distance to the fault. For example, in the case of a line-to-line short-circuit. The RoCoV is lower if the short-circuit is further away from the measurement location.

The confusion matrix of RoCoF shows more mistakes. The RoCoF gives a false acceptable response in the case of an oscillating response, just as the RoCoV. An unfair unacceptable RoCoF value is found in the case of a short-circuit close to the measurement. In this case, a large frequency dip is measured and translated into an unrealistic RoCoF. These values of RocoF can not be used to make a fair comparison of the impact.

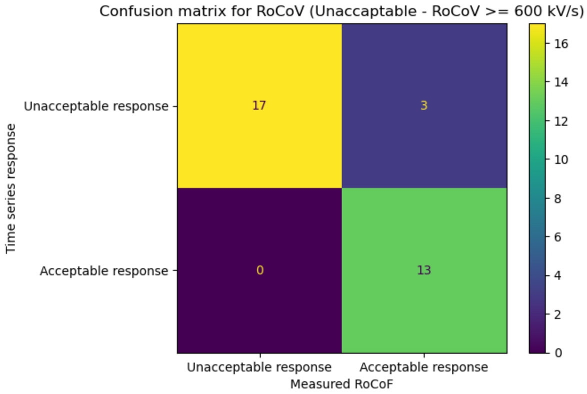

Figure 5.31: Confusion matrix RoCoV

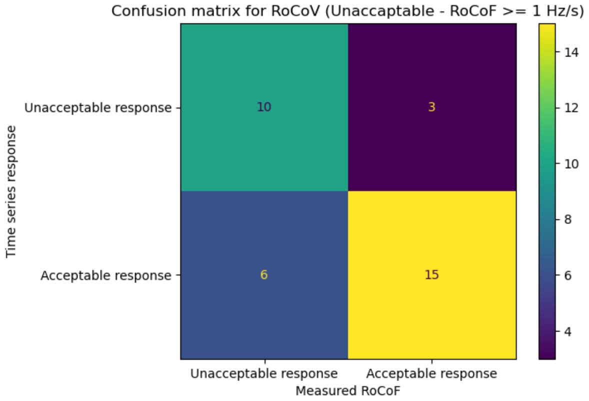

Figure 5.32: Confusion matrix RoCoF

5.4. Parametric Sensitivity Analyses

From the previous section, it has become clear that in most cases the system responds quite well to different events on both sides of the system. Only in the case of a short circuit, the system gets unstable. In this section, only the worst case AC side and DC side disturbance be shown. On the DC side, this is a line-to-line fault at the converter, and on the AC side, a 3-lines-to-ground disturbance will be examined. In section 5.2, the different settings of the control parameters are discussed. The parameters that will be altered are on the d-axis, and thus only have an impact on the DC voltage. Therefore, the frequency response will not be discussed in this section.

The numerical results of the simulations have shown that the influence of the control parameters is the same at the different buses in the DC system. In this section, the responses at bus 5 are chosen to present instead of showing the responses at buses 2 and 5 as done in the previous section.

5.4.1. Outer Loop Control Parameter Settings

Proportional Gain Parameters

In the control loop for determining the d-axis reference current, 2 proportional gains are used. The first one is the K_p for DC voltage control (K_p DC). The other one is the K_p for active power control (K_p PWR). The proportional gain of the active power control loop is actually set to 0, and instead, dead-band control is used. For the analyses of the proportional gain parameter of the active power control loop, the dead-band is turned off.

Fig. 5.33 shows the DC voltage responses to an AC side short circuit at Cb-A5 for different values of K_p in the DC voltage control loop. In the figure, it is seen that for lower values of K_p, the voltages settle quicker compared to the base value. Especially, for K_p equal to 5, the voltage settles the quickest. However, the initial overshoot for K_p equal to 5 is higher than the base. The overshoot is around $20\,kV$ higher. For values higher than the base value of K_p, the settling time is slower, and some unstable oscillations are observed after the disturbance. During the disturbance, all DC voltage responses seem to follow the same pattern. The responses in the graph show that a higher K_p results in a higher overshoot and a slower settling time. Lower values result in a faster settling time but still have a higher overshoot compared to the base.

The calculated values of RoCoV for different K_p DC for a 3-lines-to-ground event are shown in table 5.8. All values of RoCoV are higher than the base scenario. This is because the overshoots of all signals are higher than the base, which is captured by the RoCoV. The results show that the highest overshoot is for the lower proportional gains. The change in settling time is not captured by the RoCoV.

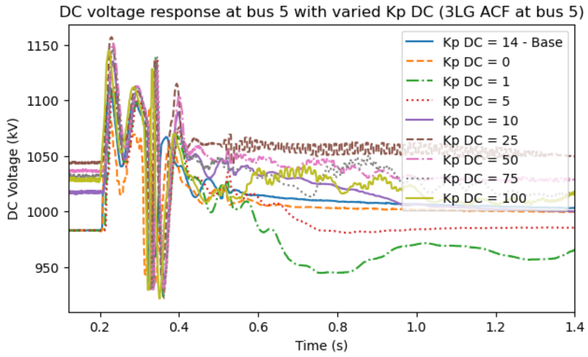

Figure 5.33: DC voltage response at bus 5 for AC side short circuit with varied K_p DC

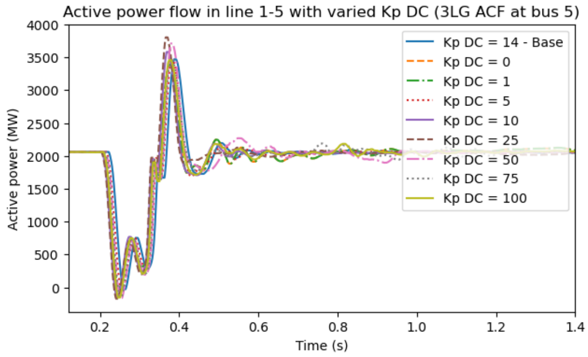

Figure 5.34: Active power flow in line 1-5 for AC side short circuit with varied K_p DC

The response of the active power flow in line 1-5 is shown for different values of K_p DC after an AC side short circuit in Fig. 5.34. This figure shows, as expected, that the proportional gain of the DC voltage control has no influence on the active power flow. Fig. 5.35 and Fig. 5.36 show that the proportional gain parameter of the DC voltage control loop has no influence on the DC voltage response and on the response of the active power flow for a line-to-line fault at the DC side. The DC voltage still immediately drops to zero showing that the controller can not respond to this quick change in DC voltage. Also in the active power flow, no significant deviations are observed.

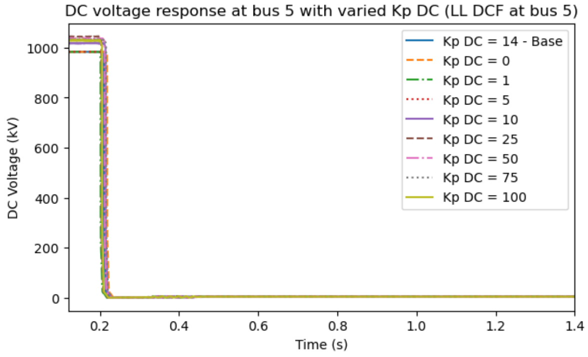

Figure 5.35: DC voltage response at bus 5 for DC side short circuit with varied K_p DC

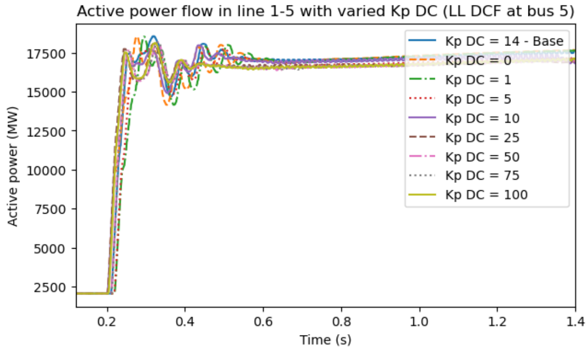

Figure 5.36: Active power flow in line 1-5 for DC side short circuit with varied K_p DC

The calculated values of RoCoV for a line-to-line DC short circuit are presented in table 5.8. The values show that in some cases the DC voltage has another pre-disturbance level, thus resulting in some deviation from the base value. The resulting values show that a higher proportional gain results in a higher value of RoCoV for a line-to-line DC short circuit.

Control Scenario	RoCoV bus 5 (kV/s) 3LG at bus 6	RoCoV bus 5 (kV/s) LL at bus 5
Base (Kp DC = 14)	504.8	3934
Kp DC = 0	710.1	3933
Kp DC = 1	1027	3934
Kp DC = 5	1015	3934
Kp DC = 10	884.7	4123
Kp DC = 25	773.1	4203
Kp DC = 50	729.2	4193
Kp DC = 75	864.8	4193
Kp DC = 100	849.4	4180

Table 5.8: Calculated performance metrics for varied K_p DC

The influence of the proportional gain in the active power loop on the DC voltage response for an AC side short circuit is presented in Fig. 5.37. From the graph, it becomes clear that turning on the proportional gain of the power loop has no positive influence on the response of the DC voltage for an AC side short circuit. The lowest overshoot and quickest settling time is achieved with the base scenario. For the other lines, an unstable response is seen with either a high overshoot or heavy oscillations. This is also observed in the response of the active power flow in line 1-5. In Fig. **??**, all active power responses show heavy oscillations.

The instability explains the motivation behind choosing the dead-band control in the active power loop. The DC voltage control is responsible for maintaining the DC network stable, ensuring that the incoming power flow is equal to the outgoing flow of power. The other converters will try to keep their power reference and the final converter (MMC-2, controlling the DC voltage) ensures that the total incoming power equals the outgoing. In both loops, PI controllers are used to determine the reference current. A PI controller will keep on trying to keep its output to the set reference. As it is impossible to perfectly match the reference, the use of a PI controller results in a small oscillation around the reference. The dead-band control does not operate in a set margin around the setpoint, giving the DC voltage control room to stabilize the system. When the proportional gain of the active power is turned on, the controllers will try to achieve the same thing, resulting in unstable oscillations.

The calculated values of RoCoV shown in table 5.9 align with the analyses. All cases have a significantly higher value of RoCoV compared to the base scenario. In the calculated values for a 3LG at bus 6, it is observed that ah higher proportional gains lead to a higher value of RoCoV.

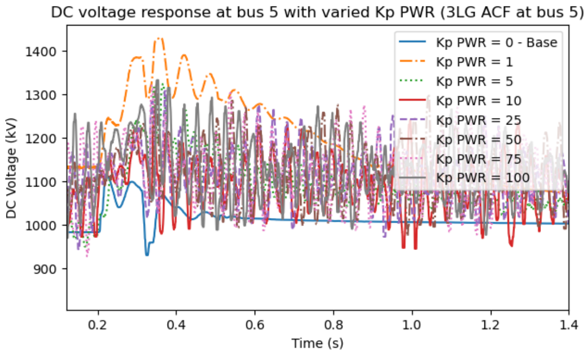

Figure 5.37: DC voltage response at bus 5 for AC side short circuit with varied K_p PWR

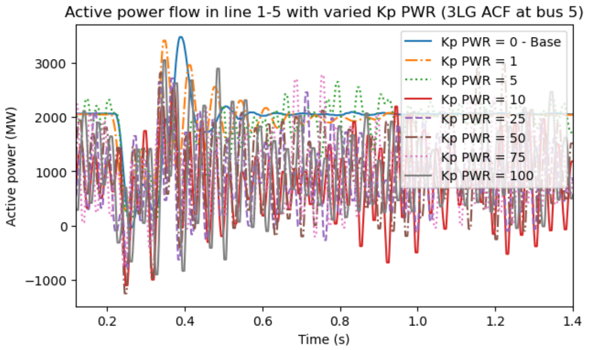

Figure 5.38: Active power flow in line 1-5 for AC side short circuit with varied K_p PWR

Again, the DC voltage response for a DC side line-to-line short circuit is not influenced by the different settings of K_p PWR. As can be seen in Fig. 5.39. The DC voltage before the disturbance is again already unstable, which results in slight differences in the calculated RoCoV values of table 5.9. For higher values of K_p PWR, the DC voltage is already unstable before the disturbance, this results in significantly higher values of RoCoV.

It is also shown that a higher K_p PWR leads to a higher RoCoV. The proportional gain of the active power loop has also no influence on the active power flow in line 1-5 after a line-to-line short circuit. All responses follow the exact same pattern. This is shown in Fig. 5.40.

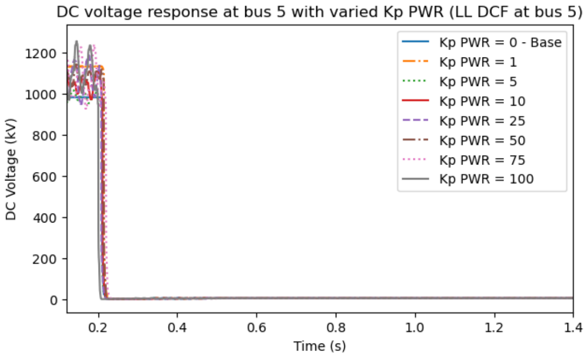

Figure 5.39: DC voltage response at bus 5 for DC side short circuit with varied K_p PWR

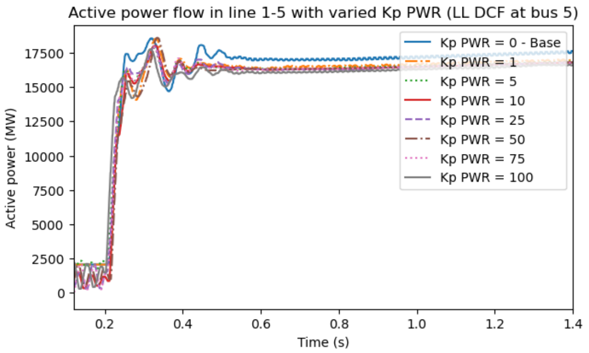

Figure 5.40: Active power flow in line 1-5 for DC side short circuit with varied K_p PWR

Control Scenario	RoCoV bus 5 (kV/s) 3LG at bus 6	RoCoV bus 5 (kV/s) LL at bus 5
Base (Kp PWR = 0)	504.8	3934
Kp PWR = 1	1298	4596
Kp PWR = 5	1726	4602
Kp PWR = 10	1995	4199
Kp PWR = 25	2108	4929
Kp PWR = 50	2110	5454
Kp PWR = 75	2478	5144
Kp PWR = 100	2575	5661

Table 5.9: Calculated performance metrics for varied K_p PWR

Integral Gain Parameters

Again 2 integral gains are available in both PI controllers. The first one is the K_i for DC voltage control (K_i DC). The other one is the K_i for active power control (K_i PWR). In Fig. 5.41, the influence of the integral gain of the DC voltage control loop for an AC side short circuit is shown. During the disturbance, all responses follow the same pattern. Only the responses of the DC voltage for K_i DC equal to 1 s and 0.02 s have a higher initial peak, but also a higher DC voltage before the disturbance. The integral gain of the DC voltage controller has no influence on the active power response, as shown in Fig. 5.42.

The main influence on the integral gain is the settling time of the response. This corresponds to the role of the integral gain in PI control. The integral gain responds slower compared to the proportional gain and integrates the error over time to eliminate the residual error. Therefore, the results show that the integral gain mainly has an impact on the settling time of the response, and almost none on the overshoot.

This is not reflected in the calculated values of RoCoV. The values of RoCoV in table 5.10 show higher values for all cases. This is caused by the extra low drop in voltage around 0.4 s. In the base case, the minimal value of response is around 950 kV. In the figure, minimal values below 900 kV are observed for different integral gains. Thus instead of capturing the difference between the pre-disturbance value and the initial overshoot, the maximal difference that is captured is between the minimal point and the value 0.25 s later. This makes the information gained from the RoCoV useless.

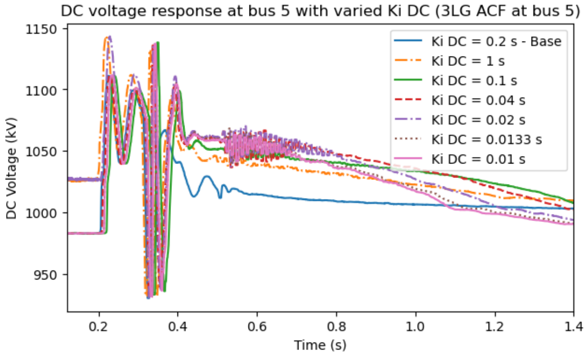

Figure 5.41: DC voltage response at bus 5 for AC side short circuit with varied K_i DC

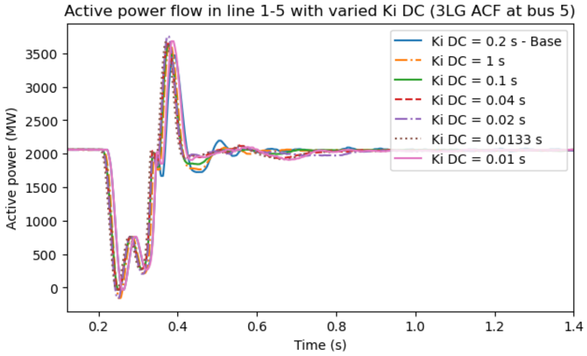

Figure 5.42: Active power flow in line 1-5 for AC side short circuit with varied K_i DC

In Fig. 5.44, the active power through line 1-5 is shown after a DC side short circuit. In the figure, it is shown that the integral gain of the DC voltage controller has no influence on the response of the active power flow. Also the response of the DC voltage can not be adjusted by using different values for K_i DC. This is shown in Fig. 5.43. This results in almost equal values of RoCoV. These are presented in table 5.10.

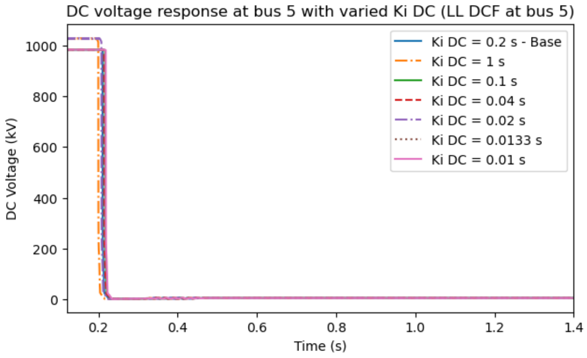

Figure 5.43: DC voltage response at bus 5 for DC side short circuit with varied K_i DC

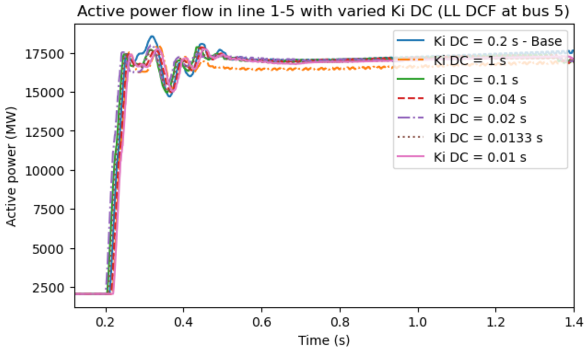

Figure 5.44: Active power flow in line 1-5 for DC side short circuit with varied K_i DC

For a DC side short circuit, changing the value of either one of the integral gains shows no effect on the response of the DC voltage. In all figures, the DC voltage follows the same pattern. This is presented in Fig. 5.43 and Fig. 5.47. Also, the calculated values of RoCoV for a DC side line-to-line short circuit show no large deviations from the base value. The calculated values for a varied K_i DC are shown in table 5.10 and for K_i PWR in table 5.11.

Control Scenario	**RoCoV bus 5 (kV/s) 3LG at bus 6**	**RoCoV bus 5 (kV/s) LL at bus 5**
Base (Ki DC = 0.2 s)	504.8	3934
Ki DC = 1 s	808.9	4150
Ki DC = 0.1 s	1022	4150
Ki DC = 0.04 s	988.9	3934
Ki DC = 0.02 s	817.7	3934
Ki DC = 0.0133 s	973.7	4149
Ki DC = 0.01 s	996.9	3935

Table 5.10: Calculated performance metrics for varied K_i DC

The influence of the integral gain of the power controller on the response of the DC voltage for an AC side short circuit is shown in Fig. 5.45. In the graph, it can be seen that almost all lines follow the same pattern during the disturbance. Just as when adjusting K_i DC, the integral gain has almost no influence on the during-disturbance phase. After the initial overshoot, most of the DC voltage responses start oscillating slightly. Only the base scenario and K_i equal to 0.0133 s do not oscillate. The settling time of K_i equal to 0.0133 s is even quicker than the base scenario. All values of K_i below the base value show heavy oscillations. This is most likely caused by a too-quick influence of the integral gain in responding to faults.

This is also observed in the response of the active power flow in line 1-5, as presented in Fig. 5.46. During the disturbance, all responses follow the same pattern. also here, the influence of the integral gain is in the settling time. A faster response of the integral gain, results in more oscillations in the active power.

Just as with the RoCoV values for different values of K_i DC, the values of RoCoV are all higher than the base when the integral gain of the active power loop is adjusted. This can be seen in table 5.11. Again the extra low dip in DC voltage is captured, instead of the difference between the pre-disturbance value and the initial overshoot.

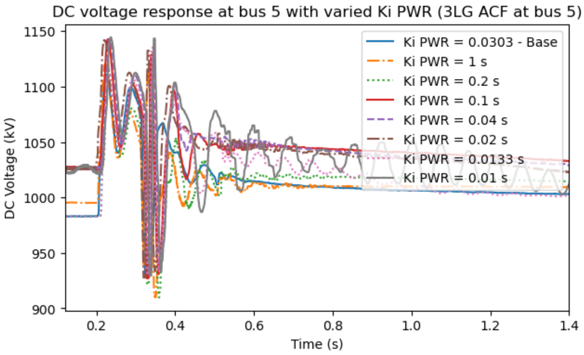

Figure 5.45: DC voltage response at bus 5 for AC side short circuit with varied K_i PWR

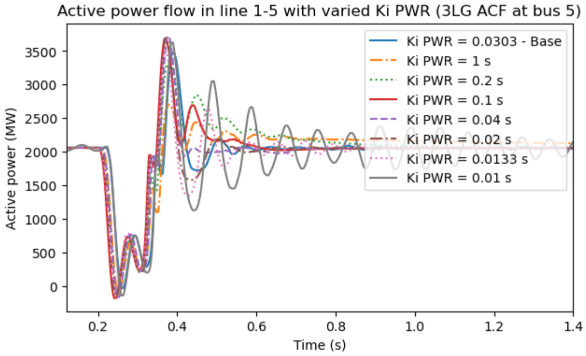

Figure 5.46: Active power flow in line 1-5 for AC side short circuit with varied K_i PWR

In Fig. 5.47 and Fig. 5.48, the DC voltage and active power flow after a DC side short circuit are shown. In both figures, just as with different values of K_i DC, the responses all follow the same pattern for different integral gains in the active power control loop. This results in no significant changes in the calculated RoCoV values. These are presented in table 5.11.

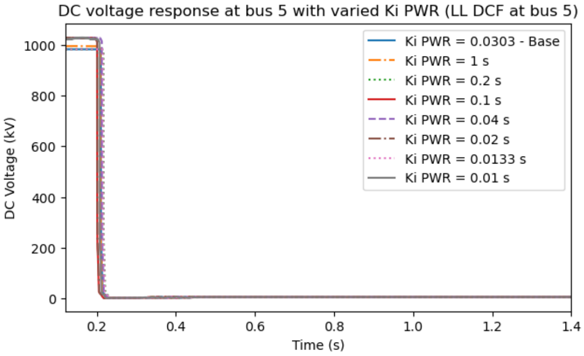

Figure 5.47: DC voltage response at bus 5 for DC side short circuit with varied K_i PWR

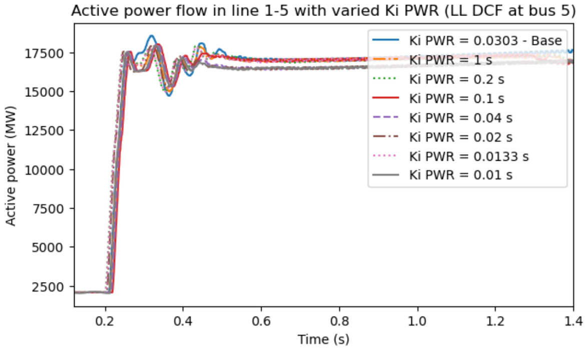

Figure 5.48: Active power flow in line 1-5 for DC side short circuit with varied K_i PWR

Control Scenario	**RoCoV bus 5 (kV/s) 3LG at bus 6**	**RoCoV bus 5 (kV/s) LL at bus 5**
Base (Ki PWR = 0.0303 s)	504.8	3934
Ki PWR = 1 s	810.5	3985
Ki PWR = 0.2 s	860.1	3934
Ki PWR = 0.1 s	790.7	4148
Ki PWR = 0.04 s	801.6	4153
Ki PWR = 0.02 s	776.7	4151
Ki PWR = 0.0133 s	1016	3935
Ki PWR = 0.01 s	835.9	4161

Table 5.11: Calculated performance metrics for varied K_i PWR

Dead-band Control Parameters

In the dead-band control, 2 parameters can be varied. The first one is the slope of the dead-band. This is the parameter that is multiplied by the difference between the reference signal and the actual signal. The second parameter is the width of the dead-band. This is the range in which the controller does not operate. This is set as a percentage of the reference.

Fig. 5.49 shows the DC voltage responses for different values of the gain of the slope in the case of an AC side short circuit. The first thing that can be concluded is that a low slope results in a higher overshoot and slower settling time. All values of the gain of the slope below the base show a response with higher overshoot and slower settling time. In this case, the dead-band controller does not respond strongly enough to the disturbance, creating a high overshoot in DC voltage. When analyzing the responses for a steeper slope, the responses of the DC voltage at bus 5 show an oscillating response for high gains. This is also observed in the response of the active power flow in line 1-5 (Fig. 5.50). The 2 highest dead-band slopes result in an oscillating active power. The other responses of the active power flow are quite similar.

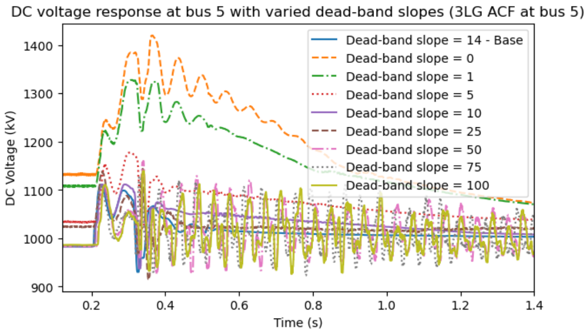

Figure 5.49: DC voltage response at bus 5 for AC side short circuit with varied dead-band slope gain

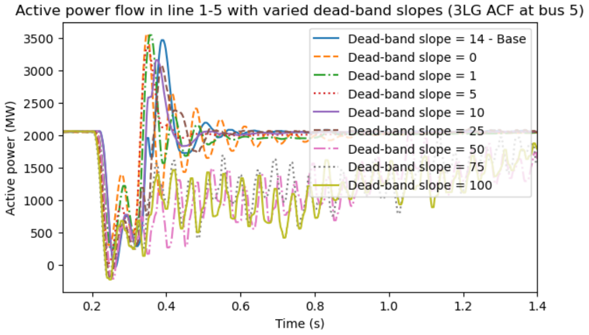

Figure 5.50: Active power flow in line 1-5 for AC side short circuit with varied dead-band slope gain

This conclusion is not fully supported by the calculated metrics of RoCoV, shown in table 5.12. Almost all of the calculated values of RoCoV are significantly above the base value. Only the values for a gain of 5 and 10, the RoCoVs come close to the base setting. For both signals, the overshoot and settling time are slightly worse compared to the base. Especially, for a gain of 10 a value almost equal to the base is expected. The calculated value of RoCoV is different than expected as the RoCoV is calculated as a moving window with a width of 0.25 s. This means that the first end of the window is equal to a value after the initial overshoot. The difference between the overshoot and the value 0.25 s is less compared to the difference between the start value and the overshoot value. This results in a lower value of RoCoV. The higher gains result in significantly higher RoCoVs, which are in line with the observed oscillations for these scenarios. Even though the RoCoV does not capture the difference in overshoot, the visualization of the calculated RoCoVs shown in Fig. 5.51, shows that a higher or lower than the base results in the increase of RoCoV.

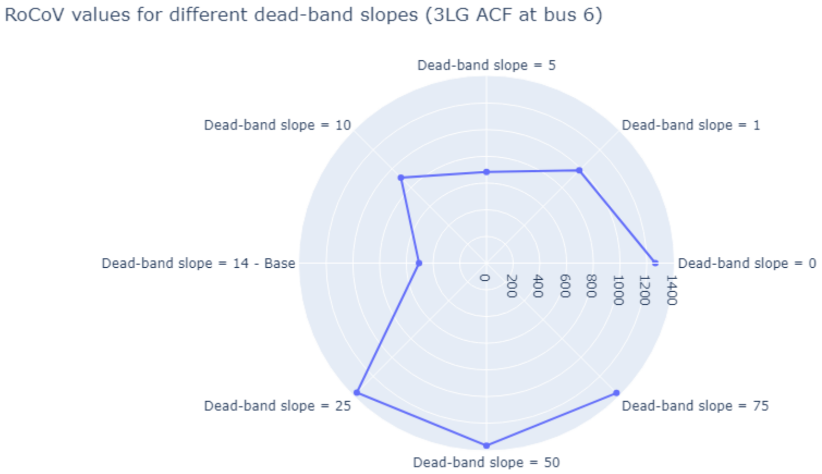

Figure 5.51: RoCoV values for different dead-band slopes

When looking at the DC voltage and active power flow responses after a DC side short circuit, the responses in Fig. 5.52 and Fig. 5.53 show that the dead-band slope has no influence on the dynamic responses. This is also observed in the calculated values of RoCoV presented in table 5.12. The only differences are due to the different pre-disturbance values.

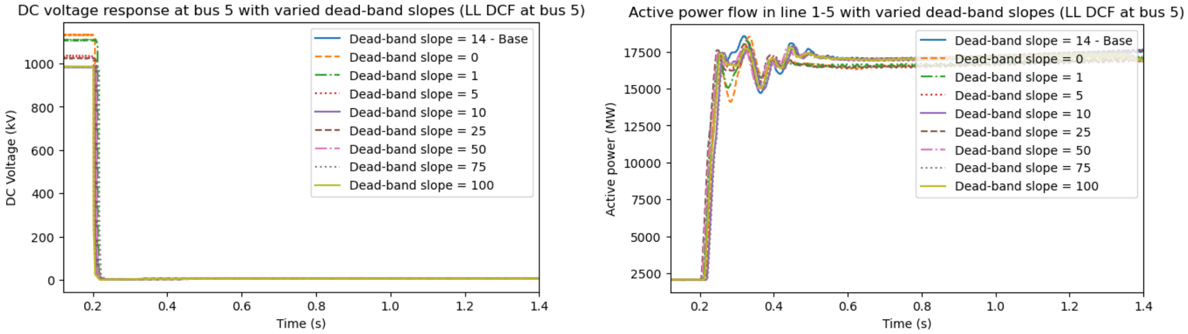

Figure 5.52: DC voltage response at bus 5 for DC side short circuit with varied deadband slope gain

Figure 5.53: Active power flow in line 1-5 for DC side short circuit with varied deadband slope gain

Control Scenario	**RoCoV bus 5 (kV/s)** **3LG at bus 6**	**RoCoV bus 5 (kV/s)** **LL at bus 5**
Base (K Deadband = 14)	504.8	3934
K Deadband = 0	1263.8	4502
K Deadband = 1	982.4	4181
K Deadband = 5	627.9	3933
K Deadband = 10	682.2	4151
K Deadband = 25	905.9	3933
K Deadband = 50	1372	4151
K Deadband = 75	1367	3935
K Deadband = 100	1376	3947

Table 5.12: Calculated performance metrics for varied dead-band slope gains

A wide variety of responses is observed in Fig. 5.54. It may not come as a surprise that a wider width of the dead-band leads to a worse response in DC voltage. A width of 50 % leads to the highest overshoot compared to the other responses. When compared to the base of 5 %, each broader width of the dead-band leads to a higher overshoot and slower settling time. A smaller bandwidth of 0 % and 1 % show responses close to the base scenario during the disturbance. However, both responses show oscillations after the disturbance.

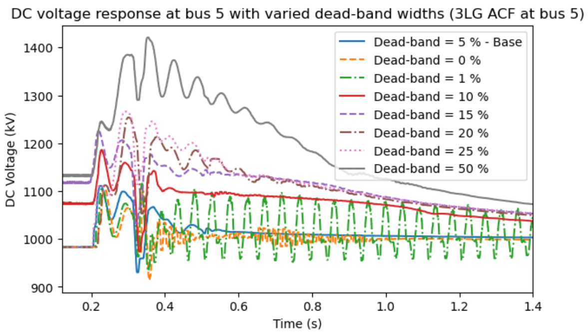

Figure 5.54: DC voltage response at bus 5 for AC side short circuit with varied width of dead-band

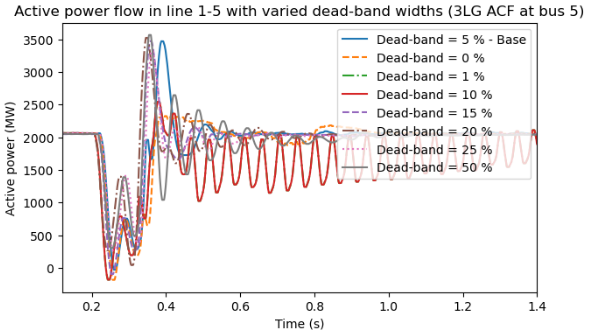

Figure 5.55: Active power flow in line 1-5 for AC side short circuit with varied width of dead-band

The oscillation observed for a dead-band width close of 0 % and 1 % show again the motivation of implementing dead-band control in the active power control loop. With small values of the dead-band width, the controller basically becomes equal to the proportional gain of the PI controller in the active power control loop. Therefore, a too-low width of the dead-band is not desirable. The base scenario with a width of 5 % shows the best responses and is the right setting of the dead-band as a larger window leads to a worse response.

The same observations can be made from the response of the active power flow through line 1-5, as is shown in Fig. 5.55. Although, more oscillations are observed. For the higher bandwidths oscillations are observed after the disturbance. In this figure, the bandwidth of 5 % also shows to be the ideal value, as this does not result in oscillations.

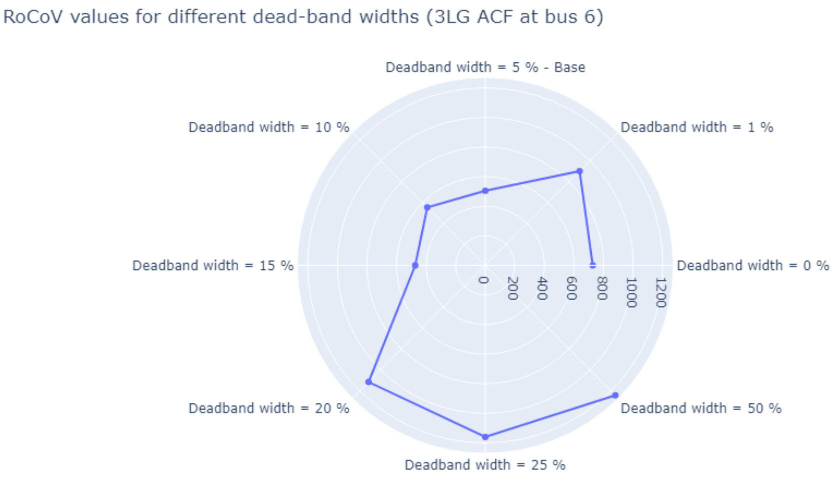

Figure 5.56: RoCoV values for different dead-band widths

The calculated values of RoCoF for different dead-band widths are presented in table 5.13 and visualized in Fig. 5.56. The results show that the ideal setting of the dead-band width would be 15 %. For values above and below this width, the RoCoVs increase. This is not entirely in line with the results in Fig. 5.54. For a width of 15 % a slower setting time is achieved, but a smaller overshoot. This means that the RoCoV does not tell the full story. An additional metric should be used to compare the settling times.

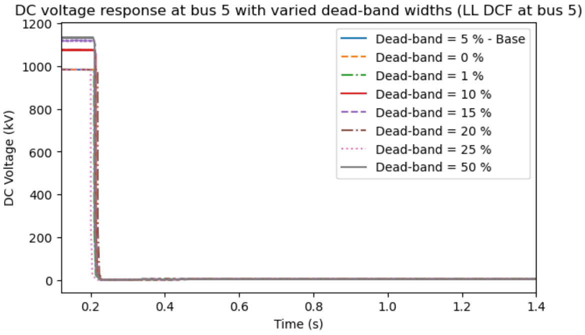

Figure 5.57: DC voltage response at bus 5 for DC side short circuit with varied width of dead-band

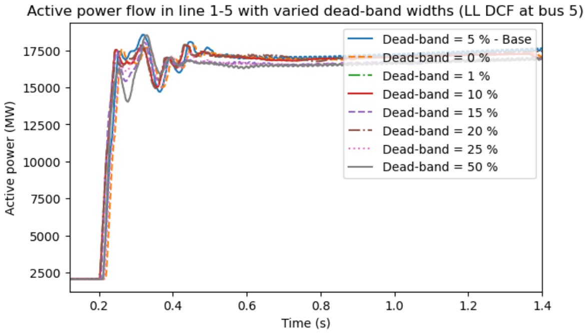

Figure 5.58: Active power flow in line 1-5 for DC side short circuit with varied width of dead-band

Again, it must be concluded that adjusting the width of the dead-band has no influence on the dynamic response of the DC voltage and the active power flow. This is shown in Fig. 5.57 and Fig. 5.58. The recorded values of RoCoV align with the time series and only show the difference between the pre-disturbance values. The calculated values of RoCoV can be found in table 5.13.

Control Scenario	**RoCoV bus 5 (kV/s) 3LG at bus 6**	**RoCoV bus 5 (kV/s) LL at bus 5**
Base (width = 5 %)	504.8	3934
Width = 0 %	1225	3937
Width = 1 %	901.3	3940
Width = 10 %	553.9	4151
Width = 15 %	473.4	4350
Width = 20 %	1114	4350
Width = 25 %	1159	4537
Width = 50 %	1242	4597

Table 5.13: Calculated performance metrics for varied dead-band widths

5.4.2. Comparison of Performance Metrics

In the previous sections, the influence of different control parameters is analyzed. From the analyses, it has become clear that adjusting the parameters can positively impact the system's DC voltage response to an AC side short circuit. Improving the response of the DC voltage for a line-to-line short circuit at the DC side is not possible by adjusting the control parameters.

The control parameters do have an influence on the DC voltage response after an AC side 3-lines-to-ground short circuit. The proportional gains of the controllers mainly influence the overshoot of the DC voltage and have a small influence on the settling time. This corresponds to the role of the proportional gain in PI control, to respond quickly to faults. However, it must be noted that this statement is not valid for adjusting the proportional gain of the active power controller. Adjusting this parameter causes the system to behave unstablely. The integral gain responds slower and integrates the error over time to eliminate the residual error. The results show that the integral gain mainly has an impact on the settling time of the response, and almost none on the overshoot.

The parameters of the deadband controller have an impact on both the overshoot and the settling time of the system. A low deadband gain results in a high overshoot, whereas a higher gain results in a lower overshoot. However, a too-high value of the gain results in an unstable DC voltage. The reverse is valid for different values of the deadband width. A smaller width will lead to a lower overshoot, but a too-small deadband width will lead to an unstable DC voltage. A larger deadband width will result in a higher overshoot and slower settling time.

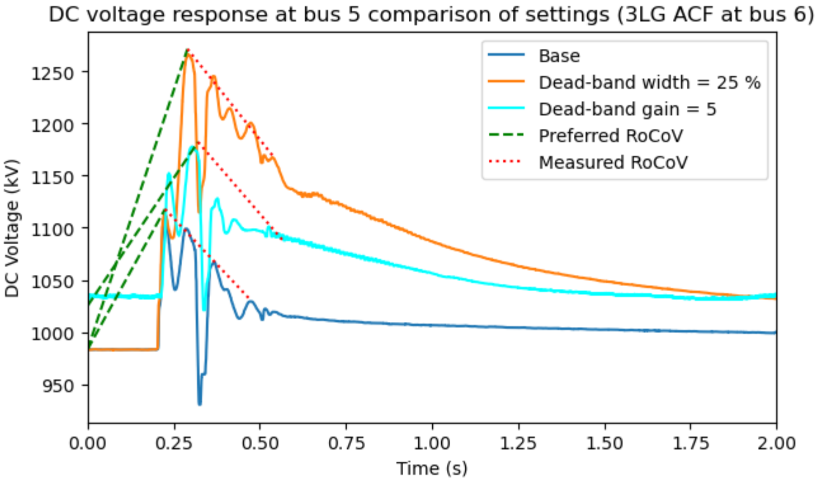

Figure 5.59: Illustrive example of calculated values of RoCoV for different control settings compared to preferred RoCoV

The influence of the control parameters is not well captured by the calculated values of RoCoV in all cases. The root of this problem is shown in Fig. 5.59. The calculated RoCoV values represent the rate of change after the disturbance hit the system. For comparing the impact of different disturbances this works well, but when adjusting control parameters this can result in too high values of RoCoV. For comparing the impact of control parameters the difference between the initial overshoot and the pre-disturbance value is needed for a fair comparison between the control settings. This could be improved by shortening the window time, to enable the RoCoV to capture the difference between the initial overshoot and pre-disturbance value. With a window of 0.25 s, it is not always possible to capture the initial overshoot as this is located before 0.25 s.

5.5. Concluding Remarks

In this chapter, the numerical results of the different case studies are discussed. The simulations that are performed show that both the DC and AC sides of the system are able to restore from different component outages. However, the system has the most problems when faced with short circuits close to the converter. A short circuit on the DC side results in an immediate collapse of the DC voltage. For an AC side short circuit at the converter, a large dip in the frequency is observed. In addition, the influence of the reference setpoints on the response of the system is analyzed. The analyses clearly show that adjusting the reference input of the control has almost no effect on the response of the system.

The proposed performance metrics are well able to capture most of the dynamic responses of the system for different types of disturbances. However, in the case of an oscillating response during the disturbance, the metrics are not able to classify this type of impact on the system. For oscillating responses, a low value of the rate of change is measured, indicating an acceptable response.

In order to analyze the sensitivity of the outer control loop parameters on the response of the system, their influence on the response to the worst-case AC side and DC side disturbance is examined. Adjusting the outer loop parameter has shown to have no influence on the response of the DC voltage to a DC side short circuit. Within a few milliseconds, the DC voltage has dropped to zero. The controller can not respond to this quick change, so adjusting the parameters of the controller has no influence on the response of the DC voltage.

On the other side, adjusting the control parameters can have a positive impact on the response of the DC voltage for an AC side short circuit at the converter. By changing the control parameters, it was possible to improve the response of the DC voltage. The main influence of the control parameters is in the settling time. However, the proportional gain of the DC voltage control shows to have some influence on the initial overshoot of the voltage. In addition, the analyses of the parametric sensitivity have shown the advantage of using dead-band control instead of the proportional gain of the active power control. Using this proportional gain instead of dead-band control results in heavy oscillations. Using the proposed performance metric RoCoV, it is not always possible to capture the difference in initial overshoot, as the initial overshoot might occur before the end of the first window. A shorter window period could be used to overcome this.

6

Conclusion and Recommendations

This chapter will provide the answers to the research questions formulated in chapter 1. But before presenting the answers, a recap of the problem definition will be given in the next section. This chapter will be concluded with recommendations for future work.

6.1. Recap of Problem Definition

This master thesis presents the work done in evaluating the impact of disturbances on the active power imbalance of MTDC-linked offshore-onshore systems. Power systems form the backbone of our modern society. Large disruptions or breakdowns of the energy supply may cause serious economic and social damage. Designing resilient and reliable power grids is of great importance to prevent large breakdowns or blackouts.

Historically, conventional risk assessment methods have been employed to evaluate the performance of the power system. This methodology ensures the system can effectively address recognized hazards and vulnerabilities, with a particular emphasis on assessing the reliability of power systems. In this type of study, the origin of disturbances and the dynamic response of the system are not taken into account. Resiliency studies do focus on this. Assessing the resilience of power systems typically involves three stages. Firstly, the disturbance progression phase is examined, during which the resilience level deviates from its pre-disturbance level. Secondly, assuming effective primary control measures are implemented, a new steady-state operating condition is reached, which differs from the pre-disturbance condition. Finally, the system enters the restorative phase, where the recovery process starts.

The development of future hybrid AC/DC power systems poses new challenges to the stability of power systems. In future hybrid power systems, fewer reserves will be available. Also, the control capabilities of converters are limited compared to the current power system. This makes the initial response of the system following a disturbance more critical. Therefore in this thesis, the focus is on evaluating the dynamic performance of the power system during a disturbance.

In literature, it is found that the impact of different disturbances is analyzed by comparing the time series of the responses of different parameters in the power system. In this thesis, the impact of disturbances on the dynamic response of the system is evaluated by quantifying the dynamic response of the system. A performance metric is chosen for both the AC and DC sides of the system to qualitatively assess the impact on the system's dynamic performance during a disturbance.

The widely employed RoCoF (Rate of Change of Frequency) serves as the chosen performance metric to evaluate the active power-frequency response from the perspective of the AC side. Additionally, a novel metric, the Rate of Change of Voltage (RoCoV), is introduced to capture the response of the DC voltage. The DC voltage is indicative of power imbalances in a DC system. Conventional voltage stability indices are inadequate for capturing the dynamic behavior of the DC voltage. RoCoV is recommended in state-of-the-art protection schemes as a valuable indicator for detecting faults in DC systems. Therefore, in this thesis, RoCoV is employed as the metric to quantify the dynamic response of the DC voltage in an MTDC system.

6.2. Answers to Research Questions

The overall goal of the thesis is to develop a framework for the assessment and enhancement of hybrid AC/DC systems. This framework aims at evaluating the impact of disturbances on hybrid AC/DC networks. In order to achieve this goal, 4 research questions are defined in section 1.3. This section will provide the answers to each research question. The analyses of the last chapter support the answers given to the questions.

1. **What insights on the impact of different disturbances on the dynamic response can be gained from the adopted performance metrics after a disturbance in an MTDC-linked offshore-onshore system?**

   The dynamic performance of a hybrid AC/DC system is quantified by adopting a performance metric for each side of the system. For the AC side, the commonly used RoCoF is used to describe the stability of the frequency. On the DC side, the DC voltage describes the synchronous operation of the system. Therefore, the use of RoCoV is proposed as a metric to quantify the dynamic response of the DC voltage. The calculated performance metrics after different outages and short circuits are shown and discussed in section 5.3.
   The confusion matrix for the determined RoCoF values is shown in Fig. 5.32. The value of RoCoF is misleading in the case of oscillations. In the case of an oscillating response, the value of RoCoF might show that the system behaves within limitations. The values of RoCoF are also useless in the case of a short circuit close to the measurement of the frequency. In this case, the frequency-time series show numerical errors that result in unrealistic RoCoF values.
   The RoCoF metric can be used to provide insight into the propagation of a fault through the AC system and show the distance to the fault. The further away, the lower RoCoF will be observed. As can be seen in Fig. 5.24, the further away the disturbance in the DC system, the lower RoCoF is measured. The RoCoF does not provide insight in the type of disturbance.
   This insight can be gained from the RoCoV values. The highest RoCoV values are observed for DC line-to-line short circuits. The values in this category are above 1000 kV/s The second group of RoCoV values is for line-to-ground short circuits on the DC side. In this group the RoCoV values are between 500 and 1000 kV/s. The third group consists of RoCoVs below 500 kV/s. In this category, all the remaining disturbances can be found.
   The RoCoV values also provide insight into the distance to the disturbance. In each of the outage and short circuit scenarios, the RoCoV decreases if the disturbance is further away. However, also the RoCoV is misleading in the case of oscillations. In this case, a lower value of RoCoV is calculated.

2. **How effective are the adopted performance metrics in capturing the sensitivity of the parameters in the outer control loop of an MMC converter on the dynamic response in an MTDC-linked offshore-onshore system?**

   In section 5.4, the sensitivity of the outer loop control parameters on the responses of the DC voltage and frequency is analyzed for an AC side and DC side short circuit at the converter. The time series of the frequency responses show that in most cases, the control parameters have no influence on the response. This is also observed in the calculated values of RoCoF. For the different case studies, the value of RoCoF stays close to the base.
   When adjusting control parameters, the RoCoF can only provide insight in cases when the DC voltage becomes unstable. When adjusting K_p PWR, the DC voltage becomes unstable. When this happens, the measured RoCoF is somewhat higher than the base value. In the other cases, no useful information can be obtained from the RoCoF. In the case of a DC line-to-line short circuit, the control parameters show to have no influence on the response of the DC voltage.
   On the other hand, adjusting the control parameter does have an impact on the DC voltage response in case of an AC side short circuit. The proportional gain of the DC voltage mainly influences the initial overshoot of the system. Whereas, the proportional gain of the active power loop makes the system unstable. This impact is well captured by the increase in RoCoV. A higher K_p PWR results in a higher RoCoV. The same type of results is expected in the case of increasing K_p DC. This is not captured by RoCoV, as the difference after the overshoot is captured in the current format.
   The integral gains show to have no influence on the initial overshoot, but more on the settling time. This can not be captured by the metrics, as this is no their purpose to quantify.
   The deadband parameters have an influence on both overshoot and settling time. With a window of 0.25 s it is not able to quantify this influence. In order to overcome this problem, a smaller window period can be used to capture the difference in initial overshoot.

Therefore, with a shorter window period, the RoCoV can be used to provide insight into the difference in overshoot when adjusting the control parameters. The RoCoF can only be used to capture an unstable DC voltage, which results in a deviating RoCoF from the base.

6.3. Recommendations for Future Work

The concluding section of this thesis will propose potential enhancements and additions derived from the knowledge and expertise acquired throughout the project. These suggestions aim to further improve the research based on the insights gained.

For this thesis, 2 metrics were used to capture the stability of the network. Each metric describes the stability of a part of the system. RoCoF is used for the stability of the AC side and RoCoV for the stability of the DC side. However, an interesting world lies between both sides where AC and DC meet: the converter. In the converter, AC voltages are transformed into DC and vice versa. An additional metric investigating the response inside the converter and capturing the transfer from a disturbance from one side to another would be interesting to add to the current performance metrics.

This research is focused on the effect of different disturbances on the dynamic responses of hybrid AC/DC systems. In this research, the focus has been on disturbances in the physical part of the system. The influence of attacks on the digital systems of the network has not been studied. It would be interesting to analyze the effect of cyber-attacks on the network and to see if the proposed metrics can also capture the effect of different cyber-attacks.

The BM1 model consisted of 2 equivalent grids of which one was relatively small and both grids were modelled as one load. It would be interesting to extend the model with more detailed AC systems connected to the DC system at different locations and see the influence on the frequency response through the system and not only on the point of coupling.

In order to isolate faulted sections, the fault is isolated by the use of circuit breakers. In the BM1 model, no protection algorithm was installed, which ensures the operation of the breakers. In a new, related research project it would be interesting to model a protection algorithm and see the influence on the dynamic response. It could also be interesting to adjust the parameters to see the sensitivity of the response.

The control system of the converters of the BM1 model is based on a vector-oriented control system for all converters. In the model, all 5 converters can easily cooperate to keep the DC system stable. In future networks, converters may use different control strategies from different vendors. Also in this situation, the cooperation of converters is important. It would be interesting to see the effect of different control strategies and different vendors on the response of the system.

Bibliography

[1] P. Gasser, P. Lustenberger, M. Cinelli, *et al.*, "A review on resilience assessment of energy systems," *Sustainable and Resilient Infrastructure*, vol. 6, pp. 273–299, 5 2021, ISSN: 23789697. DOI: 10.1080/23789689.2019.1610600.

[2] C. W. G. S. C4.47. "Defining power system resilience." (30 September 2019), [Online]. Available: https://www.cigre.org/article/GB/news/the_latest_news/defining-power-system-resilience. (accessed: 23-11-2022).

[3] H. Sabouhi, A. Doroudi, M. Fotuhi-Firuzabad, and M. Bashiri, "Electrical power system resilience assessment: A comprehensive approach," *IEEE Systems Journal*, vol. 14, pp. 2643–2652, 2 Jun. 2020, ISSN: 19379234. DOI: 10.1109/JSYST.2019.2934421.

[4] B. Ti, G. Li, M. Zhou, and J. Wang, "Resilience assessment and improvement for cyber-physical power systems under typhoon disasters," *IEEE Transactions on Smart Grid*, vol. 13, pp. 783–794, 1 Jan. 2022, ISSN: 19493061. DOI: 10.1109/TSG.2021.3114512.

[5] D. E. Alexander, "Resilience and disaster risk reduction: An etymological journey," *Natural hazards and earth system sciences*, vol. 13, no. 11, pp. 2707–2716, 2013.

[6] A. A. Bajwa, H. Mokhlis, S. Mekhilef, and M. Mubin, *Enhancing power system resilience leveraging microgrids: A review*, May 2019. DOI: 10.1063/1.5066264.

[7] F. M. Gonzalez-Longatt, M. N. Acosta, H. R. Chamorro, and J. L. Rueda Torres, "Power converters dominated power systems," in *Modelling and Simulation of Power Electronic Converter Dominated Power Systems in PowerFactory*, Springer, 2021, pp. 1–35.

[8] X. jiao tong da xue, *Power System Resiliency*. 2019, ISBN: 9781728117225.

[9] G. Chaqués-Herraiz, S. Bernal-Perez, J. Martinez-Turegano, S. Añó-Villalba, R. Peña, and R. Blasco-Gimenez, "Dc voltage control in off-shore wind farms with distributed diode rectifier units," in *43rd Annual Conference of the IEEE Industrial Electronics Society (IECON), Beijing, China*, IEEE, pp. 202–207, 2017.

[10] M. Muniappan, *A comprehensive review of dc fault protection methods in hvdc transmission systems*, Dec. 2021. DOI: 10.1186/s41601-020-00173-9.

[11] H. R. Wickramasinghe and G. Konstantinou, "Interoperability of modular vsc topologies in multi-converter multiterminal dc systems," *Electric Power Systems Research*, vol. 196, p. 107 225, 2021.

[12] M. H. Rahman, L. Xu, and L. Yao, "Protection of large partitioned mtdc networks using dc-dc converters and circuit breakers," *Protection and Control of Modern Power Systems*, vol. 1, pp. 1–9, 2016.

[13] S. Debnath, J. Qin, B. Bahrani, M. Saeedifard, and P. Barbosa, "Operation, control, and applications of the modular multilevel converter: A review," *IEEE transactions on power electronics*, vol. 30, no. 1, pp. 37–53, 2015.

[14] F. B. Ajaei and R. Iravani, "Enhanced equivalent model of the modular multilevel converter," *IEEE Transactions on Power Delivery*, vol. 30, no. 2, pp. 666–673, 2015.

[15] G. Song, T. Wang, X. Huang, and C. Zhang, "An improved averaged value model of mmc-hvdc for power system faults simulation," *International Journal of Electrical Power & Energy Systems*, vol. 110, pp. 223–231, 2019.

[16] G. Li, H. Ye, S. Gao, Y. Liu, and L. Gao, "Modeling and simulation of large power system with inclusion of bipolar mtdc grid," *International Journal of Electrical Power & Energy Systems*, vol. 116, p. 105 565, 2020.

[17] S. Cole and R. Belmans, "A proposal for standard vsc hvdc dynamic models in power system stability studies," *Electric Power Systems Research*, vol. 81, no. 4, pp. 967–973, 2019.

[18] L. M. Castro and E. Acha, "A unified modeling approach of multi-terminal vsc-hvdc links for dynamic simulations of large-scale power systems," *IEEE Transactions on Power Systems*, vol. 31, no. 6, pp. 5051–5060, 2016.

[19] "Analysis of faults in multiterminal hvdc grid for definition of test requirements of hvdc circuit breakers," *IEEE Transactions on Power Delivery*, vol. 33, pp. 403–411, 1 Feb. 2018, ISSN: 08858977. DOI: 10.1109/TPWRD.2017.2716369.

[20] C. Wang, P. Ju, F. Wu, X. Pan, and Z. Wang, "A systematic review on power system resilience from the perspective of generation, network, and load," *Renewable and Sustainable Energy Reviews*, vol. 167, Oct. 2022, ISSN: 18790690. DOI: 10.1016/j.rser.2022.112567.

[21] M. J. Pérez-Molina, D. M. Larruskain, P. E. López, and G. Buigues, *Challenges for protection of future hvdc grids*, 2020. DOI: 10.3389/fenrg.2020.00033.

[22] A. K. Khaimar and P. J. Shah, "Study of various types of faults in hvdc transmission system," Institute of Electrical and Electronics Engineers Inc., Jun. 2017, pp. 480–484, ISBN: 9781509004676. DOI: 10.1109/ICGTSPICC.2016.7955349.

[23] Tushar, V. Venkataramanan, A. Srivastava, and A. Hahn, "Cp-tram: Cyber-physical transmission resiliency assessment metric," *IEEE Transactions on Smart Grid*, vol. 11, pp. 5114–5123, 6 Nov. 2020, ISSN: 19493061. DOI: 10.1109/TSG.2020.2996137.

[24] M. Panteli, P. Mancarella, D. N. Trakas, E. Kyriakides, and N. D. Hatziargyriou, "Metrics and quantification of operational and infrastructure resilience in power systems," *IEEE Transactions on Power Systems*, vol. 32, pp. 4732–4742, 6 Nov. 2017, ISSN: 08858950. DOI: 10.1109/TPWRS.2017.2664141.

[25] R. H. Chandio, F. A. Chachar, J. B. Soomro, *et al.*, "Control and protection of mmc-based hvdc systems: A review," *Energy Reports*, vol. 9, pp. 1571–1588, 2023.

[26] ENTSO-E, "Hvdc links in system operations," 2019.

[27] S. Ruihua, Z. Chao, L. Ruomei, and Z. Xiaoxin, "Vscs based hvdc and its control strategy," vol. 2005, 2005, pp. 1–6, ISBN: 0780391144. DOI: 10.1109/TDC.2005.1546800.

[28] Q. Yang, S. L. Blond, R. Aggarwal, Y. Wang, and J. Li, "New ann method for multi-terminal hvdc protection relaying," *Electric Power Systems Research*, vol. 148, pp. 192–201, Jul. 2017, ISSN: 03787796. DOI: 10.1016/j.epsr.2017.03.024.

[29] "Fault detection and interruption in an earthed hvdc grid using rocov and hybrid dc breakers," *IEEE Transactions on Power Delivery*, vol. 31, pp. 973–981, 3 Jun. 2016, ISSN: 19374208. DOI: 10.1109/TPWRD.2014.2364547.

[30] G. P. Adam, K. H. Ahmed, S. J. Finney, and B. W. Williams, "Ac fault ride-through capability of a vsc-hvdc transmission systems," 2010, pp. 3739–3745, ISBN: 9781424452866. DOI: 10.1109/ECCE.2010.5617786.

[31] J. A. Ansari, C. Liu, and S. A. Khan, "Mmc based mtdc grids: A detailed review on issues and challenges for operation, control and protection schemes," *IEEE Access*, vol. 8, pp. 168 154–168 165, 2020, ISSN: 21693536. DOI: 10.1109/ACCESS.2020.3023544.

[32] C. W. G. B4.57, "Guide for the development of models for hvdc converters in a hvdc grid," 2014. [Online]. Available: https://e-cigre.org/publication/604-guide-for-the-development-of-models-for-hvdc-converters-in-a-hvdc-grid.

[33] D. Wand and L. Liu, "Rtds training course of iepg," 2018.

[34] K. S. Lakshmi, G. Sravanthi, L. Ramadevi, *et al.*, "A review paper on technical data of present hvdc links in india," *International journal of Recent and Innovations trends in Computing and Communication*, vol. 3, no. 4, pp. 1985–1991, 2015.

[35] E. Kontos, R. T. Pinto, S. Rodrigues, and P. Bauer, "Impact of hvdc transmission system topology on multiterminal dc network faults," *IEEE Transactions on Power Delivery*, vol. 30, pp. 844–852, 2 Apr. 2015, ISSN: 08858977. DOI: 10.1109/TPWRD.2014.2357056.

[36] A. Ametani, "A general formulation of impedance and admittance of cables," *IEEE transactions on power apparatus and systems*, no. 3, pp. 902–910, 1980.

[37] D. Povh, P. Thepparat, and D. Westermann, "Further development of hvdc control," 2011, ISBN: 9781424484195. DOI: 10.1109/PTC.2011.6019447.

[38] D. Kotur and P. Stefanov, "Optimal power flow control in the system with offshore wind power plants connected to the mtdc network," *International Journal of Electrical Power and Energy Systems*, vol. 105, pp. 142–150, Feb. 2019, ISSN: 01420615. DOI: 10.1016/j.ijepes.2018.08.012.

[39] L. Dewangan and H. J. Bahirat, "Comparison of hvdc grid control strategies," in *2017 IEEE PES Asia-Pacific Power and Energy Engineering Conference (APPEEC)*, IEEE, 2017, pp. 1–6.

[40] A. Egea-Alvarez, J. Beerten, D. V. Hertem, and O. Gomis-Bellmunt, "Hierarchical power control of multiterminal hvdc grids," *Electric Power Systems Research*, vol. 121, pp. 207–215, 2015, ISSN: 03787796. DOI: 10.1016/j.epsr.2014.12.014.

[41] K. Rouzbehi, J. I. Candela, G. B. Gharehpetian, L. Harnefors, A. Luna, and P. Rodriguez, *Multiterminal dc grids: Operating analogies to ac power systems*, 2017. DOI: 10.1016/j.rser.2016.11.270.

[42] N. M. Kangwa, C. Venugopal, and I. E. Davidson, “A review of the performance of vsc-hvdc and mtdc systems,” *2017 IEEE PES PowerAfrica*, pp. 267–273, 2017.

[43] C. B4.72, “Dc grid benchmark models for system studies,” 2020. [Online]. Available: `https://e-cigre.org/publication/804-dc-grid-benchmark-models-for-system-studies`.

[44] T. K. Vrana, Y. Yang, D. Jovcic, S. Dennetière, J. Jardini, and H. Saad, “The cigre b4 dc grid test system,” *Electra*, vol. 270, no. 1, pp. 10–19, 2013.

[45] L. Almobasher, L. R. Almobasher, I. Omar, and A. Habiballah, “Review of power system faults,” 2020. [Online]. Available: `https://www.researchgate.net/publication/345761217`.

[46] M. Liu, J. Chen, and F. Milano, “On-line inertia estimation for synchronous and non-synchronous devices,” *IEEE Transactions on Power Systems*, vol. 36, no. 3, pp. 2693–2701, 2020.

[47] M. Sun, G. Xie, L. Chen, Y. Liu, X. Li, and Y. Min, “Study on the necessity and role of inertia in power system frequency response,” in *2020 IEEE 4th Conference on Energy Internet and Energy System Integration (EI2)*, IEEE, 2020, pp. 155–159.

[48] X. Deng, R. Mo, P. Wang, J. Chen, D. Nan, and M. Liu, “Review of rocof estimation techniques for low-inertia power systems,” *Energies*, vol. 16, no. 9, p. 3708, 2023.

[49] T. Bašakarad, N. Holjevac, I. Kuzle, N. Zovko, *et al.*, “Rocof importance in electric power systems with high renewables share: A simulation case for croatia,” 2021.

[50] K. E. Martin, “Synchrophasor measurements under the ieee standard c37. 118.1-2011 with amendment c37. 118.1 a,” *IEEE Transactions on Power Delivery*, vol. 30, no. 3, pp. 1514–1522, 2015.

[51] A. C. en Markt. “Netcode elektriciteit.” (10 june 2023), [Online]. Available: `https://wetten.overheid.nl/BWBR0037940/2023-06-10`. (accessed: 27-07-2023).

[52] R. Bründlinger, “Grid codes in europe—overview on the current requirements in european codes and national interconnection standards,” *AIT Austrian Institute of Technology: Vienna, Austria*, 2019.

[53] X. Hou, Y. Sun, X. Zhang, J. Lu, P. Wang, and J. M. Guerrero, “Improvement of frequency regulation in vsg-based ac microgrid via adaptive virtual inertia,” *IEEE Transactions on Power Electronics*, vol. 35, no. 2, pp. 1589–1602, 2019.

[54] C. Broderick, “Rate of change of frequency (rocof) withstand capability,” *ENTSOE, Brussels, Belgium, Tech. Rep*, 2018.

[55] H. S. Salama and I. Vokony, “Voltage stability indices–a comparison and a review,” *Computers & Electrical Engineering*, vol. 98, p. 107 743, 2022.

[56] M. J. Pérez-Molina, P. Eguia, M. Larruskain, G. Buigues, and E. Torres, “Non-unit rocov scheme for protection of multi-terminal hvdc systems,” in *2020 22nd European Conference on Power Electronics and Applications (EPE’20 ECCE Europe)*, IEEE, 2020, pp. 1–10.

[57] J. Sneath and A. D. Rajapakse, “Fault detection and interruption in an earthed hvdc grid using rocov and hybrid dc breakers,” *IEEE Transactions on Power Delivery*, vol. 31, no. 3, pp. 973–981, 2014.

[58] C. R. (2016/631, “Establishing a network code on requirements for grid connection of generators,” *Off. J. Eur. Union*, vol. 631, pp. 1–68, 2016.

[59] MachineLearning1. “Signal processing – apply median filters (python).” (13 july 2014), [Online]. Available: `https://machinelearning1.wordpress.com/2014/07/13/signal-processing-apply-median-filters-python/`. (accessed: 27-07-2023).

[60] ENTSO-E. “Frequency stability evaluation criteria for the synchronous zone of continental europe.” (March 2016), [Online]. Available: `chrome-extension://efaidnbmnnnibpcajpcglclefindmkaj/https://eepublicdownloads.entsoe.eu/clean-documents/SOC%20documents/RGCE_SPD_frequency_stability_criteria_v10.pdf`. (accessed: 27-07-2023).

[61] C. B4.72, “Cigre wg b4.72 dc grid models,” October 2020.

[62] S. Subedi, M. Rauniyar, S. Ishaq, *et al.*, “Review of methods to accelerate electromagnetic transient simulation of power systems,” *IEEE Access*, vol. 9, pp. 89 714–89 731, 2021.

[63] X. Guillaud, M. O. Faruque, A. Teninge, *et al.*, “Applications of real-time simulation technologies in power and energy systems,” *IEEE Power and Energy Technology Systems Journal*, vol. 2, no. 3, pp. 103–115, 2015.

[64] *Rtds hardware manual*, RTDS Technologies, Winnipeg, Canada, 2020.

[65] *Introductory tutorial*, RTDS Technologies, Winnipeg, Canada.

[66] D. Wang, L. Lio, and J. L. Rueda Torres, “Rtds training course of iepg: Day 6 mmc and hvdc example,” 2018. [Online]. Available: `https://e-cigre.org/publication/804-dc-grid-benchmark-models-for-system-studies`.

[67] Q. Zhang, C. Wang, X. Li, X. Qian, P. Ye, and Y. Zhao, “Power system equivalent inertia evaluation algorithm based on intelligent optimization,” *Energy Reports*, vol. 8, pp. 271–282, 2022.

[68] A. Ghoshal and V. John, “Anti-windup schemes for proportional integral and proportional resonant controller.,” 2010.

[69] Matlab. “Anti-windup control using pid controller block.” (2020), [Online]. Available: https://nl.mathworks.com/help/simulink/slref/anti-windup-control-using-a-pid-controller.html. (accessed: 09-08-2023).

[70] M. Wang, M. Abedrabbo, W. Leterme, *et al.*, “A review on ac and dc protection equipment and technologies: Towards multivendor solution,” in *CIGRE Winnipeg 2017 Colloquium*, Cigré, 2017, pp. 1–11.

[71] “Protection systems for multi-terminal hvdc grids,” *Renewable Energy and Power Quality Journal*, vol. 1, pp. 310–315, 16 Apr. 2018, ISSN: 2172038X. DOI: 10.24084/repqj16.296.

[72] *Vsc dc breaker model*, RTDS Technologies, Winnipeg, Canada, 2020.

[73] A. Hammer, “Analysis of ieee power system stabilizer models,” M.S. thesis, Institutt for elkraftteknikk, 2011.

[74] Y. Baza, S. Cozo, and R. Nayeli, “Excitation system type st1 for a synchronous machine,” *International Journal of Engineering and Science*, vol. 4, no. 4, pp. 44–53, 2015.

[75] Matlab. “Governor type 1.” (2020), [Online]. Available: https://nl.mathworks.com/help/sps/ref/governortype1.html. (accessed: 09-08-2023).

A

Python codes

A.1. Rate of change function

```
def ROCO_frame(array, t_w, step, beg):
    Ts = 1/20000
    Fs = 1/Ts

    ROCO_array = []
    length = []

    # Determine start and end sample
    start = int(beg*Fs)
    end = int(start+t_f*Fs)

    # Move window until final sample (5 sec)
    while end < 100000:
        # Define start and end value
        value_start = array[start]
        value_end = array[end]

        # Calculate rate of change and append
        ROCO_array = np.append(ROCO_array, abs((value_end - value_start)/t_f))

        # Define new samples locations
        start = start + step
        end = end + step

    return max(ROCO_array)
```

A.2. Generae metric table function

```
def Metric_generator(Cases, scen, name, t_f, t_v):

    ROCOFA1 = {}
    ROCOFA2 = {}
    ROCOFA3 = {}
    ROCOFA4 = {}
    ROCOFA5 = {}

    ROCOVA1 = {}
```

```
ROCOVA2 = {}
ROCOVA3 = {}
ROCOVA4 = {}
ROCOVA5 = {}


Fault = {}
FaultClass = {}
Scenario = {}
ScenFault = {}

# Loop to sort the type of fault
for cas in Cases:

    Scenario[cas] = name
    Fault[cas] = cas


    if "DCF" in cas:
        if "LL" in cas:
            FaultClass[cas] = "LL - DCF"

            ScenFault[cas] = name + " LL - DCF"
        else:
            FaultClass[cas] = "LG - DCF"

            ScenFault[cas] = name + " LG - DCF"
    elif "ACF" in cas:
        if "LL" in cas:
            FaultClass[cas] = "LL - ACF"

            ScenFault[cas] = name + " LL - ACF"
        else:
            FaultClass[cas] = "3LG - ACF"

            ScenFault[cas] = name + " 3LG - ACF"
    elif "cb" in cas:
        FaultClass[cas] = "Converter outage"

        ScenFault[cas] = name + " Converter outage"
    elif "Line" in cas:
        FaultClass[cas] = "Line outage"

        ScenFault[cas] = name + " Line outage"
    else:
        FaultClass[cas] = "Generator outage"

        ScenFault[cas] = name + " Generator outage"


    # Obtain data from the measurements
    Data_A1 = pd.read_csv(r"C:\\" + scen + "_" + cas + "_A1_Data.csv")
    Data_A2 = pd.read_csv(r"C:\\" + scen + "_" + cas + "_A2_Data.csv")
    Data_A4 = pd.read_csv(r"C:\\" + scen + "_" + cas + "_A4_Data.csv")
    Data_A5 = pd.read_csv(r"C:\\" + scen + "_" + cas + "_A5_Data.csv")
```

```
        # Filter input data
        DC_A1 = median_filter(Data_A1['Subsystem #1|CTLs|Vars|EdcbA1'], size=200, mode='nearest')
        DC_A2 = median_filter(Data_A2['Subsystem #1|CTLs|Vars|EdcbA2'], size=200, mode='nearest')
        DC_A4 = median_filter(Data_A4['Subsystem #1|CTLs|Vars|EdcbA3'], size=200, mode='nearest')
        DC_A5 = median_filter(Data_A5['Subsystem #1|CTLs|Vars|EdcbA5'], size=200, mode='nearest')

        Freq_A1 = median_filter(Data_A1['Subsystem #1|CTLs|Vars|Freq_A1'], size=200, mode='nearest')
        Freq_A2 = median_filter(Data_A2['Subsystem #1|CTLs|Vars|Freq_A2'], size=200, mode='nearest')
        Freq_A4 = median_filter(Data_A4['Subsystem #1|CTLs|Vars|Freq_A4'], size=200, mode='nearest')
        Freq_A5 = median_filter(Data_A5['Subsystem #1|CTLs|Vars|Freq_A5'], size=200, mode='nearest')



        # calculate values
        ROCOFA1[cas] = ROCO_frame(Freq_A1, t_f, 2, 0.02)
        ROCOFA2[cas] = ROCO_frame(Freq_A2, t_f, 2, 0.02)
        ROCOFA4[cas] = ROCO_frame(Freq_A4, t_f, 2, 0.02)
        ROCOFA5[cas] = ROCO_frame(Freq_A5, t_f, 2, 0.02)


        ROCOVA1[cas] = ROCO_frame(DC_A1, t_v, 2, 0.02)
        ROCOVA2[cas] = ROCO_frame(DC_A2, t_v, 2, 0.02)
        ROCOVA4[cas] = ROCO_frame(DC_A4, t_v, 2, 0.02)
        ROCOVA5[cas] = ROCO_frame(DC_A5, t_v, 2, 0.02)



    Metrics = {}

    # Generate table with column per metric and location
    Metrics['ROCOF A1 - (Hz/s)'] = ROCOFA1
    Metrics['ROCOF A2 - (Hz/s)'] = ROCOFA2
    Metrics['ROCOF A3 - (Hz/s)'] = ROCOFA3
    Metrics['ROCOF A4 - (Hz/s)'] = ROCOFA4
    Metrics['ROCOF A5 - (Hz/s)'] = ROCOFA5

    Metrics['ROCOV A1 - (kV/s)'] = ROCOVA1
    Metrics['ROCOV A2 - (kV/s)'] = ROCOVA2
    Metrics['ROCOV A3 - (kV/s)'] = ROCOVA3
    Metrics['ROCOV A4 - (kV/s)'] = ROCOVA4
    Metrics['ROCOV A5 - (kV/s)'] = ROCOVA5



    Metrics['Fault'] = Fault
    Metrics['Type of fault'] = FaultClass
    Metrics['Scenario'] = Scenario
    Metrics['Fault in scenario'] = ScenFault

    Metrics_table = pd.DataFrame.from_dict(Metrics)

    return Metrics_table
```

B

Control blocks of the synchronous machine

B.1. Power System stabilizer IEEE2ST

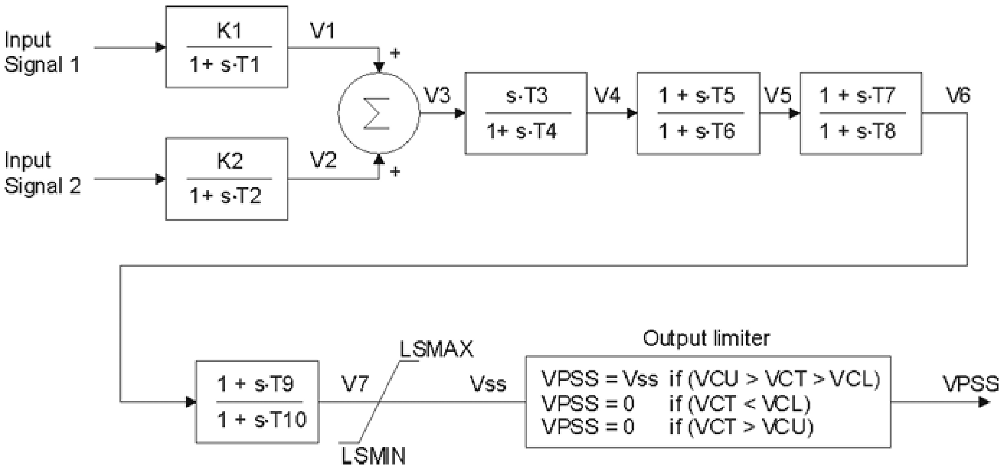

Figure B.1: Block diagram of the PSS control block IEEE2ST [73]

B.2. Exciter IEEE ST1

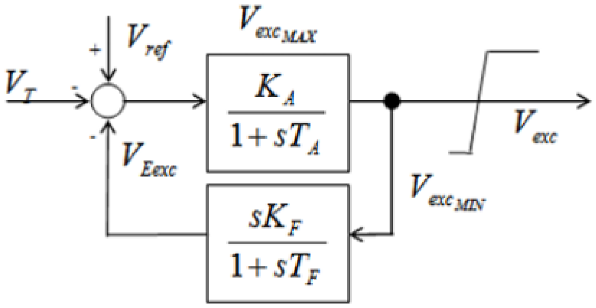

Figure B.2: Block diagram of the exciter control block IEEE ST1 [74]

B.3. Governor IEEE Type 1

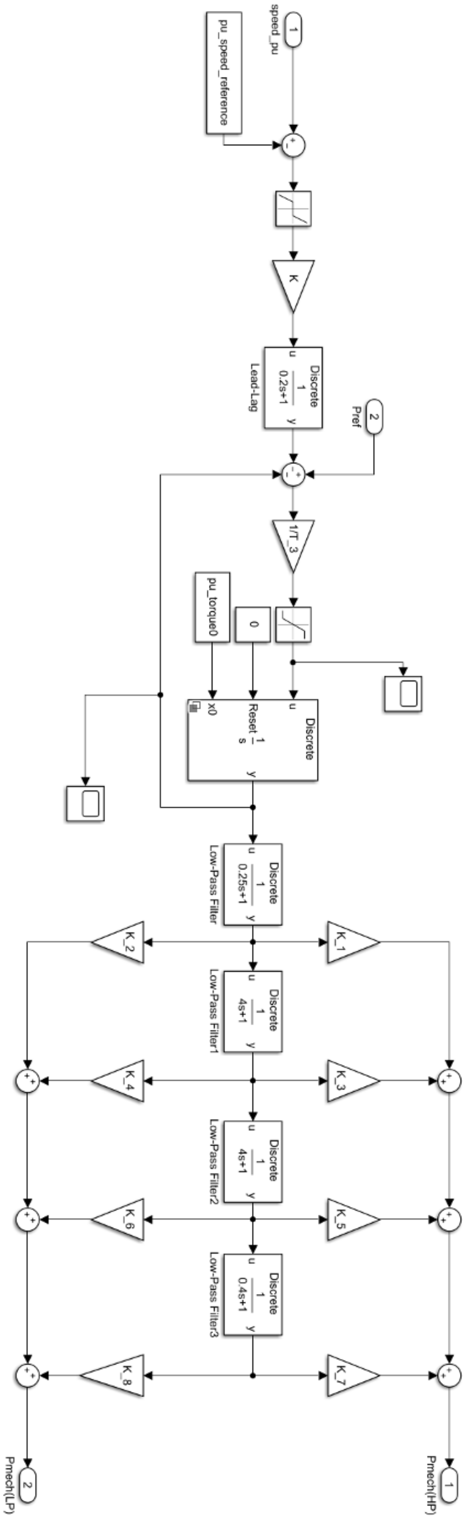

Figure B.3: Block diagram of the governor control block IEEE type 1 [75]

C

Hybrid DC breaker model RSCAD

This section is taken from [72]. As the document may not be available to everyone, the relevant parts of the description of the model are copied to the thesis.

The hybrid DC breaker consists of the following components:

- A Residual Current Disconnecting Circuit Breaker (RCDCB) to break the residual DC current of the DC breaker. In a practical hybrid HVDCbreaker, a second RCDCB is provided for security reasons. In this model, the second RCDCB is not modeled, the current of the second RCDCB is the same as the first one.
- A Current Limiting Reactor.
- A Main breaker path consisting of a number of series cells (1 to 10). Each cell consists of an IGBT/diode arrangement in parallel with main cell arrestors to carry the current when required.
- An auxiliary path parallel to the main path breaker path consisting of aUltraFast Disconnector (UFD) and a Load Commutation Switch (LCS). The function of this section is to provide a path with low voltage drop for the current during normal operation. The Load Commutation Switch consists of an IGBT/diode arrangement in parallel with an arrestor. The UltraFast Disconnector isolates the LCS once current commutates to the Main cells. Note that, UFD does not have the capacity to extinguish arc.

C.1. Principle of operation

Basic operation of the DC breaker is outlined here. As mentioned previously, during normal operation, the auxiliary path containing the UFD and LCS provides the path for the current. When the DC breaker needs to open, the first thing that happens is that the IGBTs in the main breaker are fired to provide a path for the DC current that needs to be commutated out of the UFD/LCS . Then the LCS IGBTs are blocked to force the current into the LCS arrestor which has a fairly low discharge voltage (e.g.10 kV). The voltage drop on the LCS arrestor is enough to almost instantly force the current into the IGBTs in the main path. The current in the UFD is then so low that the UFD can be opened and recovers the ability to block the full breaker rated voltage. At this point, the DC current is flowing in the IGBT cells of the main path. Therefore, the next thing that happens is that the main cell IGBTs are blocked. This forces the main path current through the N arrestors in series where N is the number of cells in the main path. The arrestors in the main cell have higher discharge voltage (about 100 kV). This means the backvoltage created by the arrestors is about (N×100 kV). This backvoltage quickly brings the DC current to zero. The whole process takes only a few milliseconds. The inductance value of Current Limiting Reactor affects this time required for the current to reach zero. At this point the Residual Current DC Breaker (RCDCB) can isolate the line.

Similarly, when the goal is to energize the DC line and basically close the DC breaker, the following procedure needs to take place. RCDCB needs to be closed, then IGBTs in the main cells are fired to provide a path for DC current. Special firing procedure may be required to have a smooth energization of the line. Then, UFD is closed and IGBT(s) in the LCS are fired. Blocking the IGBTs in the Main cells commutates the DC current into the auxiliary path.